INVESTIGATING THE EFFECT OF HEAT TRANSFER DRIVING FORCE AND SEED LOADING ON THE BATCH EUTECTIC FREEZE CRYSTALLIZATION OF A DILUTE BRINE

Author: Anotidaishe Spencer

Supervisor(s): Professor Alison Lewis, Mr Jemitias Chivavava

Dissertation submitted in partial fulfilment of the requirements for the degree of Master of Science in Engineering

Department of Chemical Engineering
Faculty of Engineering and the Built Environment
University of Cape Town
2022

Declaration: *I know the meaning of plagiarism and declare that all the work in the document, save for that which is properly referenced, is mine*

Signed by candidate

…………………………………….

ABSTRACT

Eutectic Freeze Crystallization (EFC) is a separation technology that separates solute from solvent. It is often used as a wastewater treatment process for industrial brines. In EFC, the solution is cooled to temperatures below the eutectic point of the brine, such that ice and salt simultaneously crystallize out of solution. Solid-solid-liquid separation of the resulting suspension is achieved by exploiting differences in the densities of the phases. EFC has been found to perform well when applied to concentrated brines, but not with dilute brines. Previous studies have shown that the chosen operating conditions for the crystallizer can result in phenomena that limit achievable yields and product purities. These phenomena are more severe when dilute brines are treated. One of these limiting phenomena is heat transfer, which is the principle that makes EFC possible. Understanding how operating conditions are related to the production of ice and salt through heat transfer can lead to better control of the EFC process. This would allow for consistent production of ice and salt at high yields and product purities, even for dilute brines.

The heat transfer driving force (ΔT_{LMTD}) and ice seed loading (SL) are two operating conditions that are of interest in this work as they are linked to heat transfer; ΔT_{LMTD}, directly by affecting the heat transfer rate and in turn the production capacity of a crystallizing system, and SL indirectly by forming the initial magma density (solid content in the crystallizer by mass) which affects crystallization location and the hydrodynamics of the system. These two operating conditions were chosen because their effect on production of ice and salt from dilute brines has not been studied before. The aim of this work was to understand how SL and ΔT_{LMTD} affect the yield of ice and salt and the purity of ice, in batch EFC. A synthetic Na_2SO_4 solution was used for crystallization experiments as its eutectic composition is dilute (4wt.%). Ice seed loadings between 0 and 12 wt.% and ΔT_{LMTD} values between 2 and 10°C were investigated. The yields of ice and salt, as well as the purity of ice, were measured to determine the relationship between ΔT_{LMTD} and the yield of ice and salt, ΔT_{LMTD} and ice purity, SL and the yield of ice and salt, and SL and ice purity.

It was found that as the ΔT_{LMTD} increased, the yield of ice and salt increased, due to the higher heat transfer rate. The ice yield was a sum of ice harvested from the bulk and ice formed on the wall (scale). The yield of ice in the bulk decreased with increasing ΔT_{LMTD}, whilst the yield of scale increased. As ΔT_{LMTD} increased, the cooled wall became colder, therefore the fluid closest to the wall had the most supersaturation. This led to the formation of a scale layer. The

combination of increased driving force and shortened scale formation time resulted in the observed increase in the scale yield. This increase in the scale yield increased heat transfer resistance between the coolant and the bulk, which produced less ice in the bulk.

It was also found that the purity of ice decreased as ΔT_{LMTD} increased. The salt particles were much finer than the ice particles (ice was >13 times larger than salt). The large difference between the ice and salt crystals, combined with increased salt production and intense mixing resulted in an increase in salt entrainment. Increased salt entrainment resulted in poor separation, and a reduction in ice purity was observed.

It was found that increasing the ice seed loading increased the yield of ice in the bulk and decreased the scale yield. A maximum in ice in the bulk and a minimum in the scale resulted from a seed loading of 9 wt.%. Solids in the system provided sufficient surface area to promote secondary nucleation and growth in the bulk such that heterogeneous nucleation at the wall was minimised. This reduced the propensity for scale formation. Once the seed loading increased to 12 wt.%, the mixing efficiency of the system decreased. This resulted in localised supersaturation at the wall, which in turn resulted in a scale layer. The reduced mixing efficiency increased the resistance to heat transfer within the bulk, resulting in reduced crystallization within the bulk, therefore the yield of ice in the bulk decreased. It was also found that the salt yield decreased as the seed loading increased. This was due to poor separation caused by the increase in magma density and increase in salt entrainment. The entrained salt in the ice product was washed off rather than harvested, explaining the low salt yield obtained. The salt product was small (80µm <mode< 120µm), and the wash water was increased as seed loading increased. This made washing more efficient and produced a purer final ice product.

ACKNOWLEDGEMENTS

I would like to thank:

My supervisors, Professor Alison Lewis, and Mr Jemitias Chivavava for the support, guidance and for always being open to share their wealth of knowledge of the field.

The trustees of the Julian Baring Scholarship Fund for supporting me financially through my studies.

My CPU peers, Taona, Jacolien, Lerato and Deborah for the engaging conversations and assistance with laboratory work.

My friends, Tanaka, James, and the Mhukas. I would not have been able to get through my work without your unwavering support, encouragement, and transport to and from the labs. My sister, Mufarowashe, and my helper Mai Tawanda, for watching Isabelle while I worked. It also takes a village to finish a Master's degree. Thank you for being my village.

My parents, Mama Gweru, for your prayers, continuous blessings, and always reminding me of my inner strength. Mama Harare, for your encouragement to always keep the finish line in mind. Daddy, for always being there to let me pick your brain and consistently reminding me that I am smart enough to get past any obstacle.

My daughter, Isabelle, I dedicate this Master's to you. I did it for you, so you know girls can do anything they put their minds to.

My husband, Victor, for supporting and believing in me as a person, as an engineer and as a scientist, even when I didn't believe in myself. For holding my hand through the entire journey and sometimes carrying me when I couldn't walk the journey myself. I truly could not have done this without you. My love, thank you.

God almighty. All I have to say is thank you Lord.

NOMENCLATURE

A	heat transfer area of the crystallizer
Cp	specific heat capacity
Cs	seed loading ratio
Cs^*	critical seed loading ratio
$D_{scraper}$	diameter of the scraper blades
k_a	crystal area shape factor
k_v	shape volume factor
L_{sp}	theoretical product size
L_{wp}	experimental product size
$\dot{m}$	mass flow rate
N	number of seeds
$N_{scraper}$	scraping rate
ppm	parts per million
Q_{crys}	heat used for the crystallization of ice and salt out of solution
Q_{feed}	heat energy used to cool the feed to the eutectic temperature
Q_{gain},	heat gained from the surrounding the environment
r_c	critical size
Re	Reynolds number
S	seed surface area
T_{feed}	feed temperature
U	overall heat transfer coefficient
$\dot{V}$	feed flow rate into the crystallizer
V	volume of the crystallizer
Ws	mass of the seeds
W_{th}	theoretical yield
x_{feed}	solute mass fraction

Greek symbols

α	convective heat transfer coefficient
ΔH_{crys}	heat of crystallization
ΔT_{LMTD}	log mean temperature difference between the coolant and the process fluid
ρ	density
τ	residence time
μ	dynamic viscosity

CONTENTS

LIST OF FIGURES

LIST OF TABLES

1 INTRODUCTION

1.1 Background of the study

South Africa is an arid, water stressed country. It was ranked the 30th driest country in the world in a study carried out by Luo, Young and Reig (2015). South Africa sources most of its water from surface water, ground water, return flows and more recently, seawater(DWS, 2017). Most of this water is used for agriculture, municipal uses and industry. Studies based on water usage data and population growth models predict a 17 % gap between water supply and demand by 2030 (Water Resources Group, 2009). Such predictions as well as the fluctuating nature of South Africa's climate and rainfall highlights the need for better water management.

One way of improving water management is to reuse wastewater from the various sectors where it is created. South Africa's industry produces most of South Africa's wastewater. Mining alone uses 3% of South Africa's water (DWS, 2017) and from it produces wastewater. The desalination of sea water to produce 6% of South Africa's water supply (DWS, 2017) also produces waste. The common factor with these two industrial processes is the nature of the wastewater produced: both processes produce wastewater that contains inorganic salts. The wastewater from mining is currently neutralised before producing the saline wastewater (Johnson & Hallberg, 2005). The saline wastewater from desalination is a direct waste from the process. This is illustrated below:

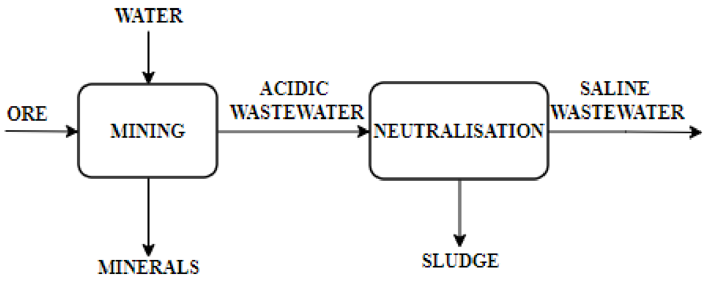

Figure 1.1: Basic block flow diagram of the mining process

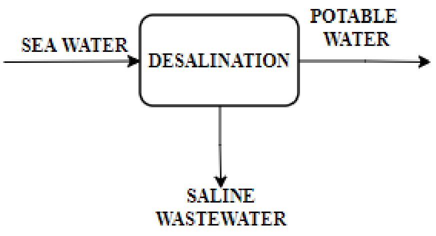

Figure 1.2: Basic block flow diagram of desalination process

The saline wastewater must be treated to make it potable or suitable for reuse in industry. The treatment is carried out by using volume reduction processes (evaporation, freeze crystallization and reverse osmosis) where potable water is produced (Jooste, 2016). The wastewater is incompletely converted to potable water as the processes are of limited efficiency. The waste from the volume reduction processes is more concentrated and still contains water which is the resource of interest. At this point, eutectic freeze crystallization

(EFC) can be employed to increase the recovery of potable water from the concentrated wastewater.

Eutectic freeze crystallization is a separation technique used to separate solute from solvent by converting the solute and solvent from liquid to solid(Lewis et al., 2015). This simultaneous phase change is achieved by cooling the wastewater to temperatures below its eutectic point. Eutectic freeze crystallization is used to treat wastewater where the solute is often a made up of multiple metallic salts, and the solvent is water. Because ice and salts are both products in EFC, a wastewater treatment process with EFC as its final stage should theoretically become a zero-waste process. This makes EFC a worthwhile technology to explore, understand and apply.

Eutectic freeze crystallization has been implemented on real industrial inorganic brines and has been found to perform well when the brines are highly concentrated (Genceli, Gärtner & Witkamp, 2005; Rodriguez-Pascual et al., 2010). When applied to dilute brines, however, EFC is less effective. Stable operation at high production rates has not been achieved. One reason for this failure is heat transfer limitations within the system caused by the formation of a layer of ice on the cooled wall of the crystallizer. The insulating effect of the scale layer makes achieving high, stable production impossible.

1.2 Research aim, scope, and limitations

Understanding the processes taking place during EFC can lead to improving the process by allowing for the minimisation of heat transfer limitations. The aim of the study is to understand the relationship between operating conditions and the production of ice and salt. The two operating conditions focused on in this study are ice seed loading and heat transfer driving force, as they were identified as being linked to heat transfer. The study was particularly aimed at understanding these relationships for a dilute brine in order to improve use of EFC when a dilute brine needs to be treated.

The effect of ice seed loading and heat transfer driving force on the production of ice and salt was tested in a 1.45 L glass laboratory-scale cooled-wall crystallizer and carried out over three years (2019-2021). This study was conducted on a synthetic Na_2SO_4 solution as its eutectic composition is very dilute (4 wt.%). The focus of this study was on the effects of ice seed loading and heat transfer driving force on the yield of ice and salt, as well as the purity of ice.

1.3 Thesis Outline

The report starts in Chapter 2 where some fundamental crystallization concepts are defined and explained. The literature review, Chapter 3, follows where studies on various factors affecting production rate/yield and purity are discussed. Chapter 4 describes the motivation for the work, the hypotheses, and the key questions that arise from the hypotheses. The materials and methods used to test the hypothesis are described in Chapter 5. Chapter 6 presents the discussion of the findings from the experimental work. These findings are concluded in Chapter 7. In Chapter 8, recommendations for future work are discussed.

2 THEORY

2.1 Eutectic freeze crystallization

Eutectic freeze crystallization is the crystallization of ice and salt from solution due to the cooling of the solution. There are multiple methods to achieve crystallization by cooling. These can be shown on a phase diagram which is a representation of the phases of a system based on the conditions (temperature or pressure) of the system. Figure 2.1 shows a phase diagram for a binary aqueous solution showing different cooling paths that can be applied to a brine/solution.

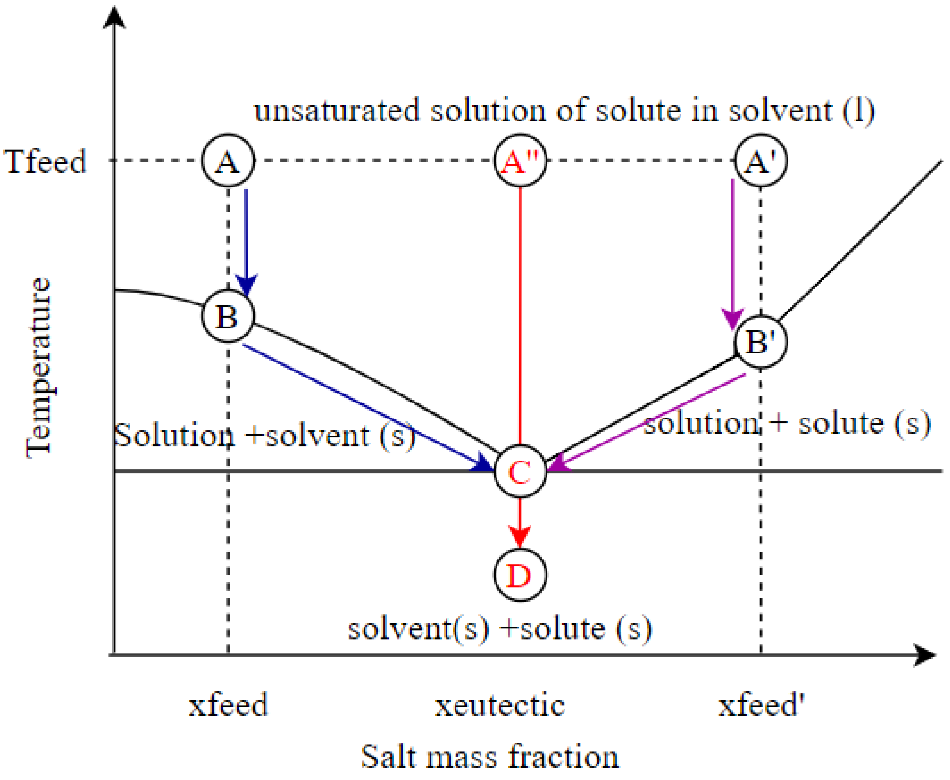

Figure 2.1: Binary phase diagram adapted from Lewis et al. (2015); (Myerson, 2002), A, A' AND A'' represent a solution at T_{feed} and of composition x_{feed}, $x_{feed'}$ and $x_{eutectic}$ respectively; B and B' show the solubility temperature of solution of composition x_{feed} and $x_{feed'}$ respectively, C is the eutectic temperature and composition of the solution, D shows a supersaturated solution of eutectic composition

The type of crystallization achieved is determined by the cooling path applied(Myerson, 2002). Using Figure 2.1 above, for a binary aqueous solution, the cooling of the solution at a temperature T_{feed} and solute mass fraction x_{feed} (A to B), results in the crystallization of the solvent. Further cooling results in more solvent crystallizing out of solution, leaving the solution more concentrated (B to C). Cooling via pathway **ABC** such that the solvent solidifies, represents freeze crystallization(Myerson, 2002). Path **A'B'C** for a solution at temperature T_{feed} and solute mass fraction of x_{feed}', represents cooling crystallization(Myerson, 2002). Here, the concentration decreases due to the solute crystallizing out of solution. As cooling continues and temperatures become lower than the eutectic point (C to D), solute and solvent crystallize out of solution simultaneously. This is eutectic freeze crystallization, EFC(Lewis et al., 2015). The liquidus line, **BCB’**, represents all the temperature-solution concentration conditions where liquid and solid are at equilibrium (Ulrich & Stelzer, 2011). Eutectic freeze crystallization can be achieved first either by cooling or freeze crystallization (until the solution reaches eutectic composition) then by further cooling (path **ABCD** or **A’B’CD**) or by cooling a solution at eutectic composition to a temperature below the eutectic temperature (Path **A’’CD**).

2.2 Supersaturation

Crystallization is a phase-changing process that is thermodynamically driven by supersaturation. Supersaturation is a driving force that determines the time required for crystallization to obtain a certain mass of solids (Myerson, 2002). This driving force arises when the system undergoing crystallization deviates from thermodynamic equilibrium.

A solution can be defined as supersaturated when the solution concentration exceeds the equilibrium concentration at a given temperature, or when the solution temperature is below the equilibrium temperature at a given concentration (Myerson, 2002). Creating supersaturation means that a system undergoes a change in either temperature, concentration or both. Myerson (2002) states that supersaturation is achieved by cooling, evaporation of the solvent, chemical reaction or by changing the solvent/solution composition.

2.3 Nucleation

Nucleation is the birth of crystals (Myerson, 2002) which occurs due to cluster formation. These clusters are the nuclei on which crystals develop (Mullin, 2001b); nuclei must be present for crystallization to occur.

2.3.1 Primary nucleation

Cluster formation makes up the classical nucleation theory (Lewis et al., 2015; Ulrich & Stelzer, 2011). That theory stipulates that clusters are formed by an addition mechanism where units of the crystals, either atoms, ions or molecules, collide with, then attach to each other to form clusters (Myerson, 2002). For the crystal to grow to a visible size, the clusters must reach and exceed a certain size, referred to as the critical size, r_c (Mullin, 2001b). This is because clusters of radius greater than r_c decrease the required free energy for nucleation (Myerson, 2002).

Primary nucleation occurs in systems where crystalline matter is not present (Mullin, 2001b) and includes both homogenous and heterogenous nucleation (Ulrich & Stelzer, 2011). Homogenous primary nucleation refers to nucleation that occurs spontaneously, while heterogenous refers to primary nucleation that is induced by foreign particles or surfaces. The presence of foreign particles or surfaces lowers the free energy barrier that must be overcome for nucleation to take place. Due to this lower barrier, heterogenous nucleation requires lower supersaturation than homogenous nucleation. The free energy required for nucleation depends on the contact angle of the nucleus on the foreign particle/surface. For homogeneous nucleation, the contact angle would have to be zero. Because such systems do not exist in practice, heterogenous primary nucleation is more likely to occur than homogenous.

For every substance there exists a region where the solution is supersaturated but not enough for crystals to form (Ulrich & Stelzer, 2011) and is known as the metastable region. It is a region made up of temperature-concentration (x-y) points some width above the solubility line of the substance. This is shown in Figure 2.2:

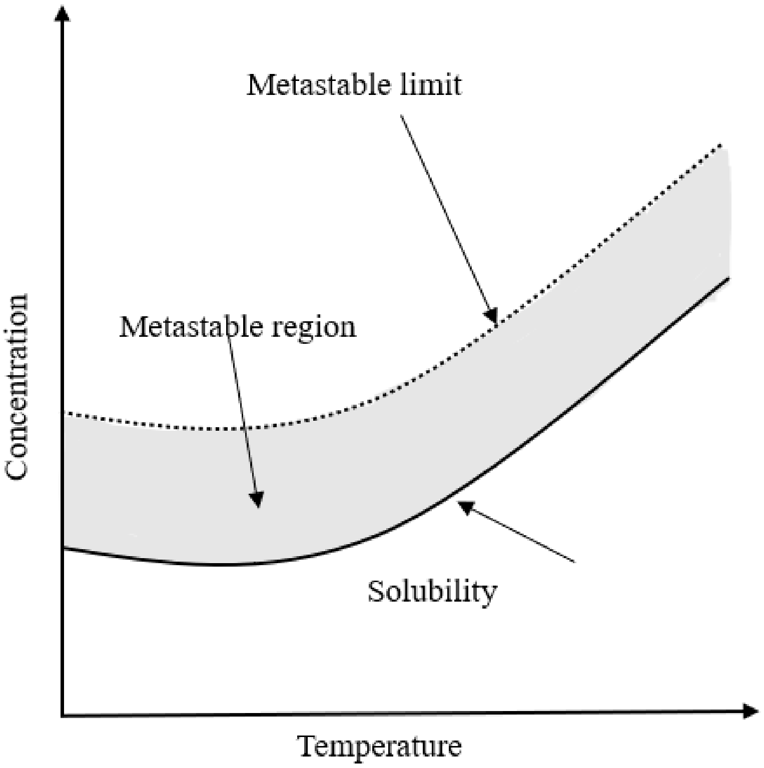

Figure 2.2: Metastable region illustration, adapted from Ulrich and Stelzer (2011)

Primary nucleation will not occur in this region as the supersaturation is too low (Ulrich & Stelzer, 2011). Primary nucleation is achieved by changing the solution temperature or concentration so that the supersaturation is above the metastable region.

2.3.2 Secondary nucleation

In secondary nucleation, crystals of the solute or solvent must be present (Ulrich & Stelzer, 2011). In industrial crystallization, secondary nucleation is more important because crystals needed for secondary nucleation to take place are already present in the crystallizer (Ulrich & Stelzer, 2011). These crystals induce nucleation more readily at low supersaturation, i.e. within the metastable region (Mullin, 2001b).

Secondary nucleation can be achieved by:

- Initial breeding which occurs when dry seeds are immersed into a supersaturated solution (Haan & Bosch, 2013; Mullin, 2001b; Ulrich & Stelzer, 2011). During the drying of the seeds, extremely small crystals form on the surface of the seeds and, once the seeds are added to the solution, these crystals are dislodged from the surface of the seeds and become new nuclei (Lewis et al., 2015; Ulrich & Stelzer, 2011).
- Contact nucleation is what happens when nuclei are formed by collision between the crystals (Mullin, 2001b; Ulrich & Stelzer, 2011) or collision between the crystals and the walls of the crystallizer or collision between the crystals and the impeller. These collisions chip away the edges and surfaces of the crystals and this forms nuclei (Lewis et al., 2015).
- Shear breeding happens where a supersaturated solution contacts crystals by flowing past them (Ulrich & Stelzer, 2011). The strength of this contact between the solution and the crystals can either be high enough to break the crystal, causing an attrition fragment to form, and become a new nucleus (Lewis et al., 2015) or the flow of the solution must be turbulent enough to carry with it crystal precursors around a growing crystal (Haan & Bosch, 2013; Ulrich & Stelzer, 2011).

2.4 Seeding

As a solution is cooled, primary nucleation can occur at any random temperature that is beyond the metastable region. The random nature of nucleation is referred to as stochastic nucleation as there is no way to precisely tell at what temperature nucleation occurs. This makes controlling the crystallization process difficult. It is important to control the nucleation temperature because it affects the ice and salt product. For improved control of nucleation, seeding is employed. Seeding is the addition of solute or solvent crystals to a solution to initiate crystallization. Seeding induces secondary nucleation so the supersaturation is low, i.e., within the metastable zone. Nucleation is controlled by seeding as the seeds are added to the solution at a known temperature.

The ice and salt product formed from solution is not only affected by nucleation temperature but by the characteristics of the seeds as well. One of the most important characteristics of the seeds used is the mass of seeds, known as the seed loading. A measure of the seed loading is the seed loading ratio. Cs is the ratio of the mass of seeds to the theoretical yield of the salt being crystallized (Doki et al., 1999). This is depicted in equation **2.1**:

$$C_S = \frac{W_S}{W_{th}} \tag{2.1}$$

where Ws(kg) is the mass of the seeds and W_{th} (kg) is the theoretical yield.

By assuming the product only arises due to growth of the seeds (no nucleation), the growth rate is independent of crystal size and the growth rate is not dispersed (Lewis et al., 2015). The mass of seeds can also be described by

$$W_s = N k_v \rho_{seed} L_{seed}^3 \tag{2.2}$$

where N is the number of seeds, k_v is the shape volume factor, ρ_{seed} (kg/m^3) is the density of the seeds, L_{seed} is the size of the seed crystals. The theoretical yield can therefore be described by

$$W_{th} = N k_v \rho_{seed} (L_{sp}^3 - L_{seed}^3) \tag{2.3}$$

where L_{sp} is theoretical product size. This makes the seed loading ratio to be

$$C_S = \frac{L_{seed}^3}{L_{sp}^3 - L_{seed}^3} \tag{2.4}$$

The choice of the seed loading ratio is dependent on the target product size (Lewis et al., 2015).

2.5 Crystal-size enlargement

A nucleus is required for crystals to develop. The nucleus can increase in size either by growth of the crystals or by small crystals clumping together, known as agglomeration.

2.5.1 Crystal growth

Crystal growth is the increase in size of the nuclei to visible sizes. Crystal growth is achieved by addition of the solute or solvent from the supersaturated solution, first by diffusion of growth units towards the surface of a crystal, then by integration of the units into the surface of the crystal (Lewis et al., 2015). The integration of single units onto a crystal surface has been stated to occur in three mechanisms (Myerson, 2002), set out in the Gibbs-Volmer theory, Kossel Growth Model and Burton-Cabrera-Frank (BCF) Model. These are theories that explain how growth occurs.

The Gibbs-Volmer theory states that when single units are to be integrated onto the surface of an existing crystal, they link at positions on the surface where the attractive forces are the greatest (Mullin, 2001a). These positions are known as active centres. The single units will continue to be added to the crystal surface until the entire face is complete. Once this happens, further growth occurs when a nucleus forms on the completed surface (Myerson, 2002). This becomes a new active centre that attracts more single units.

The Kossel model describes the crystal surface as having multiple flat steps that are made of vacancies (uneven texture) for the single units to be absorbed into. It also states that the crystal surface has kinks and corners (Lewis et al., 2015; Mullin, 2001a; Myerson, 2002). The easiest surface integration occurs at kinks, while nucleation is easiest at corners. The layer does not have to be complete for the growth of the next layer to commence.

The BCF model states that the layer-by-layer growth suggested by the Gibbs-Volmer theory or the flat step-by-step growth model suggested by the Kossel model is rare because crystal surfaces are not perfect. They have dislocations. These dislocations determine the shape of the crystal. The most common dislocation that has been observed is the screw dislocation which results in spiral growth and a spiral shape on the resulting crystal surface (Mullin, 2001a; Myerson, 2002).

Crystal growth can be rough or smooth depending on how the growth units are integrated into the surface. If the deposition of growth layers is orderly, the resulting growth is smooth, if not, it is rough. Supersaturation has the largest impact on how orderly crystal surface growth is. The higher the supersaturation, the rougher the growth.

2.5.2 Agglomeration

Lewis et al. (2015) define agglomeration as a crystal size enlargement process where two or more crystals attach for long enough for the space between them to be filled by growth of the crystal surfaces . This attachment by growth is known as cementation. Unlike growth which results in symmetrical crystals, the arrangement of crystals that form a larger particle by agglomeration is random, and the resulting crystal is not symmetrical or well ordered.

Agglomeration occurs when particles are transported by the waste-water flow in such a way that they collide. Transport can be achieved by Brownian motion, flow induced by agitation or motion due to particles settling (Lewis et al., 2015). Mullin (2001b) states that the collision results in attachment of the particles into aggregates. In process, particles form clumps due to attractive forces, such as Van der Waals forces. The aggregates are cemented by growth of crystals in corners and gaps to ‘glue’ particles together.

2.6 Crystal size decrease-breakage and attrition

When crystals are formed first by nucleation, single units attach but they also simultaneously detach from clusters. Single unit detachment is the first method of breakage and causes the crystal to reduce in size. In agglomeration, this phenomenon is present in that the aggregates can rupture from the repelling forces between the ions present on the surface of the particles (Lewis et al., 2015). Aggregates can also rupture as a result of collision with other aggregates, particles, agglomerates or crystallizer hardware.

When crystals rub against each other because of induced motion by agitation, abrasion or attrition may occur. Abrasion and attrition are size-decreasing mechanisms that occur at the surface of the crystal. Abrasion occurs when two particles rub against each other, while attrition occurs when a smaller particle is trapped between larger particles such that its sides are subjected to friction. Both mechanisms result in the wearing away of the surfaces of the crystals.

Breakage affects the shape and size of the crystal. Breakage can result in fine particles which affects the solid-solid separation and ultimately the purity of the product (refer to section 2.11)

2.7 Heat transfer

Heat transfer drives EFC. The heat transfer rate theoretically determines the production capacity of a crystallizer (Vaessen et al., 2003). After removing sensible heat, this is given by

$$\dot{m} = \frac{Q_{tot}}{\Delta H_{crystallization}} \qquad 2.5$$

where $\dot{m}$ (kg/s) is the mass flow rate of the products, Q is the heat transfer rate (W=kJ/s) and $\Delta H_{crystallization}$ (kJ/kg) is the heat of crystallization. The differences in temperature between the coolant and process fluid allow for cooling to temperatures below the eutectic point, so that crystallization occurs. Heat is transferred through the process fluid by convection, to the coolant through a wall by conduction, and through the coolant by convection (Welty et al., 2000).

The total heat transferred (Q_{tot}) from the process fluid and the surroundings to the coolant can be expressed using equation *2.6* (Vaessen et al., 2003):

$$Q_{tot} = UA\Delta T_{LMTD} + Q_{gain,m} \qquad 2.6$$

$Q_{gain,m}$ (W) is the energy the coolant gains from the environment and is measured when the coolant is circulated without crystallization(Vaessen et al., 2003), A(m^2) is the heat transfer area of the crystallizer, ΔT_{LMTD} (K) is a log mean temperature difference between the coolant and the process fluid. Equation *2.7* shows how ΔT_{LMTD} (K) is calculated (Vaessen, Seckler & Witkamp, 2004):

$$\Delta T_{LMTD} = \frac{T_{coolant,out} - T_{coolant,in}}{\ln\left(\frac{T_{coolant,out} - T_{bulk}}{T_{coolant,in} - T_{bulk}}\right)} \qquad 2.7$$

U is the overall heat transfer coefficient ($Wm^{-2}K^{-1}$) which is the inverse of the sum of the resistance to heat transfer that the system encounters in the process fluid, the wall and in the coolant. Equation *2.8* (Vaessen, Seckler & Witkamp, 2004; Welty et al., 2000) shows how U can be calculated from

$$\frac{1}{U} = \frac{1}{\alpha_{process}} + \frac{1}{\alpha_{coolant}} + \frac{1}{\alpha_{wall}} \qquad 2.8$$

where α is the convective heat transfer coefficient ($Wm^{-2}K^{-1}$). α can be described by

$$\alpha = \frac{1}{RA} \qquad 2.9$$

where R(K/W) is the thermal resistance to heat transfer which is determined by the type of heat transfer (conductive or convective), material properties (thermal conductivity) and heat transfer configuration (rectangular, cylindrical, or spherical) and A(m^2) is the heat transfer area.

The heat that the coolant absorbs can be calculated using equation *2.10*:

$$Q_{cool} = \dot{m}_{coolant} Cp_{coolant} (T_{coolant,in} - T_{coolant,out}) \qquad 2.10$$

$\dot{m}_{coolant}$ (kg s^{-1}) is the mass flow rate of the coolant, Cp (J $kg^{-1}K^{-1}$) is the heat capacity of the coolant. $T_{coolant,in/out}$ (K) is the temperature of the coolant into and out of the cooling jacket in a crystallizer. The amount of heat released by the process should be absorbed by the coolant. The heat absorbed by the coolant should allow for the feed to be cooled to the eutectic temperature (Q_{feed}) and for the ice and salt to crystallize out of solution (Q_{crys}). Any excess energy that the coolant gains is from the surrounding environment ($Q_{gain,\ calc}$). An energy balance for the crystallization process can be done and is shown by equation *2.11*:

$$Q = Q_{tot} = \mathrm{UA\Delta T_{LMTD}} + Q_{gain,m} = Q_{cool} = Q_{feed} + Q_{crys} + Q_{gain,calc} \qquad 2.11$$

The heat used to cool the feed, to form the solids and gained from the environment can be calculated using equations *2.12* to *2.14* below:

$$Q_{feed} = \dot{m_{feed}} Cp_{feed} (T_{feed,in} - \bar{T}_{products,out}) \qquad 2.12$$

where $\dot{m}$(kg s^{-1}) is the mass flow rate of the feed, Cp (J $kg^{-1}K^{-1}$) is the specific heat capacity of the feed, T_{feed} (K) is the inlet temperature of the feed and $\bar{T}_{products,out}$(K) is the average temperature of the products.

$$Q_{crys} = \dot{m}_{ice} \Delta\hat{H}_{crys,ice} + \dot{m_{salt}} \Delta\hat{H}_{crys,salt} \qquad 2.13$$

where $\dot{m}$(kg/s) is the mass flow rate of the ice/salt, $\Delta\hat{H}_{crys}$ (J kg^{-1}) is the specific heat of crystallization of ice/salt. The heat gained by the coolant can be calculated instead of being obtained experimentally as in equation *2.6*, using equation *2.14*:

$$Q_{gain,calc} = Q_{cool} - (Q_{feed} + Q_{crys}) \qquad 2.14$$

2.8 Magma Density

The magma density in a crystallizer is the solid content in the crystallizer(Mullin, 2001b).. The magma density is a direct result of the crystallization process and the conditions under which crystallization takes place and is measured as a percentage of the total mass of the contents of a crystallizer.

2.9 Hydrodynamics

The hydrodynamics of a system refers to the motion of a noncompressible fluid within the system(Schaschke, 2014). Hydrodynamics are important in crystallization as the motion of the brine allows for even and continuous distribution of supersaturation from the cooling medium to the rest of the brine. Fluid flow is induced by use of impellers which induce bulk/macro fluid flow. In the case where cooling is done indirectly through a surface, micro fluid flow at the surface where the fluid contacts the surface (the boundary) can further improve the hydrodynamics of a crystallizing system. In EFC scrapers are used for micro fluid flow as they disturb the fluid at the boundary, widely known as the boundary layer. Disturbance of the boundary layer ensures there are no areas with stagnant fluid. Stagnant fluid is undesirable as it results in the formation of an ice layer, i.e., the formation of a scale layer, which is further explained in section 2.10.

2.10 Scaling

In crystallization where cooling is done indirectly through a wall, the formation of an ice layer on the cooled surface of the crystallizer often occurs if no preventive action is taken. The ice scale layer forms a layer of insulation between the coolant and the process fluid which reduces the heat removal rate (Jooste, 2016). Reduction of the heat removal rate is undesirable as it lowers the rate of production of the components being crystallized. Ice scaling occurs either by heterogeneous nucleation or by ice crystals adhering to the cooled walls of the crystallizer.

Heterogeneous nucleation results from localised supersaturation at the wall and often occurs when a thermal boundary layer forms between the wall and the bulk fluid. This layer of fluid tends to be colder than the bulk fluid as the wall is in direct contact with the coolant. The result is that this layer is at a high supersaturation, and the high supersaturation drives the heterogenous nucleation (Qin, Chen & Russell, 2003).

Ice adheres to solid surfaces. At higher driving forces, ΔT_{LMTD}, the rate of production of ice is high. This results in a high number of crystals in the crystallizer, so the chance of adhesion is high. At these conditions the wall is also colder, and ice adheres more strongly at lower temperatures (Petrenko, 1993).

Scrapers (section 2.13) have been developed to disturb the thermal boundary layer periodically and avoid localised supersaturation at the wall. Scrapers can also remove the ice scale layer from the walls of the crystallizer if one has already formed. This scraping can reduce the effect of the scale layer on heat removal. Scrapers may be unable to remove the scale layer if it is too thick or if the scrapers move too quickly.

2.11 Separation of ice and salt

After cooling, separation is first achieved by the crystallization of ice and salt from aqueous solution. After the two solids crystallize out of solution and are suspended in the bulk, gravitational separation takes place because of differences in densities: ice floats and salts sink. This allows for separate harvesting of ice and salt, with salt harvested at the bottom of the crystallizer and ice at the top.

The purity of the products in EFC is a function of the efficiency of the solid-solid-liquid separation of the system. Theoretically, high degrees of purity should be achievable because the first form of separation occurs when the crystals form. Crystal lattices reject impurities due to the differences in the size and shape of the molecules (Mullin, 2001b). However, in practice, some impurities are found in the product. These impurities can come from the entrainment of small crystals, because fine crystals of an impurity are transported along with larger crystals of the product as they flow. Impurities can also come from the products’ crystals being small. Small crystals tend to agglomerate and in doing so, crystals of impurities or mother liquor is entrapped in the spaces between the fines during agglomeration. Impurities can also be found in the product due to poor gravitational separation. Gravitational separation is one of the key steps after crystallization as it allows for the physical separation of the solids produced. If the gravitational separation is poor, the purity will be low as the product will be harvested as a mixture.

2.12 Crystallization operation

Crystallization can be operated in batch or continuous mode. These are explained below.

2.12.1 Batch crystallization

In batch crystallization, the solution is fed to the crystallizer and is subjected to cooling for a period that ensures crystallization occurs. The crystals are only harvested at the end of running the batch, (Myerson, 2002) and then sent to a batch solid-liquid separation step (Lewis et al., 2015). In batch crystallization, the liquid being treated spends a specific length of time in the crystallizer: the batch residence time. Myerson (2002) states that batch crystallization is mainly used in the pharmaceutical and photography industry. Batch crystallization is also used for industrial plants that process more than one feed (Lewis et al., 2015).

2.12.2 Continuous crystallization

For continuous crystallization, a solution is continuously fed to the crystallizer and is subjected to cooling to allow crystallization to take place. The formed solids are kept in suspension by agitation and the resulting slurry is continuously removed as a product stream and sent to a solid-liquid separation step such as a centrifuge or filter (Lewis et al., 2015). The average time that is spent in the crystallizer before leaving the crystallizer, residence time τ, can be defined as shown in equation **2.15** :

$$\tau = \frac{V}{\dot{V_{in}}} \qquad 2.15$$

where τ (min) is the residence time, V(m^3) is the volume of the crystallizer and $\dot{V_{in}}$ (m^3/min) is the feed flow rate into the crystallizer. Continuous crystallization is used for the processing of one feed type, as well as large capacities (Lewis et al., 2015).

2.13 Types of crystallizers

There are two main types of crystallizers used in laboratory work. The crystallizers are the scraped, cooled-wall crystallizer, SCWC, and the cooled, disc-column crystallizer, CDCC.

2.13.1 Scraped cooled-wall crystallizer, SCWC

Figure 2.3 and

Figure 2.4 show schematics of the two models of the SCWC used in previous studies.

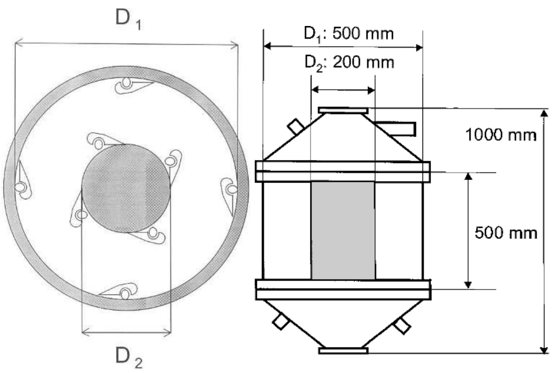

Figure 2.3: SCWC-1 top and side view, taken from Vaessen et al. (2003)

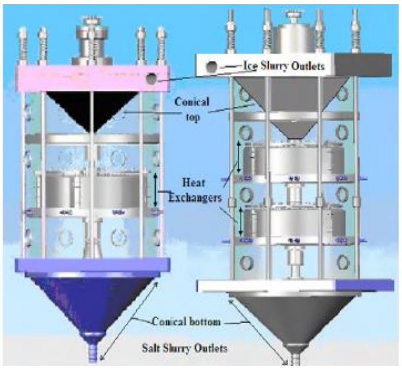

Figure 2.4: SCWC-2, taken from Rodriguez-Pascual et al. (2010)

The first model is a vessel that has a jacketed cooled wall with scrapers on the inside to remove ice-scale layers that form on the wall. It also contains a cooled cylinder in the centre of the vessel to allow for further cooling. The cylinder, too, is scraped. The second model does not have a cooled jacket wall, but rather scraped heat exchangers in the centre of the crystallizer. The scrapers used in both models are wing-shaped and shown in Figure 2.5.

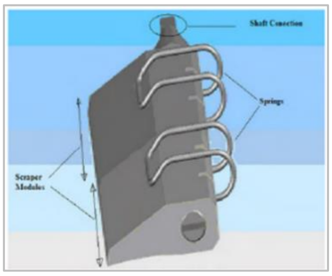

Figure 2.5: Winged shaped scraper used in SCWCs.

2.13.2 Cooled disc-column crystallizer, CDCC

Figure 2.6 and Figure 2.7 show an open view and a general schematic of the CDCC. There have been three models developed for laboratory use, and the main differences lie in the number of disks and compartments they have. Here the scrapers are flat, as can be seen in Figure 2.6.

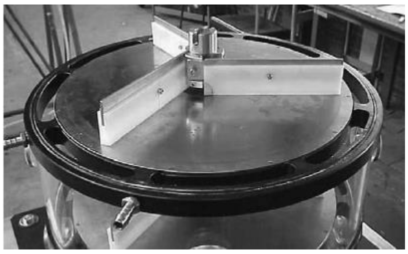

Figure 2.6:Open view of CDCC-1 taken from Vaessen, Seckler and Witkamp (2004)

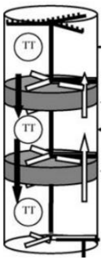

Figure 2.7: Schematic of CDCC taken from (Genceli, Gärtner & Witkamp, 2005)

The fundamental theory which applies to EFC was discussed in this chapter. The concepts discussed here were used in understanding and discussing the work carried out by others (discussed in Chapter 3). The theory discussed here, in combination with the literature review was used to formulate the key questions and hypotheses for this study, and for the interpretation of the results from the experiments.

3 LITERATURE REVIEW

3.1 Production performance in EFC

Eutectic freeze crystallization is a promising separation technique as it should theoretically achieve 100% separation of solute from solvent at a fraction of the energy requirements. Van der Ham et al. (1998) and Vaessen (2003) found that using EFC to treat brines require 70% less energy than the use of evaporative crystallization. Eutectic freeze crystallization is often used in combination with reverse osmosis as the hybrid set up allows for maximization of yield(Randall, 2011) at reduced energy consumption. Theoretically the use of EFC should achieve 100% separation and in turn ensure that a separation by EFC yield high production rates, however, practically this has not been achieved.

Heat transfer is the driving force for EFC, so the absence of complete separation and high production capacity is due to heat transfer limitations. Theoretically the maximization of heat transfer should come from the maximization of the heat transfer driving force, heat transfer coefficient and heat transfer area. There are studies that corroborate the theoretical effect of heat transfer area on production rate(Genceli, Gärtner & Witkamp, 2005; Genceli et al., 2005) however other studies have shown that the maximization of heat transfer driving force does not only result in the expected theoretical outcome but gives rise to phenomena which limit the production capacity of a crystallizer (Vaessen, Seckler & Witkamp, 2004). The most common limiting phenomenon is the formation of an ice scale layer on the cooled wall of a crystallizer which dampens heat transfer between the coolant and the bulk fluid. There are studies on understanding how the scale layer forms(Motsepe, 2020), how operating conditions affect the formation of the scale layer(Leyland, Chivavava & Lewis, 2019) as well as studies where scrapers were used to mitigate the effects of the scale layer(Rodriguez-Pascual et al., 2010; Vaessen, Seckler & Witkamp, 2004). A common finding in these studies was that the scale layer became larger as the heat transfer driving force increased. This is undesirable as high heat transfer driving forces are required for high production capacities. Therefor it is necessary to further understand factors that affect the production of ice and salt as well as find more methods to mitigate the effects of the scale layer in order to achieve high production rates.

Since EFC is a separation technique, the purity of the products is important. Studies into the effects of operating conditions on purity of ice and salt show that gravitational separation(Randall, 2010; Rodriguez-Pascual et al., 2010), crystal formation and in turn crystal size play a role in the resulting product purity. The control of crystal formation and size for salt is widely covered in literature however the same can’t be said for ice. It is therefore necessary to understand the effect of ice crystal formation and size on ice purity.

Achieving high production rate and purity of the products consistently, without stoppages, is a desired outcome for the EFC process. This standard has not been reached, and studies are being conducted to understand the phenomena that block progress in the process. This understanding would allow for better application and control of the separation technique needed for high, consistent production. This chapter reviews some of the studies on the operating conditions that affect product purity and production rate. The literature review will be used as the basis for the hypotheses formed

3.2 Factors affecting production rate.

Heat transfer rate drives EFC and determines the production capacity of a crystallizing system so it is important to understand the factors that influence heat transfer. The heat transfer rate is determined by the heat transfer driving force, ΔT_{LMTD}, the heat transfer area, A and the heat transfer coefficient, U. Thus, it is important to understand the relationship between ΔT_{LMTD} , A and U, and the production rate through the heat transfer rate.

3.2.1 Heat transfer area

Heat transfer rate is directly proportional to heat transfer area. Changing the crystallizer type changes the area available for heat transfer. Genceli, Gärtner and Witkamp (2005) and Genceli et al. (2005) evaluated the performance of the second and third models of the CDCC. The heat transfer data obtained is summarised in

Table 3.1. It can be seen that the crystallizer with the larger heat transfer area achieved higher heat transfer rates. –Even though many of the operating conditions, including ΔT_{LMTD} and residence time, were different for the studies using the two crystallizers, it can be concluded that increasing the heat transfer area did contribute to the increase in the heat transfer rate.

Table 3.1: CDCC heat transfer data

Model	**Capacity**	**Area**		**Residence time**	**ΔT_{LMTD}**	**Max Q**
	L	m^2/m^3	m^2	hrs	K	kW
2	150	5.6	0.84	1.3	6.42	3.25
3	220	7.7	1.69	0.5	7.5	6.48

3.2.2 Heat transfer driving force, ΔT_{LMTD}.

Heat transfer rate is directly proportional to heat transfer driving force, ΔT_{LMTD} . Vaessen, Seckler and Witkamp (2004) and Genceli et al. (2005) in their studies using the first model of the SCWC and the third model of the CDCC, showed that for different mother liquors, an increase in ΔT_{LMTD} accelerates the heat flux, q (heat transfer rate per unit area), which in turn raised the production rate of ice and salt. This shown in Figures 3.1 to 3.4.

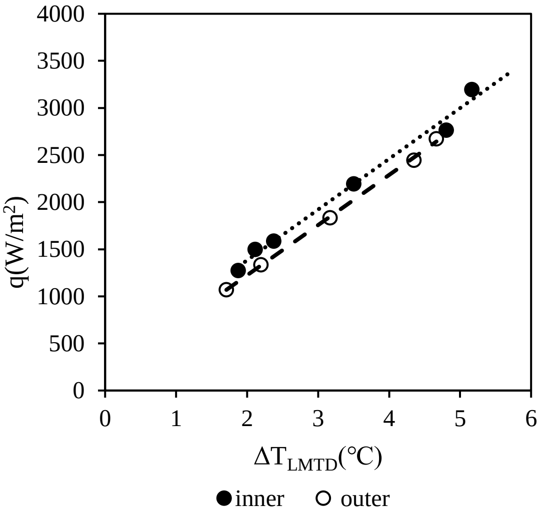

Figure 3.1: Effect of ΔT_{LMTD} on heat flux for KNO_3 solution in the SCWC-1, redrawn from Vaessen, Seckler and Witkamp (2004) & Vaessen et al. (2003)

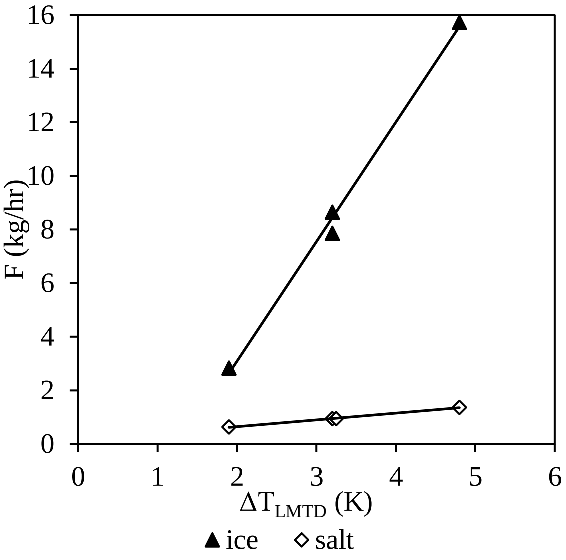

Figure 3.2: ΔT_{LMTD} vs product flow for KNO_3 solution in the SCWC-1, redrawn from Vaessen, Seckler and Witkamp (2004) & Vaessen et al. (2003)

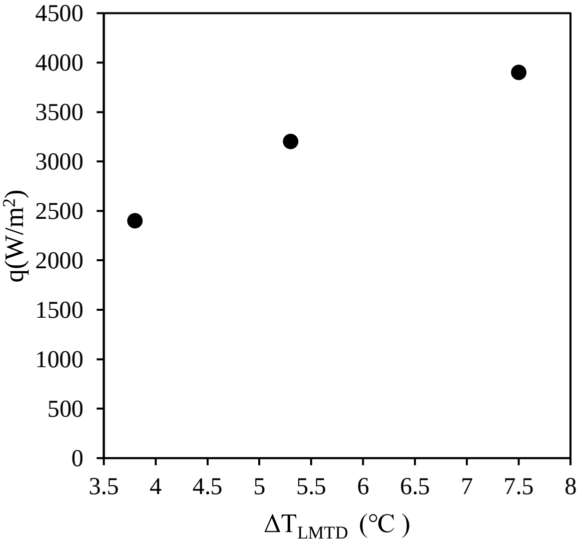

Figure 3.3: Effect of ΔT_{LMTD} on heat flux for $MgSO_4$ solution in the CDCC-3, adapted from Genceli et al. (2005)

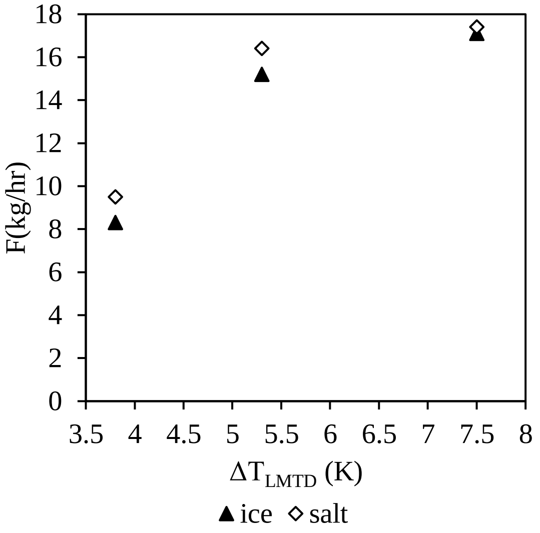

Figure 3.4: Effect of ΔT_{LMTD} on product flow for $MgSO_4$ solution in the CDCC-3, adapted from Genceli et al. (2005)

This proportional relationship is expected because a higher ΔT_{LMTD} allows for a high heat transfer rate which increases the crystallization rate. An increase in crystallization rate is reflected in faster production of ice and salt. Figure 3.3 and

Figure 3.4 show different ranges for ΔT_{LMTD}. For the range where ΔT_{LMTD}<5.3 K, both graphs show that increasing the ΔT_{LMTD} increases the production rate. For the range where ΔT_{LMTD} >5.3 K,

Figure 3.4 shows an increase in production rate with increasing ΔT_{LMTD} but the increase is less steep. This may suggest that if the ΔT_{LMTD} was to be increased further, the production rate could either remain constant or drop, but there is only one data point after ΔT_{LMTD}=5.3K, so the data is not sufficient to conclude this confidently. In the study by Rodriguez-Pascual et al. (2010) ΔT_{LMTD}s as large as10.8 ℃ were applied, but the residence time, feed and coolant flowrate were all varied simultaneously. A comparison of the production rates could not be made as it is not clear which factor contributed to the observed changes.

3.2.3 Heat transfer coefficient

Another factor that affects heat transfer rate is the heat transfer coefficient. In a crystallizer where the heat transfer area and ΔT_{LMTD} are constant, a measure of heat transfer is the heat transfer coefficient, U. The heat transfer coefficient had been found to be affected by coolant flow rate, vessel wall thickness, and agitation/scraper speed, because they affect the heat transfer on the coolant side, wall, and bulk fluid respectively (equation *2.8*). The hydrodynamic conditions of a crystallizing system have also been found to be affected, in a more indirect manner, by $\Delta T_{LMTD.}$

Vaessen, Seckler and Witkamp (2004) found that higher coolant flow rates resulted in higher heat fluxes that resulted from a reduction in the coolant heat transfer coefficient, $\alpha_{coolant}$, which was found to be dependent on the coolant flow rate. A reduction in $\alpha_{coolant}$, increased the U, resulting in greater heat flux. Altering the thickness of the crystallizer wall, as well as the material of construction, such that the thermal conductivity was altered, also affected U (equation *2.8*).

Another factor that affects U is the heat transfer coefficient of the process fluid, $\alpha_{process}$. In the work done by Vaessen, Seckler and Witkamp (2004) using the model of the CDCC, the ΔT_{LMTD} was increased. The scraper rate was also increased to match the increase in $\Delta T_{LMTD.}$ It was found that higher scraping rates resulted in higher values of $\alpha_{process}$. This change happened because scraping at a faster rate disturbed the boundary layer, thereby distributing supersaturation more efficiently and preventing the formation of a scale layer. In the work carried out by Jooste (2016), the scraper rate was varied and though $\alpha_{process}$ was not quantified, the heat transfer rate was. It was found that the heat transfer rate increased with a faster scraper rate.

Faster scraping rates result in higher Reynolds numbers. Reynolds number, *Re*, is a dimensionless number used to categorize the flow pattern of fluids. For a scraping system, it is calculated using equation *3.1*:

$$Re = \frac{\rho N_{scraper} D_{scraper}^2}{\mu} \tag{3.1}$$

where ρ is the density of the process fluid, $N_{scraper}$ and $D_{scraper}$ are the scraping rate and diameter of the scraper blades respectively, and μ is the process fluid's dynamic viscosity. A higher Re means more turbulent flow. Turbulence results in more effective disturbance of the boundary layer fluid at the cooled wall. Disturbance of this layer prevents the formation of a scale layer as the supersaturated fluid is thrust into the bulk fluid. Thus, a higher scraping rate was found to increase the values of $\alpha_{process}$ and in turn, heat transfer rates.

The same tests were conducted in the SCWC as in the CDCC by Vaessen, Seckler and Witkamp (2004). Here it was found that increasing the scraping rate and ΔT_{LMTD} decreased the values of αprocess. Upon closer investigation, it was found that when the scraping rate was kept constant, an increase in ΔT_{LMTD} caused an increase in the solid content in the bulk. The high solid content, i.e, the magma density, altered the hydrodynamics of the system. When there was more solid content the flow of the bulk fluid around the scrapers was found to be negligible. The reduced flow in combination with the colder wall (at the higher ΔT_{LMTD} the walls were colder) led to scale formation, most likely by a combination of heterogenous nucleation and adhesion. The formation of this scale layer when there was more solid content caused the decrease in the heat transfer coefficient. The scrapers were unable to remove the scale. The observed changes are listed in Table 3.2.

Table 3.2: Effect of magma density on heat transfer in a KNO_3-HNO_3 system tested in the SCWC-1

SCWC-1 KNO_3-HNO_3 system				
N (rev/s)	ΔT_{LMTD} (K)	Product solid content (wt.%)	$\alpha_{process,outerwall}$ (kW/m^{2}K)	$\alpha_{process,inner\ cylinder}$(kW/m^{2}K)
0.71	3.2	6	3.9	4
0.71	4.8	10	3.0	3.2

Rodriguez-Pascual et al. (2010) achieved 42 wt.% solid in the crystallizer before scaling occurred. This can be attributed to the change in the crystallizer design. The scrapers used by Rodriguez-Pascual et al. (2010) and Vaessen, Seckler and Witkamp (2004) were wing-shaped, but the ones used by Rodriguez-Pascual et al. (2010) allowed for an increased normal force on the heat exchanger surface so as to be able to scrape under a scale layer better and lift it off the cooled surface. This shows that the limit that ΔT_{LMTD} can have on the heat transfer coefficient is specific to the system being treated as well as crystallizer design. If the design used by Rodriguez-Pascual et al. (2010) had been used by Vaessen, Seckler and Witkamp (2004), the increase in ΔT_{LMTD} might have increased the magma density, but the increase in magma density would not have caused a reduction in the heat transfer coefficient as the ice would have been kept off the wall.

3.2.4 Magma density

The magma density imposes limitations on heat transfer by causing changes to the hydrodynamic properties of the system. This ultimately affects the production rate of the resulting salt and ice. However, magma density is coupled with heat transfer in that a heat transfer driving force is required to create the solids that make up the magma, but once they are formed, they impose limitations on any further heat transfer from the process fluid to the coolant by increasing the probability of scaling.

Leyland, Chivavava and Lewis (2019) determined a relationship between magma density and the scaling potential of a system. The relationship was separated into three regions as seen in Figure 3.5. The figure shows that the scaling potential is high when the magma density is very low or very high.

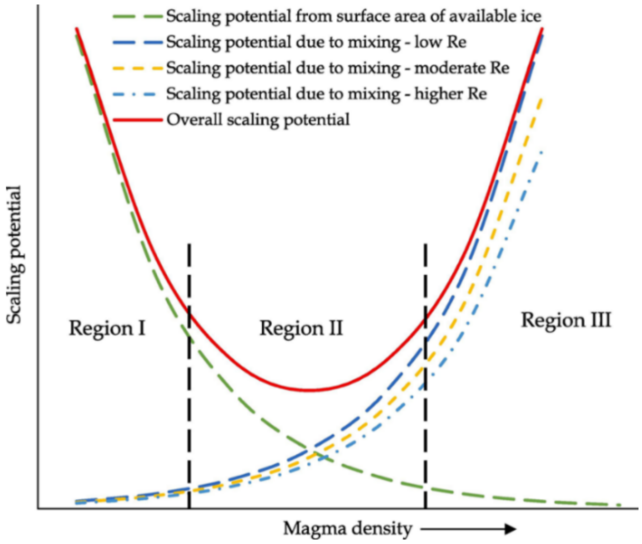

Figure 3.5: Relationship between magma density and scaling potential, taken from Leyland, Chivavava and Lewis (2019)

Leyland, Chivavava and Lewis (2019). These researchers formulated that at low magma density, there is little surface area for growth in the bulk, which promotes heterogeneous nucleation on the wall, and therefore the scaling potential in Region I is high. As magma density increases, the system shifts from region I to Region II where the scaling potential is minimised. The scaling potential decreases because the solids in the bulk provide more surface area for crystallization in the bulk. Increased surface area available for crystallization in the bulk increases the rate of consumption of supersaturation, leaving little supersaturation at the wall, reducing the tendency for heterogeneous nucleation. Further increase in the magma density increases the scaling potential, as high magma densities affect the hydrodynamics of the system. In Region III, the magma density is high, increasing the viscosity of the bulk. The efficiency of mixing is reduced when the viscosity of the bulk is high. Efficient mixing is required for the solution to contact the cooled wall. Reduced contact between the wall and the solution results in the walls becoming colder leading to high supersaturation next to the wall. This results in heterogeneous nucleation, hence the high scaling potential.

Systems in Regions I or III lead to scaling. Scaling dampens heat transfer by reducing the overall heat transfer coefficient. This in turn, reduces production rate. It is therefore desirable to operate at magma densities that fall within Region II where scaling is minimised.

3.2.5 Scale layer formation

The heat transfer driving force determines the magma density of the system which in turn affects the heat transfer coefficient through scaling. It is therefore important to know when the onset of scaling happens in a system to prevent or minimise it. This was done by Leyland, Chivavava and Lewis (2019) where the onset of scaling was measured at different driving forces. It was found that operating at higher driving forces resulted in scaling occurring in a shorter time, which was termed scaling induction time. Having shorter scaling induction means thermal resistance is introduced into the system earlier,resulting in prolonged inefficient heat removal. The overall heat transfer coefficient is reduced. Referring to equation *2.8* in Chapter 2, there would be an added term as seen in equation *3.2*:

$$\frac{1}{U}=\frac{1}{\alpha_{process}}+\frac{1}{\alpha_{coolant}}+\frac{1}{\alpha_{wall}}+\frac{1}{\alpha_{scale}} \qquad 3.2$$

When there is no scale layer there is no resistance to heat transfer that it causes, however, once it is there, an increase in the scale layer results in an increase in heat transfer resistance thereby causing a reduction of α_{scale}. This results in a reduction of the overall heat transfer coefficient.

Reducing the overall heat transfer coefficient reduces the heat removal rate, which in turn reduces the production rate of ice and salt in the bulk.

3.3 Factors affecting purity.

The purity of the products in EFC depends on how well the ice and salt separate. Separation depends on the efficiency of gravitational separation as well as on how the crystals grow when supersaturation is consumed for crystallization. To achieve the best possible purity, the factors that affect gravitational separation must be understood and then exploited.

3.3.1 Gravitational separation

3.3.1.1 Magma density

The magma density imposes limitations on gravitational separation which affects the purity of the products. A magma density that is too high makes it difficult for ice to float or salt to settle. The product slurries will be a mixture of ice and salt, resulting in a poor product purity.

The crystallizer that was tested by Rodriguez-Pascual et al. (2010) could contain up to 42 wt.% solids without difficulty in gravitational separation. For the work done by Randall (2010), this limit was 30 wt.%. The two values are different due to the differences in the systems. These are listed in Table 3.3.

Table 3.3: Experimental characteristics of different studies

	Rodriguez-Pascual et al. (2010)	**Randall (2010)**
Brine system	$NaHCO_3$-Na_2CO_3-H_2O	Na/K/Ca-SO_4-H_2O
Concentration	4.5 wt. % $NaHCO_3$; 5.2 wt.% Na_2CO_3	59.2 g/l
Crystallizer type	SCWC-2	Stirred-cylindrical crystallizer
Operational Mode	Continuous	Batch
Crystallizer volume	130L	1.5L

A significant difference between the two systems was the design of the crystallizers. The crystallizer used by Randall (2010) was much smaller than the one used by Rodriguez-Pascual et al. (2010). The latter crystallizer therefore had more space for ice to float and salt to sink which allowed more solids to separate before gravitational separation became poor.

In the work done by Rodriguez-Pascual et al. (2010), the gravitational separation was also aided by the internal heat exchanger that created a temperature gradient that made the top and bottom sections warm. The warm sections ensured partial melting of ice agglomerates so that entrained salt would settle and entrapped ice would float, whereas separation in the crystallizer used by Randall (2010) depended solely on the difference in densities in the crystallizing components. From this finding, it can be concluded that a high magma density can be achieved while avoiding limitations on gravitational separation if the crystallizer is well-designed. The best results can be achieved when the operation is carried out at a magma density that allows for maximisation of production rate without compromising separation and product purity.

3.3.1.2 Product size

Ice and salt crystals need to be large for separation to be efficient. The probability of entrainment is reduced when the crystals are larger. It is therefore necessary to identify the factors that affect the product size in crystallization. It is known that when growth is dominant, the resulting product is made up of large crystals, while systems that are nucleation dominated produce fine crystals. Seeds are often used to initiate the crystallization process. It is important to understand how the amount used when seeding (seed loading and seed size) affects product size as that determines whether growth or nucleation is dominant.

3.3.1.2.1 Seed loading

Seed loading can be used to control the size of product ice and salt. The choice of the seed-loading ratio is dependent on the crystallization goal i.e. growth or nucleation. Doki et al. (1999) carried out an investigation into the effects of scaling up seeded batch crystallization of potassium alum. The different conditions that were tested are summarised in Table 3.4.

Table 3.4: Experimental conditions tested by Doki et al. (1999)

Seed size (µm)	**Solution Concentration (g/gH$_2$O)**	**Cs**	
315	0.1; 0.15	0.0051	0.25
41.5		0.00051	0.00337

It was found that regardless of the crystallizer size, seed size or solution concentration, the higher seed loading ratio resulted in a unimodal product crystal size distribution (CSD) and the lower seed loading ratio resulted in a wide-spread, bimodal product CSD. The unimodal CSD showed that there was growth of the seeds while the bimodal CSD showed that there was nucleation and growth.

A low seed loading provides low crystal surface area for growth. In the investigation of seeding and cooling on the batch crystallization of potassium alum, Hojjati and Rohani (2005) showed that regardless of the cooling mode, cooling results in high supersaturation in the first 1000s of the experiments. This supersaturation can either be consumed by deposition of mass on crystal surface, in other words, by growth of seed crystals or by nucleation, which is the birth of crystals. If the seeds provide enough surface area, growth will be dominant and if not, growth will still occur, but nucleation will occur as well so that the supersaturation is consumed.

A low seed loading induces secondary nucleation which explains why a widespread and bimodal CSD was obtained. A high seed loading provides sufficient seed surface area to maintain a low supersaturation which allows for growth (Lewis et al., 2015), hence the unimodal CSD. It is possible that at very high seed loadings contact breeding might become more prevalent, but this is not detailed in the literature. Seed loadings are often kept low so as not to take up a large proportion of the crystallizer. Lung-Somarribaa et al. (2004) consolidated the findings from the work by Doki et al. (1999) by showing that different seed loadings provide different seed surface area, as given by

$$S = \frac{W_S k_a}{\rho k_v L_s} \qquad 3.3$$

where S (cm^2) is the seed surface area, k_a is the area shape factor of the crystals, k_v is the volume shape factor of the crystals, ρ is the density of the crystals (g/cm^3), and L_s is the seed size.

For every species, there exists a seed loading ratio where the ratio of the theoretical product size to seed size, $\frac{L_{sp}}{L_s}$, is the same as the experimental ratio of the product size to the seed size, $\frac{Lw_p}{L_s}$. Graphically, this point is where the line of $\frac{L_{sp}}{L_s}\ vs\ C_S$ intersects the line of $\frac{L_{wp}}{L_s}\ vs\ Cs$. The graph of $\frac{L_{sp}}{L_s}\ vs\ C_S$ can be determined by solving for $\frac{L_{sp}}{L_s}$ in equation **2.4** which gives

$$\frac{L_{sp}}{L_s} = \left(\frac{1 + C_S}{C_s}\right)^3 \qquad 3.4$$

The seed loading where the two lines meet is the critical seed loading ratio, C_S^* (Doki et al., 1999). The critical seed loading ratio gives a seed mass that provides the critical surface area, S_c, required for growth. Doki et al. (2002) developed an equation relating C_s^* and seed size. This is shown as

$$C_s^* = 2.17 \times 10^{-6} L_s^2 \qquad 3.5$$

Crystallization carried out using a $C_S > C_S^*$ results in growth of the seeds while using a $C_S < C_S^*$ results in growth and nucleation. Lung-Somarribaa et al. (2004) showed that regardless of the seed size, when the seeds provided $S<S_c$, the product size was much smaller than the theoretical product size, once again proving the lack of growth. This same conclusion was made from the point of view of supersaturation by Hojjati and Rohani (2005) as the results showed that increasing the seed loading beyond C_S^*, reduced the initial increase in supersaturation in the first 1000s of the experiment, leading to a unimodal CSD which showed that growth was dominant.

Referring back to the work done by Doki et al. (1999), it can be concluded that for 315 and 41.5 µm seeds, the seed loading ratios 0.25 and 0.0037 were larger than the critical seed loading ratio as they resulted in growth.

The work by Doki et al. (1999) was for cooling crystallization but earlier, Kaboyashi and Shirai (1996) studied the effect of ice seed loading on the product size in the freeze crystallization of ice from a glucose solution and found that the concept of critical seed loading (though it was not termed that at the time) also applied to ice. Ice seed loadings of 3,6 and 12 wt.% (w_s/w_l-mass of seeds/mass of liquid) were used. It was found that the size distribution of the ice product for 3 wt.% was unimodal and smaller than the seeds, the size distribution for 6 wt.% was bimodal, and the size distribution for 12 wt.% was unimodal and larger than the seeds. The size distributions are illustrated in Figure 3.6.

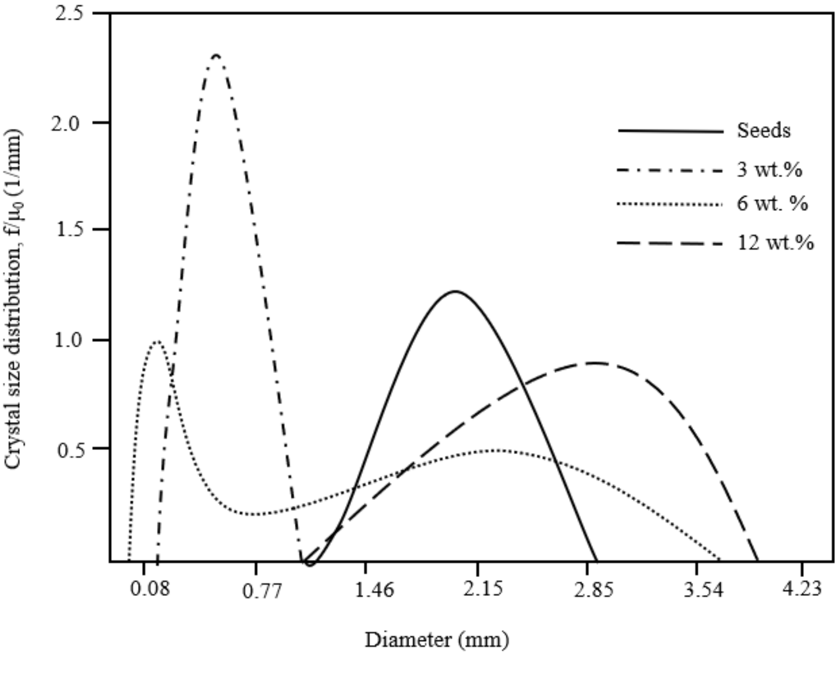

Figure 3.6: Product CSD of ice, adapted from Kaboyashi and Shirai (1996)

This means that at 3 wt.%, nucleation was dominant, at 6 wt.% nucleation and growth occurred and the critical seed loading for this system was 12 wt.% as growth was dominant. Kaboyashi and Shirai (1996) however, concluded that using a seed loading of 6 wt.% or more resulted in large, agglomerated ice crystals. This conclusion shows that eliminating nucleation was not a concern for Kaboyashi and Shirai (1996), so 6 wt.% would suffice in future use of seed for product size control.

There was no target in terms of growth and nucleation in the work done by Doki et al. (1999) as the aim was to investigate a range below and above the C_S^* or S_c^*. In most batch crystallization in industry the desired product size dictates whether growth or nucleation is to be targeted. In the case of continuous EFC however, the C_S would have to be one that yields a good balance of nucleation and growth. Growth is needed so that ice and salt are big enough to float and settle, giving high product purity, while nucleation is required for the birth of crystals that would act as seeds for the fresh feed at low supersaturation, i.e. within the metastable zone. However, after the initial seeds have been added, the system would become self-seeding, making the seeds important only for the induction of crystallization within the metastable region.

3.3.1.2.2 Seed size

It has been found that seed size affects final product size. Table 3.5 shows data at a constant Cs value of 10^{-2} for different seed sizes for crystallization of potassium alum in batch operation (Doki et al., 2002). The product became larger when the seed size was increased from 42 to 165 μm. When seeds larger than 165 μm were used, the product became smaller. The increase in product size for seeds of sizes below 165 μm may have been because the seeds were growing and since the seed size was increasing, the larger seeds grew bigger. This effect becomes less significant for seeds of size larger than 165 μm as breakage by impact becomes more prevalent. Larger seeds would grow to larger sizes but crystals of larger sizes experience higher impact from the impeller. This would lead to breakage which results in smaller products.

Table 3.5: Product size for every seed size adapted from Doki et al. (2002)

Ls (μm)	$\frac{L_{wp}}{L_s}$	Lw_p (μm)
42	5	210
60	4.7	282
165	2.9	479
328	1.1	361
550	0.7	385

Lung-Somarribaa et al. (2004) found that when larger seed sizes were used, the resulting product had broken vertices by attrition and this significantly reduced the actual product size to the point where it was much smaller than the theoretical. Lung-Somarribaa et al. (2004) suggest that if the L_{sp} of the specific seed size is larger than the maximum achievable product size when no seeds are used, attrition will become more prevalent. This suggestion shows that Lung-Somarribaa et al. (2004) believed the product size was a result of the competition between growth and attrition. Larger seeds are more susceptible to attrition than smaller seeds, leading to the recommendation for the use of small seeds in batch cooling crystallization. This recommendation is applicable to EFC, for salt seeding, as the growth of the crystals promotes gravitational separation of the crystals.

Eder et al. (2011) investigated the effect of seed size on the production of acetylsalicylic acid (ASA) crystals in a 15 m tubular crystallizer. An ethanolic suspension with ASA seeds was continuously fed into a tubular crystallizer after being mixed with an ethanol solution that had a high concentration of ASA. It was found that for a constant seed loading of 0.05g/$ml_{suspension}$, increasing the seed size from 132 μm to 184 μm, increased the product size by 98 μm. This increase indicates that 184 μm seeds allowed for the increase in product size without inducing increased impact, in this case with the crystallizer wall rather than an impeller. Perhaps the absence of an impeller allowed for this increase. This sheds light on the need for careful consideration not only of the seed size but of the seeding mechanism, as well as crystallizer design.

The studies by Doki et al. (2002) and Lung-Somarribaa et al. (2004) were for cooling crystallization which means only salt crystallized out of solution. Kaboyashi and Shirai (1996) on the other hand, carried out work on freeze crystallization of ice from a 10 wt.% glucose solution. The experiments were carried out using seeds that were 0.8 mm and 2.2 mm. It was found that both seed sizes resulted in large, agglomerated product ice crystals, with the 2.2 mm crystals producing a slightly wider size distribution. This is illustrated in Figure 3.7

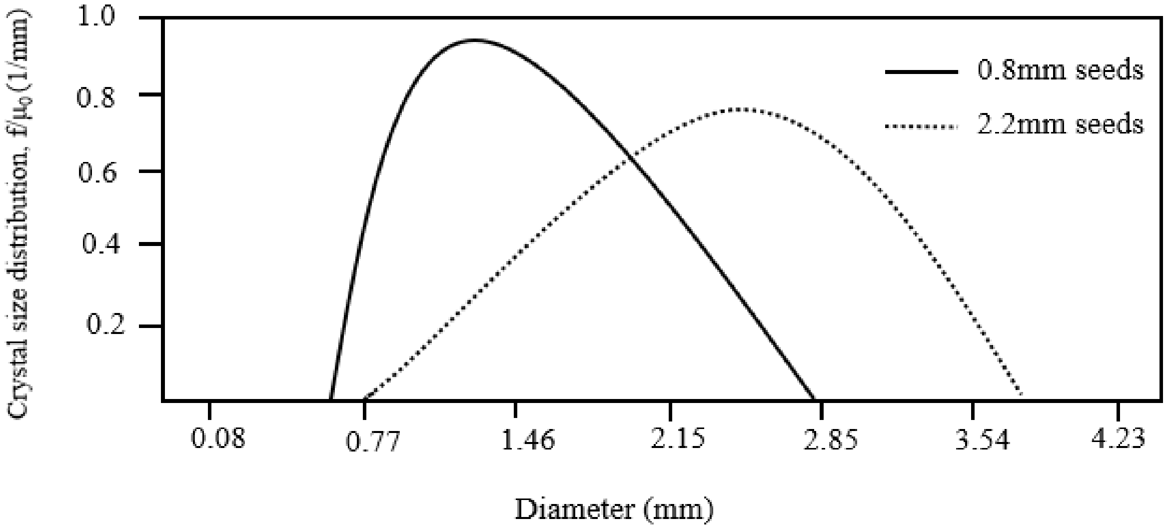

Figure 3.7: Product ice CSD when different seed sizes were used, adapted from Kaboyashi and Shirai (1996)

The ice seeds used here were much larger than the entire seed size range tested by Doki et al. (2002). It is interesting to note that for ice, no product size reduction was observed when large seeds were used. This may be due to the rigid structure of the ice lattice or the fact that the ice would float and be away from the impellers during crystallization thereby reducing the effect of attrition on the ice. This suggests that the recommendation by Lung-Somarribaa et al. (2004) to use small seeds is not applicable to ice seeding.

3.3.2 Supersaturation , crystal growth and entrapment of impurities

Product purity is affected by the supersaturation as the supersaturation affects nucleation and crystal growth (Dhanaraj et al., 2010). When supersaturation is high, nucleation occurs, and the resulting product is fine. When the supersaturation is low, growth occurs, and the resulting product is large(Kadi & Janajreh, 2017).

In addition to supersaturation determining whether nucleation or growth occurs, supersaturation determines whether the growth is rough or smooth (Lewis et al., 2015). Crystal growth determines the intensity of impurity entrapment. Rough growth occurs at high supersaturation and leaves room for entrapment of impurities as the crystals grow. Entrapment of impurities reduces the purity of products.

Shirai et al. (1999) investigated the effect of ice seeds on the purity of the product. This work was done in batch mode on a synthetic industrial waste stream that contained polypeptone. Shirai et al. (1999)The investigators showed that in the absence of seeds, the supersaturation was high, which resulted in one of the most common forms of rough growth, dendritic growth. Impurities were trapped between the dendrites before the supersaturation was low enough for smooth layered growth to start. This is illustrated in Figure 3.8.

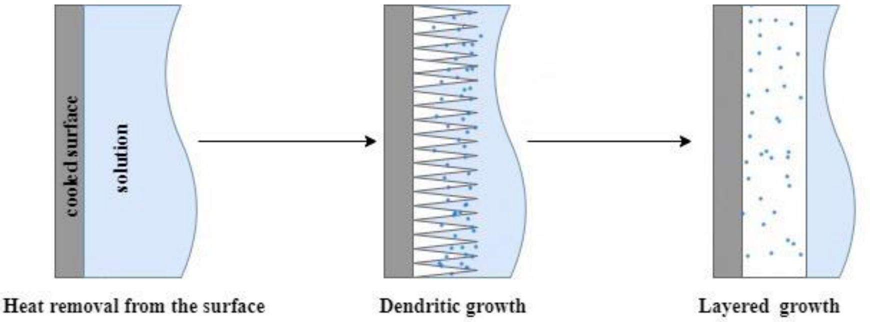

Figure 3.8: Illustration of growth of ice on a surface adapted from Shirai et al. (1999)

The aim of the work was to remove polypeptone from the solution, but the ice produced still had just over 30 % of the polypeptone from the original solution. If the growth had been layered from the initiation of crystallization, the ice would have been purer. Kapembwa, Rodríguez-Pascual and Lewis (2014) corroborated the findings by Shirai et al. (1999) in that the researchers found that high subcoolings (>2.8 °C) resulted in high growth rates which resulted in dendrites. It was also found that growth shifted from dendritic growth to layered growth with time as the supersaturation was consumed when heat of crystallization was released.

The work done by Shirai et al. (1999) and Kapembwa, Rodríguez-Pascual and Lewis (2014) was a batch operation where the crystals grew on a surface. In the case of continuous crystallization, growth of crystals in the bulk is desirable. Continuous crystallization allows for the maintenance of low supersaturation, which is achieved by the production and consumption of supersaturation that occurs in a continuous system (Hofmann & Melches, 2013). The supersaturated solution in the crystallizer is mixed with the undersaturated feed solution. The mixed solution is cooled beyond the eutectic point and crystallization occurs. The cooling produces the supersaturation, which is consumed by crystal growth. This cycle continues and this is how a low supersaturation is maintained. At low supersaturation the likelihood of rough growth occurring is low, so purity is less likely to be affected by rough growth.

3.3.2.1 *Seeding, supersaturation, and purity*

Supersaturation determines whether growth is rough or smooth (Lewis et al., 2015). When the supersaturation is high, the growth is rough and allows for dendrites to form. Dendrites trap impurities as the growth shifts from rough to smooth. Introduction of seeds allows crystallization to be induced at low supersaturation which leads to smooth-layered growth to be dominant. This process reduces the entrapment of impurities. These two cases are illustrated in Figure 3.9.

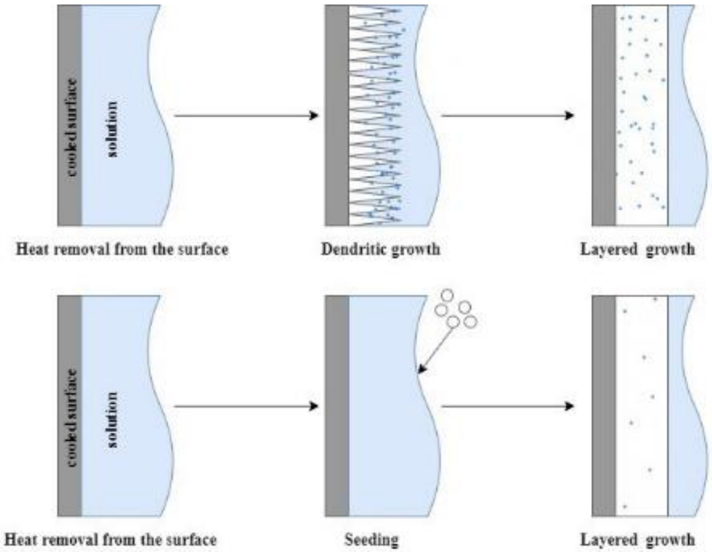

Figure 3.9: Growth of ice on a surface for a seeded and un-seeded experiment adapted from Shirai et al. (1999)

Shirai et al. (1999) investigated the effects of seeding on ice grown from an 1820 ppm polypeptone solution and observed the purity of the product. Upon testing, it was found that the ice that had grown from seeds was purer than the ice that grew without seeds, as shown in Table 3.6. This was testament to the effect of the different types of growth experienced in the two cases.

Table 3.6: Impurities in product ice taken from Shirai et al. (1999) done in a tube ice maker for a glucose-water system

	Polypeptone in the product ice (ppm)
No seeding	570
Seeding	40

3.3.3 Surface adsorption of impurities

Crystal lattices reject impurities because of the molecules of impurities having different shapes and sizes from those of the crystals (Mullin, 2001b). Although rejected from the crystal lattice, impurities can be on the surface of the solids as they tend to adsorb on the surface as it grows

(Myerson, 2002). These surface impurities, if loosely adsorbed, can be washed off to improve the purity of the product.

Post-crystallization washing has been done to improve product purity by pouring a liquid over the product during filtration. Van der Ham, Seckler and Witkamp (2004) showed that applying different wash cycles (odd and even cycles) to the same ice product from the continuous crystallization of a $CuSO_4$ solution, reduced copper content in the ice. This is shown in Figure 3.10.

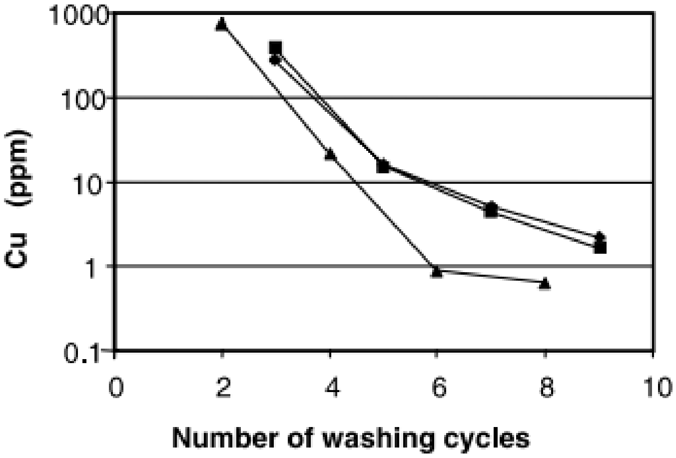

Figure 3.10: Cu content in ice vs washing cycles in three experiments taken from Van der Ham, Seckler and Witkamp (2004)

3.3.4 Mother liquor inclusion and encapsulation of impurities

In EFC where ice and salt(s) crystallize simultaneously, salt crystals can also be in the spaces between ice or other salt crystals that are aggregating. Aggregates form agglomerates, and in the cementation of aggregates, crystals of impurities can be encapsulated in the agglomerates of the products.

Another phenomenon that occurs where there is rough growth is mother liquor inclusion. At high supersaturations, the resulting rough growth leads to macro-steps which encapsulate the mother liquor (Lewis et al., 2015). Mother liquor inclusions reduce the purity of products because as the crystal grows, it rejects impurities, and this leaves the mother liquor right next to a growing crystal with a slightly higher concentration of impurities (Mullin, 2001b).

The inclusion of mother liquor and encapsulated salt crystals reduces the purity of the products. In such cases, washing is ineffective in improving the degree of purity. A warm washing medium can be used to dissolve the solid partially to allow encapsulated crystals to escape (Reddy et al., 2009). For crystals that have mother liquor inclusions, a warm washing medium can be used too, but this would only remove mother liquor inclusions close to the surface if the loss of product is to be avoided.

For crystal aggregation, agitators can be used to break the aggregates apart to allow crystals to escape. Reddy et al. (2009) found washing to be ineffective in improving the purity of the ice crystallized from a Na_2SO_4 solution in the absence of agitation. Adding an agitator however, improved the purity of the products by breaking up the aggregates of ice and allowing entrapped salt to escape.

In EFC, this principle need for agitation has been employed in the crystallizer designs. Crystallizers that are crystallizer-settlers have rake-like scrapers added to the agitation shaft at their top and bottom sections to break up aggregates before the crystals leave the crystallizer.

This chapter was aimed at understanding the factors which affect the production and purity of ice and salt in EFC. Understanding these is important because it allows for the identification of gaps in the literature. It is these gaps in the body of knowledge of EFC that this study will fill. Understanding the factors which affect production and purity of ice and salt is also important in formulating hypotheses to test the factors that have not yet been studied. These gaps and hypotheses are identified and discussed in Chapter 4.

4 RESEARCH MOTIVATION

4.1 Gap analysis

When EFC is used to treat a brine, the production rate and purities of ice and salt should be high. In practice however, this does not happen; the production rates and purity of ice and salt is low. Due to this outcome, production becomes inconsistent because downtime is required to remedy both the low production rate and lack of purity. The low production rate and purity of ice and salt reflect phenomena that arise when certain operating conditions are used for the crystallizer. Understanding the relationship between the operating conditions and the quantity and quality of the products could lead to better choice of operating conditions, so that high production rates and purities are achieved, and the longevity of production is increased. Two such operating conditions are the heat transfer driving force, ΔT_{LMTD}, and initial ice seed loading, SL. These were the focus of this research.

The production rate of ice and salt depends on the heat transfer rate from the bulk fluid to the coolant (Vaessen et al., 2003). The heat transfer rate is a function of the heat transfer area, A, the heat transfer coefficient, U, and the heat transfer driving force, ΔT_{LMTD}. Studies on factors that affect U and its effect on the production rates of ice and salt (Vaessen, Seckler & Witkamp, 2004), as well as studies on altering the design of the crystallizer to increase the heat transfer area have been conducted. Studies on the effect of ΔT_{LMTD} on production rate have also been conducted (Genceli et al., 2005; Vaessen, Seckler & Witkamp, 2004), however, these studies have been for very concentrated brines. Studies on the effect of ΔT_{LMTD} on production rate of ice and salt from dilute brines are lacking in the literature. This research was designed to fill this gap by investigating the effect of ΔT_{LMTD} on ice and salt produced from a dilute brine.

While in suspension, ice and salt make up the solid content in the crystallizer. This is referred to as the magma density, M_T. Magma densities have been found to range from 6 wt.% to 42wt.% (Rodriguez-Pascual et al., 2010; Vaessen, Seckler & Witkamp, 2004). Randall (2010) and Rodriguez-Pascual et al. (2010) found there were limits as to how large the magma density could be before the separation of ice and salt became poor. Poor separation was reflected in the product purity. Though cases of these limits are present in literature, no relationship has been drawn between the changes in magma density (due to change in ΔT_{LMTD}), separation and purity. The effect of ΔT_{LMTD} on purity was studied to understand this link. Poor separation is reflected in poor product purity

The magma density is not the only factor that affects separation. Another factor is crystal size. The ice and salt produced must be large enough to float and sink, respectively. The size of the crystals is a function of growth and nucleation. It is known that the growth of seeds leads to large product crystals while nucleation of crystals from solution leads to fine product crystals (Doki et al., 1999). When supersaturation is provided it must be consumed. The surface area provided (by seeds) to consume that superstation determines whether nucleation, growth, or both, occur (Doki et al., 2002; Doki et al., 1999; Lung-Somarribaa et al., 2004). When little surface area is provided, the supersaturation is consumed by nucleation of crystals from solution. The resulting crystals produced are fine. If enough or more than enough surface area is provided, growth will occur, resulting in large product crystals. The larger the crystals, the better the separation. The effect of surface area on nucleation and growth of salts is documented in literature (Doki et al., 2002; Doki et al., 1999; Lung-Somarribaa et al., 2004), however, the effect of surface area on nucleation and growth of ice and how that is reflected in purity has not been studied. This work filled this gap by investigating the effect of ice seed loading on purity. By varying the seed loading, the system is provided with different surface areas.

The seeds are not the only source of surface area in the crystallizer. The cooled wall also provides surface area for crystallization. Crystallization on the wall results in a scale layer which limits the efficiency of heat removal from the bulk. This layer results in low production of ice and salt. The scale layer can become too thick for the scrapers to etch under, (Vaessen, Seckler & Witkamp, 2004) which increases the downtime required for removal of the scale layer. This interruption results in inconsistent production.

The initial magma density could be used to control where nucleation occurs (the wall or bulk), such that the longevity of production is improved. Providing the system with enough surface area in the bulk via the addition of ice seeds may lead to more crystallization in the bulk than on the wall. The concept of the consumption of supersaturation in the bulk versus the wall was developed based on observation (Leyland, Chivavava & Lewis, 2019), but the relationship was not quantified. This work investigated this concept by quantifying how the ice and salt is distributed between the wall and in the bulk at different ice seed loadings.

EFC operation is mainly carried out in continuous mode. In a continuous set up, after start-up and nucleation, there is a transient phase before the system reaches steady state. It is this steady state production rate and purity which have been found to be low due to different operating conditions. The steady state production rate and purity are therefore determined by whatever takes place during the transient phase. Understanding the effect of operating conditions on production rate and purity during this transient phase will allow for a better choice of operating conditions, and for better production once steady state is reached. Batch crystallization is always in the transient phase until complete separation is achieved. For this reason, all the investigations mentioned above were carried out under batch mode, as it is consistently in transient phase.

4.2 Hypotheses

4.2.1 Effect of ΔT_{LMTD} on ice and salt yield

Increasing ΔT_{LMTD} will increase the total yield of ice and salt because it permits an increased heat transfer rate. An increase in the heat transfer rate results in increased crystallization rate, thereby yielding a higher mass of ice and salt from solution. The total ice yield will be the sum of the ice formed on the wall and the ice formed in the bulk. **It is hypothesised that as the ΔT_{LMTD} increases, the yield of ice on the wall will increase, while the yield of ice in the bulk decreases.** This prediction is based on the fact that an increase in ΔT_{LMTD} results in increased supersaturation at the cooled wall. The supersaturation at the wall leads to the formation of a scale layer. Continuous cooling will result in growth of the scale layer. As ΔT_{LMTD} increases, the scale layer will be growing at a faster rate, so the yield of ice on the wall will increase. A scale layer reduces the overall heat transfer coefficient between the bulk and the coolant. This will lead to a reduction in the ice that can be formed in the bulk.

4.2.2 Effect of ice seed loading on bulk and wall crystallization of ice

It is hypothesised that increasing the ice-seed loading results in an increase in bulk crystallization and a decrease in the wall crystallization of ice. This is because an increase in the ice-seed loading increases the surface area available for growth in the bulk solution. Increased crystallization in the bulk reduces supersaturation available for nucleation on the wall, leading to a reduction in the yield of ice on the wall.

Beyond a certain seed loading, the yield of ice and salt in the bulk will decrease while the yield of ice on the wall will increase. This is because a high seed loading increases the initial magma density of the system. Increased magma density affects the efficiency of mixing since the removal of supersaturated liquid from the wall into the bulk is reduced when the magma density is high. This promotes localised supersaturation at the wall which leads to scale layer formation. Increasing the seed loading also increases crystal-wall collision, promoting increased adhesion of crystals to the wall. Adhesion also results in the formation of a scale layer which reduces heat transfer. The reduced heat transfer rate results in less ice in the bulk

4.3 Key Questions

The key questions that can be posed are:

i. What is the relationship between heat transfer driving force, ΔT_{LMTD}, and yield of ice and salt in the bulk?

ii. How is the purity of ice affected by the yields produced at different ΔT_{LMTD} values?

iii. What is the relationship between ice seed loading and bulk and wall crystallization of ice?

iv. How is the purity of ice affected by the yields of ice on the wall and in the bulk produced at different seed loadings?

5 MATERIALS AND METHODS

The materials and methods used to test the hypotheses in section 4.2. are detailed in this chapter. The experimental design is explained first, followed by the details about the equipment that was used for the experiments. The experimental procedure concludes the chapter.

5.1 Experimental design

The experiments were carried out in three stages. The first was to use thermodynamic modelling to determine the operating temperature ranges for the experiments. The second was to prepare the seeds. The third stage was to run the experiments in batch operation.

5.1.1 Dilute Brine

A 4 wt.% Na_2SO_4 aqueous solution was used for all the experiments as Na_2SO_4 is a common salt in South African brines(Mehlo, 2019). Studying this brine would allow the results to apply directly to the real brines. The concentration was chosen because this is the eutectic concentration of an aqueous Na_2SO_4 solution. Using a eutectic concentration is relevant for understanding a eutectic system. It allows eutectic freeze crystallization to occur without having to crystallize ice or salt out first before reaching eutectic conditions.

5.1.2 Thermodynamic modelling

Thermodynamic simulation of the EFC of 1 kg of 4 wt.% Na_2SO_4 aqueous solution was conducted using OLI Stream Analyser ^{TM} 10.0 to determine the temperature to be used in the experiments (OLI-Systems-Inc, 2020). OLI uses Mixed Solvent Electrolyte (MSE) thermodynamic frameworks and databases to calculate different phenomena at given conditions. OLI Stream Analyser ^{TM} was used to predict the phases that would crystallize out of solution for a range of temperatures to find the eutectic temperature of the solution. Obtaining the eutectic temperature of the solution prior to experiments was important in choosing the operating conditions for the experiments. The experiments were conducted at a temperature below the eutectic temperature so that eutectic freeze crystallization occurred.

5.1.3 Ice seed preparation

The method of ice seed preparation had to ensure that the nature of the seeds (the size and shape) was kept constant so that any changes observed in the production rate and purity of the products were only due to the change in the seed loading, rather than due to changes in size and shape.

5.1.4 Batch crystallization

Batch crystallization was chosen in order to understand the effect of the operating conditions in a simple set up that would allow for easy handling of ice seeds. The batch crystallization was done in two phases. In the first, ΔT_{LMTD} was varied (2, 4, 6, 8 and 10 °C) to investigate the effect of ΔT_{LMTD} on the yield of ice in the bulk and ice on the wall, the yield of salt and the purity of ice. The range of ΔT_{LMTD} was based on the preliminary experiments that showed that it was not worthwhile to carry out experiments at ΔT_{LMTD} above 10 °C as the extent of scaling was so severe there was very little operability. A constant seed loading of 6 wt.% (w_s/w_l) was used as suggested by Kaboyashi and Shirai (1996) for the production of large ice crystals. This was important because large ice crystals would allow better gravitational separation.

The second phase was to investigate three things: the effect of ice seed loading on the yield of ice in the bulk and on the wall, the yield of salt, and the purity of ice, using ice seed loadings of 0 to 12 wt.% :- 0, 3, 6, 9 and 12 wt.%. This range was chosen as the calculated seed loading ratio was found to be 0.58 which translated to critical seed loadings ranging from 708 g to 799 g. If these were used, the seed would take up between 49 and 55 % of the crystallizer volume. This would have been impractical to implement, hence the chosen range of 0-12 wt.%. A ΔT_{LMTD} of 4 °C was used and kept constant. This temperature was chosen as it produced the least scale layer when the ΔT_{LMTD} experiments were carried out. This was important as the results would show if it were possible to use seeds to improve the performance of the ΔT_{LMTD} that, to date, had produced the least scale.

5.2 Equipment and measurement

5.2.1 Synthetic brine

The brine used in the experiments was prepared by dissolving reagent grade $Na_2SO_4 \cdot 10H_2O$ in deionised water at a ratio of 90.9 g of salt for every 909.9 g of water to yield a 4 wt.% Na_2SO_4 brine.

5.2.2 Ice seed preparation

An ice-shaving machine used to prepare seeds from ice cubes made from distilled water. It consisted of an ice depositing chamber with blades that shave the ice into fine crystals.

5.2.3 Batch crystallization

Figure 5.1 shows a schematic diagram of the equipment that was used for the batch crystallization experiments.

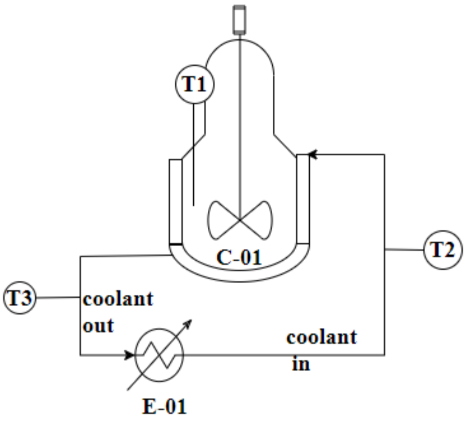

Figure 5.1: Schematic of the batch crystallizer set up.

A 1.45 L glass-jacketed, stirred crystallizer, C-01, was used with a Lauda Proline cooling unit(Delavan, USA), E-01, to cool the solution. Polydimethylphenylsiloxane (commercially known as Kryo-51) was used as the coolant. Three platinum resistance temperature probes connected to a Tempcontrol F252 AC bridge and a 16-channel SB500 switchbox (Nootdorp, Netherlands) were used to measure the temperatures of the solution (T1) and the coolant (T2 and T3). The temperatures were recorded by Ulog temperature logging software. All experiments were carried out at room temperature, so the vessel and piping were insulated. Preliminary experiments showed that a pitched blade impeller with a diameter of 0.075m ensured efficient suspension of the seeds. This impeller was at a size of $\frac{D_{crystallizer}}{1.47}$. The impeller was positioned a third of the total crystallizer length above the base of the crystallizer to avoid dead zones. The impeller used an IKA RW20(Staufen, Germany) motor for rotation.

5.3 Experimental procedure

5.3.1 Seed preparation

The seeds were prepared by freezing distilled water in ice cube trays overnight in a freezer at -18 ℃. The ice cubes were emptied into the shaving chamber of the ice-shaving machine. Once switched on, the ice cubes were shaved into fine ice crystals, and these were collected in a cold insulated beaker before being weighed for use in the batch crystallization experiments. The beaker was kept cold in a cold room at 2.5 ℃ overnight. After the first three repeats that were testing for reproducibility, this procedure was carried out prior to the batch crystallization without the size and purity analysis.

The seed preparation prior to running the batch experiments was repeated in order to determine if the seed size distribution would be reproducible. The modal size of the seeds was between 260 and 520 μm. This was typically larger than the ice crystals obtained in EFC (up to 250 μm (Genceli, 2008), (Rodriguez-Pascual et al., 2010)). The seed size distribution was reproducible (Appendix 10.7).

The seeds prepared from the ice-shaving machine were slightly larger than those produced by crystallization from solution. The seeds were just as reproducible however, and the reliability of this method made it a better option for seed preparation and avoided the loss of time due to unsuccessful runs as happens with the crystallization from solution.

5.3.2 Batch crystallization

First, the crystallizer was filled with the solution. Thereafter, the temperature logger software was opened and set up prior to starting the cooling unit. The cooling unit was started to allow the coolant to flow and set to the required temperatures shown in Table 5.1.

Table 5.1: Cooling unit set points for different ΔT_{LMTD}.

ΔT_{LMTD} (°C)	Thermostatic Unit Set point (°C)
2	-3.39
4	-7.30
6	-11.43
8	-15.43
10	-17.30

Once the temperature logger was started, the agitator was set in motion at 230 rpm. A rotational speed of 230 rpm was chosen as this was experimentally determined to be the speed where no scaling at ΔT_{LMTD} of 2 °C would happen. It was important for there to be no scaling as this would be the control experiment for the ΔT_{LMTD} experiments When T1 = -1.15 °C, 1g of reagent grade $Na_2SO_4 \cdot 10H_2O$ was added(Aspeling, 2019). This salt seed loading was sufficient to initiate salt crystallization such that the experiments could be carried out under eutectic conditions. When the bulk temperature reached -1.3 °C, 6 wt.% (w_s/w_l) ice seeds were added for the first phase, while for phase 2, the test level seed loading was added to the solution. The different seed loadings required are shown in Table 5.2

Table 5.2: Seed masses for the different seed loadings

SL (wt.%)	Seed mass (g)
0.1	1.44
3	43.50
6	84.41
9	122.88
12	159.34

The seeds were prepared using the procedure described in section 5.3.1 and they were harvested just in time for seeding in the batch crystallization experiments. Crystallization continued for 1 hour 15 minutes after seeding. Thereafter the coolant flow was stopped by switching the cooling unit off. This was followed by stopping the agitator. The crystallizer did not have separation height so the harvested slurry would be a mixture of ice and salt. Transferring the slurry from the crystallizer to the beaker further mixed the ice and salt. Preliminary experiments showed that this could not be avoided, but the use of an Imhoff cone after harvesting in the beaker allowed for separation of ice and salt therefore the suspension was transferred into a cooled 2 L beaker then to a cooled Imhoff cone. The Imhoff cone and beaker were kept overnight in a cooled room at 2.5 °C, then in a freezer at -18 °C for 7 minutes before harvesting. This was done to minimise melting. The suspension was then stirred for 10 minutes using a spatula to allow for the disengagement of salt from ice in a cooled room at 2.5 °C. Ice was harvested on to a Buchner funnel with filter KimLab (Xi'an, China) qualitative paper of 11 µm pore size connected to a vacuum pump for filtration. A ratio of 0.5:1 of wash water:ice product was used during the experiments. A membrane filter with KimLab (Xi'an, China) cellulose acetate filter paper of 0.22 µm pore size was used on the remaining suspension to collect the salt. The filtered ice and salt were weighed, and the masses were recorded.

A sample of the ice product was taken from several positions in the beaker was taken as for imaging using a light microscope; the sample was 10 wt. % of the product. Images were captured using a light microscope and they were acquired using the analySIS docu ™ software and saved for sizing and shape analysis that was to be done at a later stage (section 5.3.3). The collected ice was stored in a sample bottle and allowed to melt for sulphate analysis for the determination of the ice purity.

The scale layer was melted off the wall of the crystallizer by raising the cooling unit set point to 20 °C. Thereafter it was collected as a liquid in a measuring cylinder and weighed. The mass and volume of the scale was recorded. A sample was stored in a sample bottle and allowed to melt for sulphate analysis to determine the scale purity.

5.3.3 Image analysis

A sample of ice seeds as well as product ice and salt from the batch crystallization were collected and set under an Olympus BX51 microscope(Johannesburg, South Africa) for imaging. The slides used under the microscope were insulated and frozen prior to use to stop the ice from melting. The size and shape characterisation was carried out using the captured images and ImageJ image analysis software (Schneider, Rasband & Eliceiri, 2012). ImageJ (Schneider, Rasband & Eliceiri, 2012) was used to obtain the area of each crystal, and this area was converted from pixels to microns using a measurement of the scale bar from the images. The area was then converted to an equivalent diameter using the formula for the area of a circle as the crystals were disc shaped. At least 100 crystals were analysed for ice as the imaging was limited by melting of the sample, and 300 crystals for salt.

6 RESULTS AND DISCUSSION

The findings from the experiments are discussed in this chapter. The results from carrying out the thermodynamic modelling is shown first. This is followed by the description of a typical experimental run. Discussion of the effect of ΔT_{LMTD} on the yield of ice and salt as well as the purity of the ice produced in batch crystallizer follows, and the effect of ice seed loading concludes the chapter.

6.1 Thermodynamic modelling

OLI Stream Analyser ™ V10.0(OLI-Systems-Inc, 2020) predicted that salt would crystallize out of solution from -1.03 °C, and ice would then crystallize out of solution at -1.15 °C. This is shown in Figure 6.1. This prediction meant the experiments had to be conducted at temperatures below -1.15 °C. The predicted ratio of ice to salt is 10:1. It was expected that this ratio would be different as the feed would not be completely separated into two solids during the experiment. Due to the crystallizing salt being a hydrous salt, this means ice yield, even in the case of complete perfect separation could never be 100%, as seen here the maximum achievable yield is 95%.

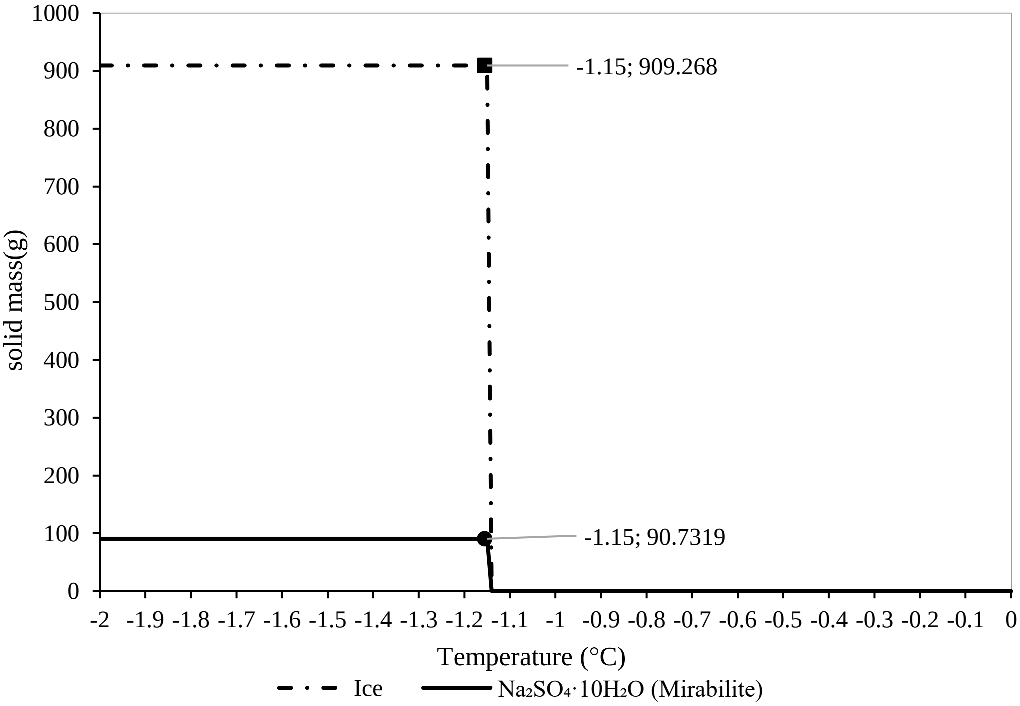

Figure 6.1: Yield of solids vs temperature for a 4 wt.% solution

6.2 Typical experimental run

Figure 6.2 shows a typical temperature profile for an experimental run. Figure 6.3 shows a zoomed in version of the temperature profile just after seeding. The profile for one of the experiments for a ΔT_{LMTD} of 6 °C was used as an example. The temperature profiles were reliably reproducible with the variation at ±0.02 °C. The experiment was started at 0 minutes.

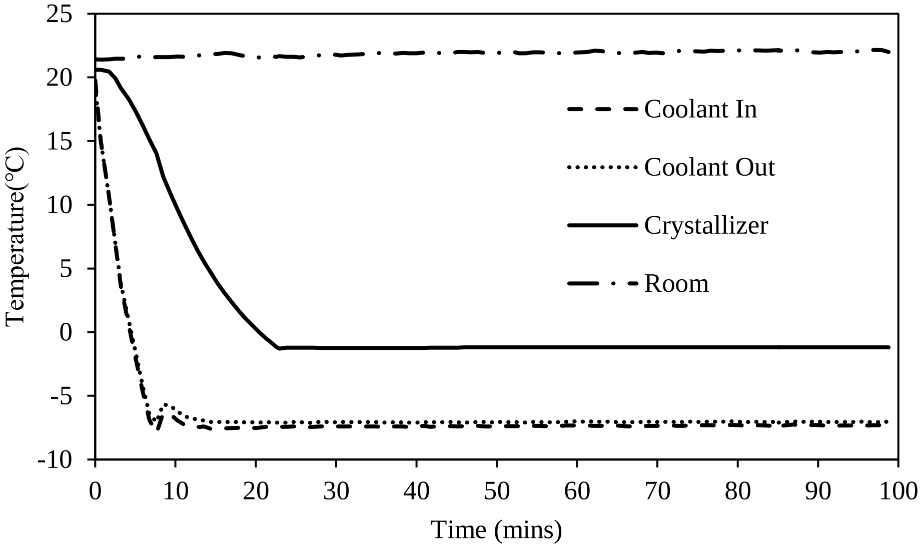

Figure 6.2: Temperature profiles for ΔT_{LMTD} = 6 °C

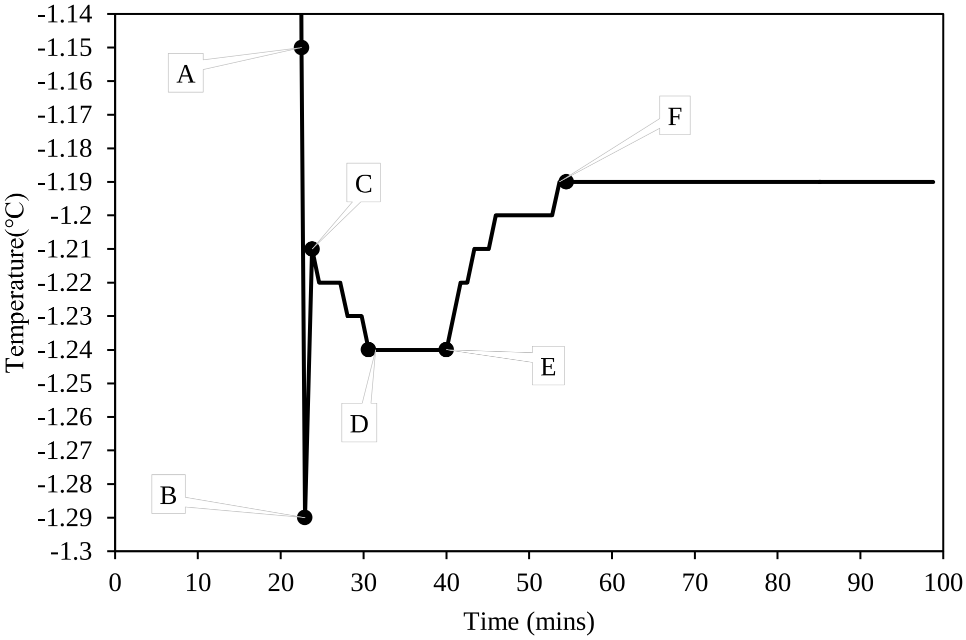

Figure 6.3: Temperature profile for the contents of the crystallizer after seeding ΔT_{LMTD} = 6 °C
A-salt seeding temperature; B-ice seeding temperature; C bulk temperature after seeding; D bulk temperature after cooling; E final cool bulk temperature; F Final operating temperature

After cooling the solution from room temperature, reagent grade $Na_2SO_4 \cdot 10H_2O$ salt seeds were added to the bulk at point A when the crystallizer temperature was -1.15 °C. At this point, no temperature change was observed to indicate salt nucleation as the temperature continued to decrease. When the bulk crystallizer temperature reached -1.29 °C at point B, ice seeds were added. An increase in the bulk crystallizer temperature from -1.29 ℃ to -1.21 ℃ (point C) was observed. This temperature increase was due to the heat of crystallization released when nucleation of ice from solution occurred upon seeding. After seeding with ice, the crystallizer temperature decreased from point C to -1.24 ℃ at point D. This decrease was due to the heat removal rate being faster than the release of heat of crystallization due to crystal growth and nucleation. This resulted in removal of the heat of crystallization and the cooling of the solution, which led to the observed temperature decrease.

Between point D and E, the temperature remained constant as the heat released as the crystals continued to grow was balanced by the heat removal rate. After point E, the bulk crystallizer temperature gradually increased to -1.19 ℃ at point F. The increase in the bulk crystallizer temperature observed after point E was due to the formation of an ice layer on the cooled wall of the crystallizer. The presence of the ice scale layer introduced additional heat transfer resistance to the system. This resistance reduced the total heat transfer coefficient, U, thereby reducing the heat removal rate. A reduction in the heat removal rate results in inefficient removal of the heat of crystallization being released into the bulk which raised the temperature in the bulk crystallizer. A similar profile was observed in work done on EFC from a eutectic Na_2SO_4 solution by Jooste (2016), however, this was done in continuous mode without seeding. Operating in continuous mode resulted in a longer time before the onset of scale formation, while the lack of seeds resulted in a larger initial supersaturation (in comparison to the initial supersaturation for this work) as the solution had to cool to beyond the metastable zone width.

6.3 Effect of ΔT_{LMTD}

6.3.1 Effect of ΔT_{LMTD} on ice and salt yield

6.3.1.1 Overall Mass balance

Error! Reference source not found. shows the feed line and the average mass balance at d ifferent ΔT_{LMTD}. The bars for the mass balance for each ΔT_{LMTD} are very close to the feed line showing that there was very little loss of material during the experiments. The mass balances ranged from 11.06 g to 24.43 g. As the ΔT_{LMTD} increased, a larger portion of the brine was crystallized out as ice and salt.

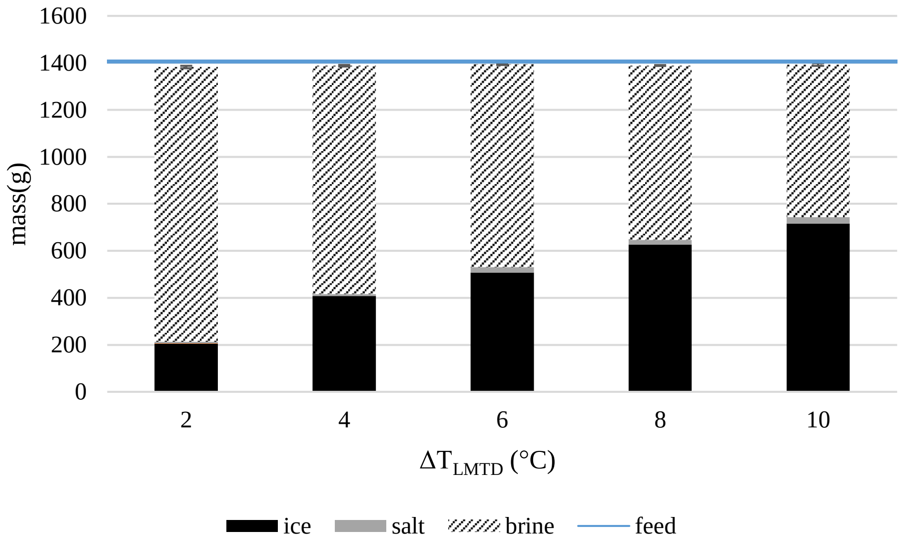

Figure 6.4: Average mass balance at different ΔT_{LMTD}

Most of the brine was converted to ice, as was expected as the brine was very dilute (4 wt.% Na_2SO_4). This means there was a larger portion of water as a crystallizing resource to begin with, so naturally more ice would be formed than salt. The ratio predicted by the thermodynamic simulation for ice yield to salt yield was 10:1. The obtained ratios are all over 20 which is more than twice the predicted ratio. These are shown in .

Table 6.1. These are ratios of total ice to harvested salt. Entrained, entrapped, and washed salt are not included, which may explain the large difference between the predicted and obtained ratio of ice to salt. This salt was not included as it was not harvestable.

Table 6.1: Experimental ratio of ice yield to salt yield

ΔT_{LMTD} (°C)	**ice:salt**
2	26
4	44
6	22
8	30
10	26

6.3.1.2 *Effect of ΔT_{LMTD} on total yield of ice and salt*

The ice and salt yields are shown in Figure 6.5. The error bars are very small ($\pm 0.9\% < \varepsilon_{ice} < \pm 3.6\%$; $\pm 1.3\% < \varepsilon_{salt} < \pm 5.4\%$) showing that these yields are reproducible at the specific ΔT_{LMTD}s.

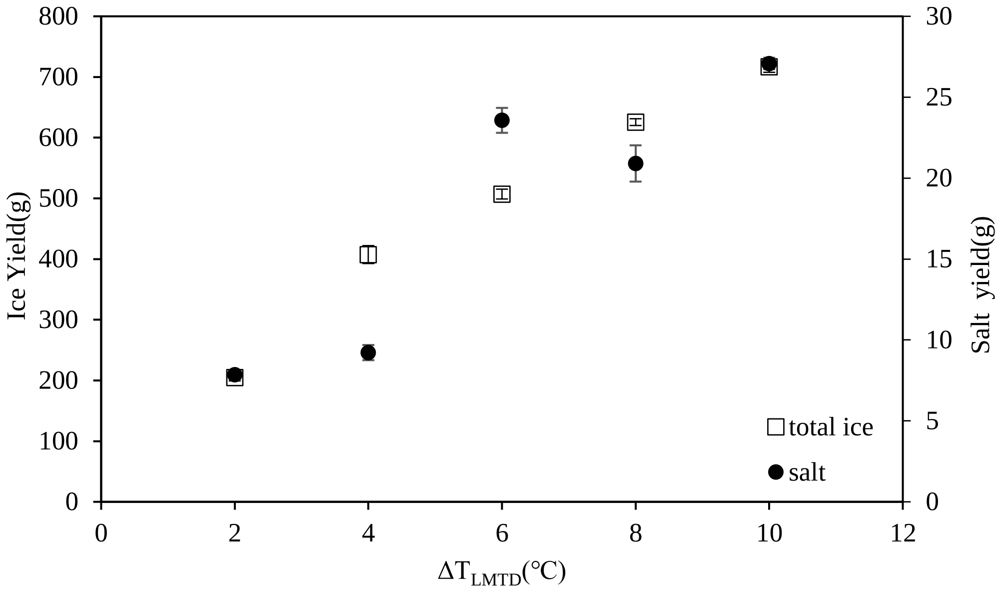

Figure 6.5: Effect of ΔT_{LMTD} on ice and salt yield

Figure 6.5 shows that the total yield of ice and salt increased as ΔT_{LMTD} increased. The increase in the ice and salt yield with ΔT_{LMTD} can be attributed to the increase in ΔT_{LMTD} resulting in an increase in the heat transfer rate. Figure 6.6 shows the values of Q_{cool} at each ΔT_{LMTD}. These values were calculated using the measured coolant flow rate, temperatures, and equation *2.10* (appendix 10.4). These Q_{cool} values show the heat transferred from the bulk to the coolant. The heat ingress into the system was not measured or included in this calculation.

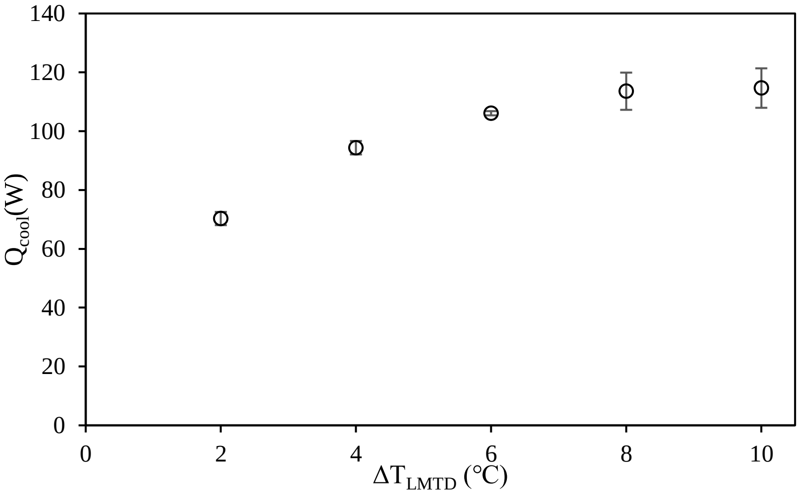

Figure 6.6: Heat transfer rates at varying ΔT_{LMTD}

Figure 6.6 shows that as ΔT_{LMTD} increased, Q_{cool} increased. The heat transfer rate determines how much ice and salt can be crystallized from solution as it allows for the removal of heat of crystallization from the bulk. When there is an increase in ΔT_{LMTD}, the resulting increase in heat transfer rate is balanced by an increase in crystallization of ice and salt from solution, hence the observed increase in the yield of ice and salt when ΔT_{LMTD} was increased. Vaessen, Seckler and Witkamp (2004) and Genceli et al. (2005) also found an increase in the heat transfer rate and, in turn, an increase in the production of ice, as ΔT_{LMTD} increased.

6.3.1.3 Bulk and wall crystallization

Even though Vaessen, Seckler and Witkamp (2004) found an increase in the heat transfer rate as ΔT_{LMTD} increased, they also found that the increase in ΔT_{LMTD} resulted in more solid content in the crystallizer which caused the formation of an ice scale layer. In this work, a scale layer also formed when ΔT_{LMTD}s above 4 °C were applied. This is shown in Figure 6.7. For ΔT_{LMTD} of 4 °C and above, the total ice yield was a sum of ice formed in the bulk and ice formed on the wall (scale) with most of the total ice yield being scale. It was assumed that the seeds remained in the bulk, so the yield of ice in the bulk reported here excludes the seed mass.

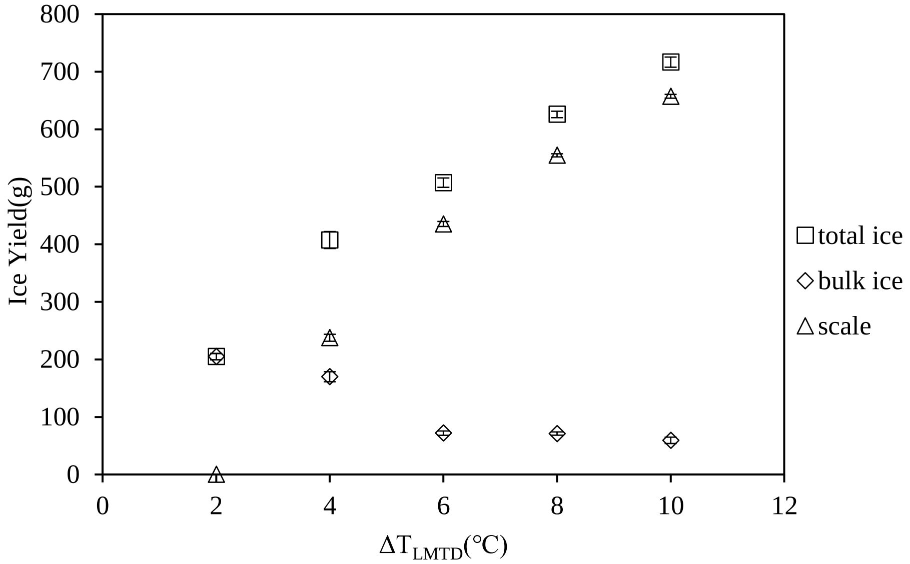

Figure 6.7: Effect of ΔT_{LMTD} on ice yield

Figure 6.7 shows that as ΔT_{LMTD} increased, the yield of ice in the bulk decreased. From **Error! Reference source not found.**, it can be seen that the yield of salt (also in the bulk) increased as ΔT_{LMTD} increased. In EFC, ice and salt simultaneously crystallize out of solution. After ice crystallizes out of solution, the resulting change in concentration creates supersaturation for salt to crystallize out of solution. This will occur regardless of whether the ice crystallizes on the wall or in the bulk, which explains the increase in the yield of salt in the bulk, though the ice in the bulk decreased.

Figure 6.7 also shows that as ΔT_{LMTD} increased, the yield of the scale layer increased. As the ΔT_{LMTD} increased, the cooled wall became colder, therefore the fluid right next to the wall, the boundary layer, would have the highest supersaturation. If the boundary layer is undisturbed, the localised high supersaturation at the wall leads to the formation of a scale layer by heterogeneous nucleation (Leyland, Chivavava & Lewis, 2019). This was the phenomenon responsible for scale formation in the case of Vaessen, Seckler and Witkamp (2004). They found that the increase in solid content, caused by the increase in ΔT_{LMTD}, altered the hydrodynamics of the system by reducing the disturbance of the boundary layer. The scrapers installed for the very purpose of disturbing the boundary layer did not do so efficiently, so a scale layer formed. For this investigation, the cooled wall was not scraped, and the solid content changed from 0 to 6 wt.% right from the beginning of the experiment. This immediately altered the hydrodynamics of the system and allowed scale formation by heterogeneous nucleation. Operating at increasing ΔT_{LMTD} meant the walls were at colder temperatures. Ice adheres more strongly to colder walls (Petrenko, 1993) so the scale layer could have also formed by adhesion of crystals (those made from solution and seeds) (Motsepe, 2020). This work was limited in that the scale formation mechanism was indistinguishable. The scale could have formed by nucleation, adhesion, or both.

Leyland, Chivavava and Lewis (2019) found that the time it took for the scale to form became shorter as the ΔT_{LMTD} increased. They derived this time from scraper stoppages and the temperature profiles for each experiment. For this work, this time for the scale to form was derived by periodically stopping the experiment and repeating until the first observance of a scale layer. This was done in supplementary experiments as the variation in the scale formation time (SFT) as derived from the temperature profiles was very small. The SFT is defined as the time taken for the scale layer to form after seeding. The supplementary experiments were carried out for ΔT_{LMTD} of 4 and 10 °C. These are shown in Table 6.2. It is possible that these times include some growth time as there is some ice at these SFT, but these could not be set apart. Additional adhesion of ice to the wall after stopping the experiment was minimised by harvesting as quickly as possible.

Table 6.2: Scale formation times

ΔT_{LMTD} (°C)	**Scale Formation Time (minutes)**	**Scale yield t=SFT (g)**	**Scale yield t=75 min (g)**
4	12	28.8	238
10	2	85.9	657

Table 6.2 shows that as ΔT$_{LMTD}$ increased, the SFT became shorter. The combination of a shorter scale formation time and a higher driving force provided by the higher ΔT$_{LMTD}$ resulted in the scale layer growing at a faster rate for longer periods, since it started growing earlier. This shorter SFT resulted in a larger scale yield as ΔT$_{LMTD}$ increased.

After forming, the presence and growth of the scale layer increased the thermal resistance to heat removal from the bulk to the coolant. The increase in thermal resistance between the coolant and the bulk was evident in the difference between the coolant inlet and outlet temperatures, $\boldsymbol{T_{c,out} - T_{c,in}}$. $\boldsymbol{T_{c,out} - T_{c,in}}$ declined as the experiment progressed for all the ΔT$_{LMTD}$ values where a scale layer formed.

Figure 6.8 shows the effect of ΔT$_{LMTD}$ on $T_{c,out} - T_{c,in}$ The temperature profiles were reliably reproducible with the maximum variation at ±0.02 °C.

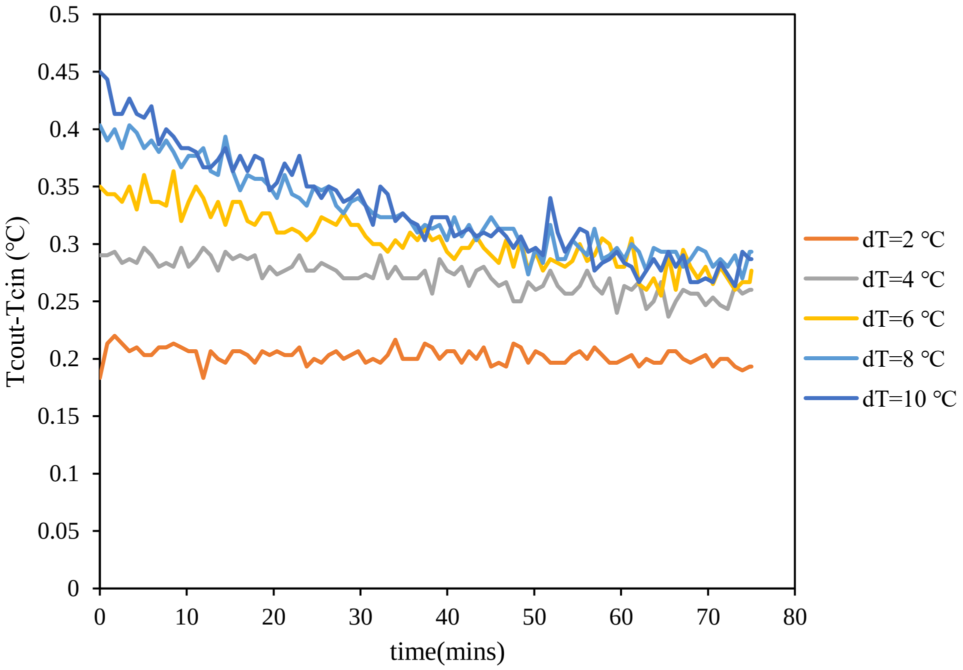

Figure 6.8: Effect of ΔT_{LMTD} on $T_{c,out} - T_{c,in}$

It can be seen that when there was no scale layer, at ΔT$_{LMTD}$=2 °C, $T_{c,out} - T_{c,in}$ was virtually constant. When there was a scale layer at ΔT$_{LMTD}$=4 °C and above, $T_{c,out} - T_{c,in}$ gradually decreased. This shows that the presence of the scale layer reduced cooling of the bulk. The extent of the reduction in cooling became more severe as ΔT$_{LMTD}$ increased because the scale layer became larger. Reduced cooling of the bulk resulted in a reduction in the rate of crystallization of ice from solution, resulting in the observed reduction in the yield of ice in the bulk as ΔT_{LMTD} increased. The reduction, however, was not to the extent that cooling stopped, since $T_{c,out} - T_{c,in}$ never reached 0.

6.3.1.4 *Effects of the scale layer on heat transfer*

The increase in thermal resistance between the coolant and the bulk due to the scale layer can also be seen in the overall heat transfer coefficient, U. As ΔT_{LMTD} increased, U decreased. This is shown in Figure 6.9. The U values were calculated using the measured coolant and bulk temperatures, Q_{cool} values calculated earlier and the heat transfer area (equation *2.6*). These values were calculated for each set of temperature readings which were 51 seconds apart (Appendix 10.5).

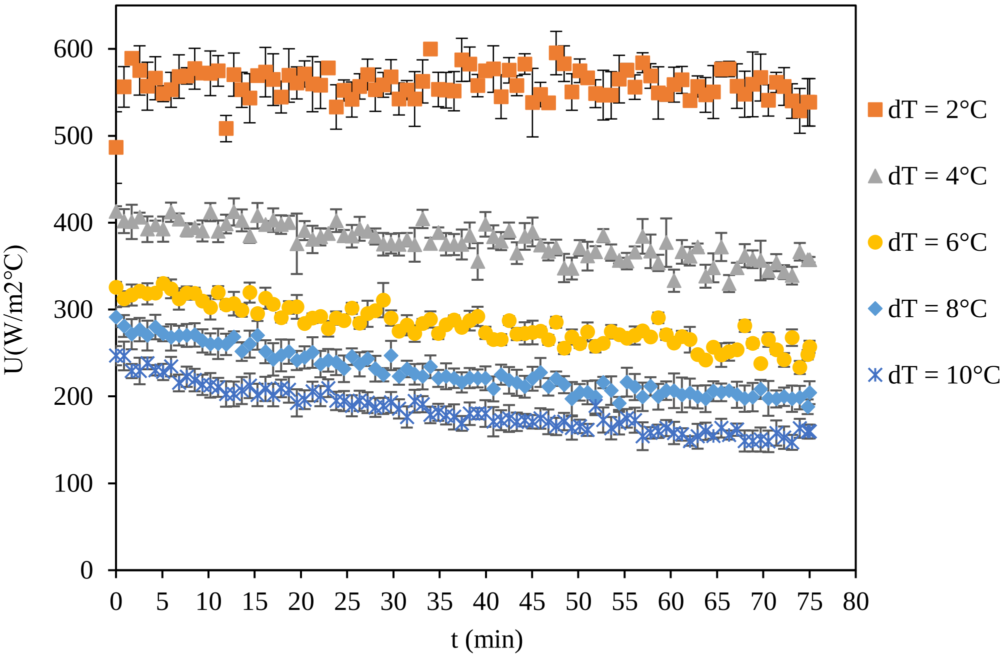

Figure 6.9: Average heat transfer coefficient at varying ΔT_{LMTD}

The reduction in U was due to the presence of the scale layer. The scale layer increased the heat transfer resistance between the bulk and the coolant. This was depicted in equation *3.2*. When there was no scale layer, U was only a function of resistances in the process fluid, the wall, and the coolant. The scale layer introduced an extra term, α_{sccale}. This was calculated (Appendix 10.6) for each ΔT_{LMTD} and the results are shown in Figure 6.10. These values were calculated for the final scale layer, as the growth rate of the scale layer could not be determined for different points in time as done with the U values.

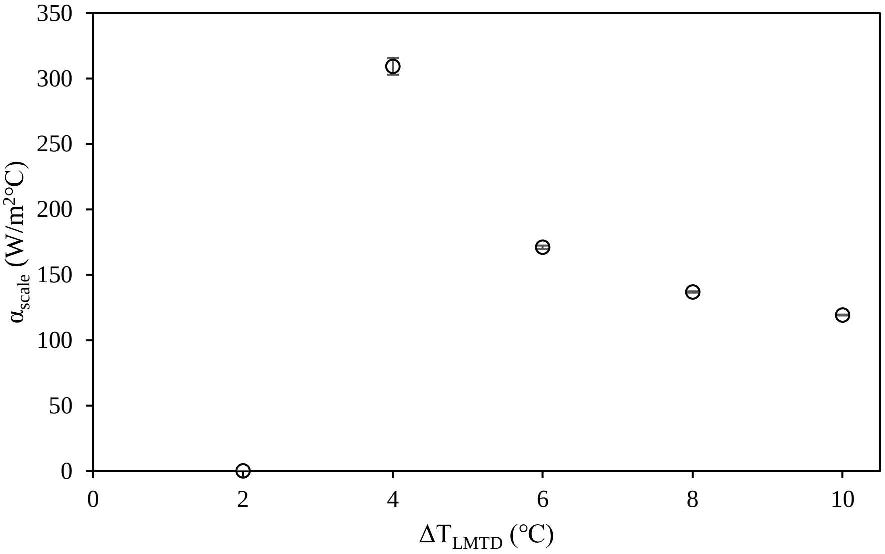

Figure 6.10: Effect of ΔT_{LMTD} on α_{scale}

As ΔT_{LMTD} increased from 2 to 4 °C, a scale layer grew and introduced an extra heat transfer coefficient, α_{scale} of 309.4 W/m^{2}K. Having resistance to heat transfer due to the scale layer lowered the overall heat transfer coefficient though an extra term was introduced. As the ΔT_{LMTD} increased further, the scale layer became larger, thereby reducing α_{scale}. The reduction in α_{scale} resulted in the reduction of the overall heat transfer coefficient, U.

The reduction in the overall heat transfer coefficient with the increase in ΔT_{LMTD} is the reason that the increase in the heat transfer rate plateaus, as was observed in Figure 6.6. A comparison between the heat transfer rate achieved experimentally and the heat transfer rate that would have been achieved had the scale layer not been present (theoretical) can be made. Figure 6.11 shows heat transfer rates at different ΔT_{LMTD}s for the two scenarios. The theoretical values were calculated using the U obtained when ΔT_{LMTD} was 2 °C and there was no scale layer. Figure 6.11 shows that had the scale layer not been there, higher heat transfer rates would have been achieved. The experimental heat transfer rate is 32 % lower than the theoretical at a ΔT_{LMTD} of 4, and this reduction becomes larger as ΔT_{LMTD} increases.

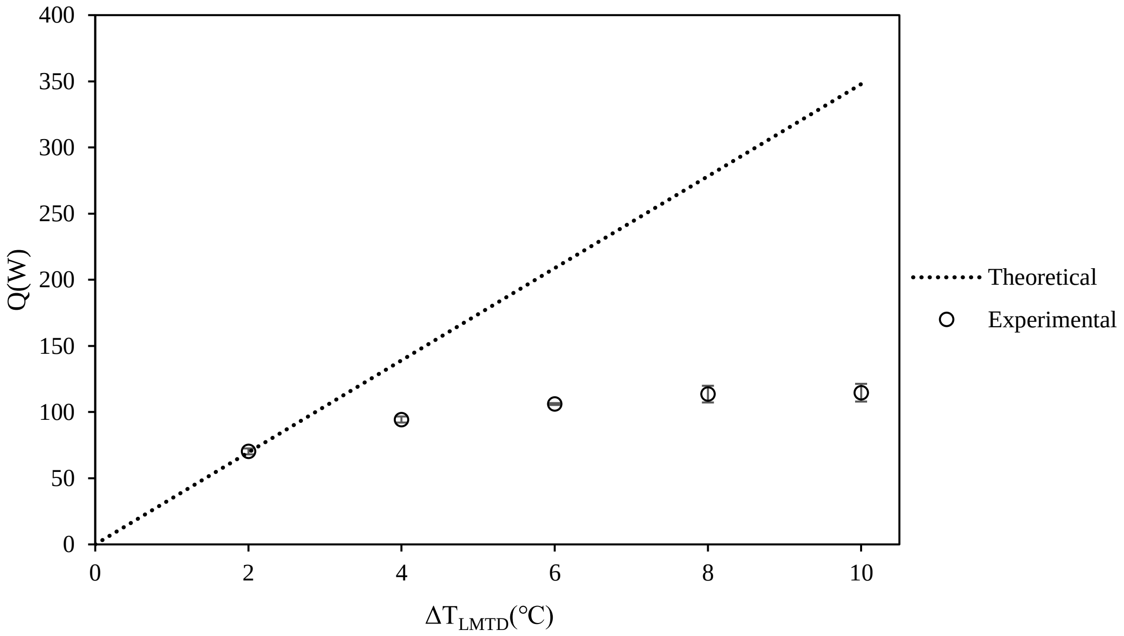

Figure 6.11: Comparison of heat transfer rates.

Had the scale layer not been present at higher ΔT_{LMTD}s, higher heat transfer coefficients would have been achieved and in turn, higher heat transfer rates. This would have allowed more heat to be removed from the bulk, which would have produced higher yields of ice in the bulk.

6.3.1.5 Hypothesis-Effect of ΔT_{LMTD} on ice and salt yield

It was hypothesised that as ΔT_{LMTD} increased, the yield of ice on the wall would increase, while the yield of ice in the bulk would decrease. This was found to be true and was attributed to the colder temperatures that are required to operate at higher ΔT_{LMTD}s resulting in scale layer formation. The high ΔT_{LMTD}s allowed the scale to form much earlier in the experiment and to grow at a faster rate. This change resulted in a larger ice scale layer as the ΔT_{LMTD} increased. The scale layer increased the heat transfer resistance between the coolant and the bulk, and this resistance was increased as the scale layer became larger. The increase in resistance to heat transfer between the coolant and the bulk resulted in reduced ice production in the bulk, causing the reduction of yield of ice formed in the bulk.

6.3.2 Effect of ΔT_{LMTD} on ice purity

6.3.2.1 Purity of ice in the bulk

Figure 6.12 shows the purity of the ice obtained at different ΔT_{LMTD}s. The ice purity decreased with increasing ΔT_{LMTD} from the highest purity of 99.2 %H_2O achieved when the ΔT_{LMTD} was 2 °C to the lowest at 97.8 %H_2O at ΔT_{LMTD} of 10 °C.

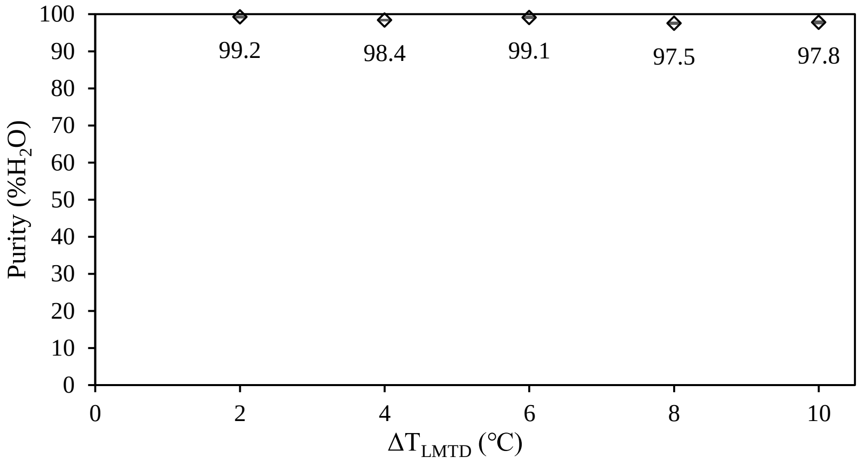

Figure 6.12: Ice purity at varying ΔT_{LMTD}

The purity of ice is determined by separation of ice and salt. It was expected that changes in magma density, M_T, would affect separation efficiency, but it was found that there were insignificant changes in the M_T when the ΔT_{LMTD} was increased. This is shown in Figure 6.13. Figure 6.13 shows the final M_Ts as the M_T could not be measured during the experiment. The changes in M_T were insignificant because as ΔT_{LMTD} increased, the ice in the bulk decreased, the salt in the bulk increased and the residual brine decreased.

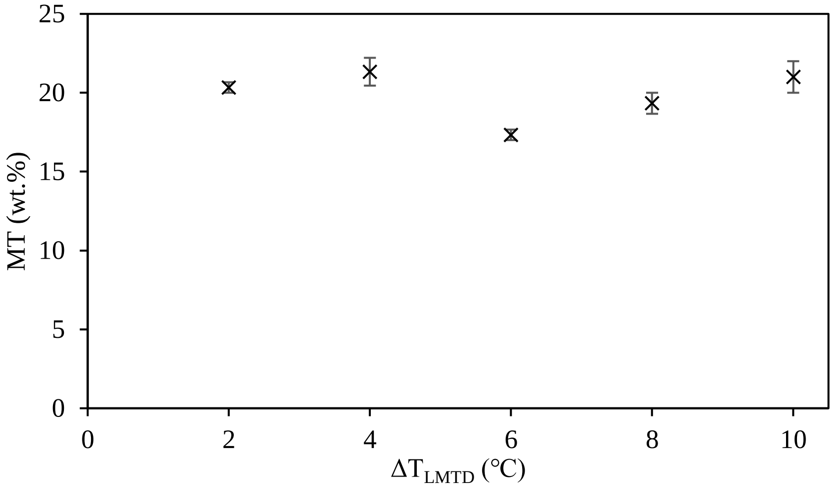

Figure 6.13: Effect of ΔT_{LMTD} on magma density

The reduction in purity can still be attributed to poor separation, however, the poor separation was due to the difference in ice and salt crystal sizes, rather than because of changes in magma density. The ice crystals were quite large while the salt particles were small. The ice crystals had d50s ranging from 1183 μm to 1527 μm, as shown in Table 6.3, and CSDs ranging from 250 to 2800 μm. The ice CSD is shown in Figure 6.14. The salt particles had d50s ranging from 71.9 μm to 96.7 μm, as shown in Table 6.3, and CSDs ranging from 20 to 250 μm. The salt PSD is shown in Figure 6.15.

Table 6.3: Effect of ΔT_{LMTD} on ice and salt d50

ΔT$_{LMTD}$ (°C)	**Ice d50 (μm)**	**Salt d50 (μm)**	
2	1183	71.9	16.5
4	1300	94.7	13.7
6	1300	90.8	14.4
8	1527	96.7	15.8
10	1515	95.7	15.8

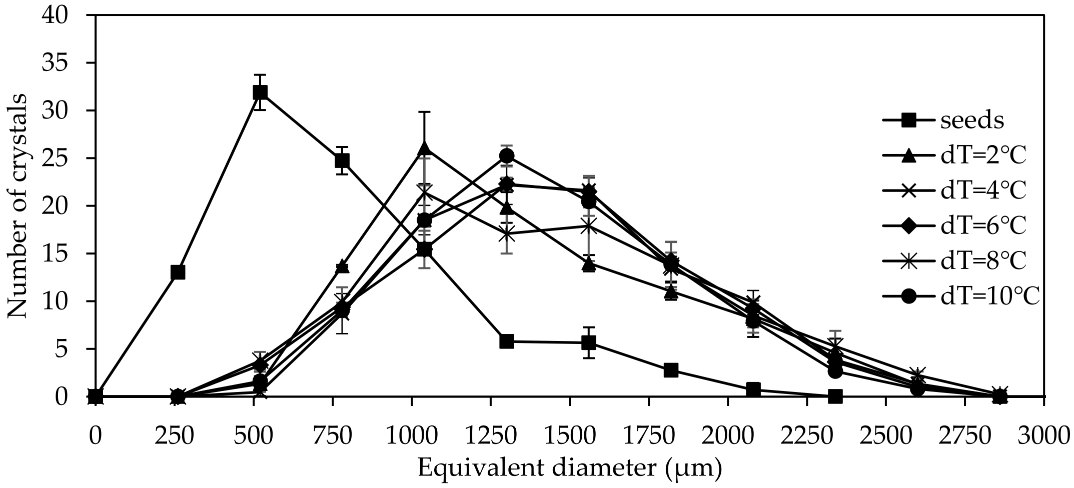

Figure 6.14: Effect of ΔT$_{LMTD}$ on ice product crystal size

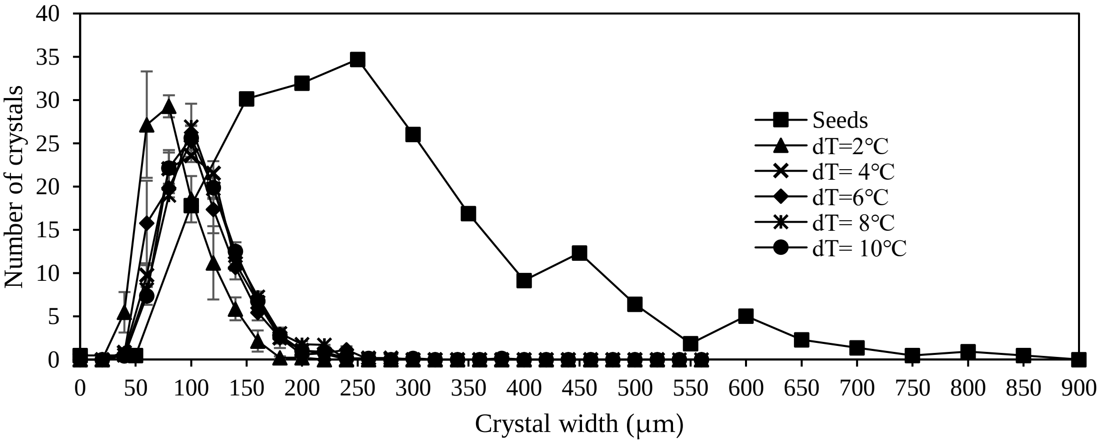

Figure 6.15: Effect of ΔT$_{LMTD}$ on salt product crystal size

The large difference in particle size (ice was >13 times larger than salt) resulted in the salt following the flow of the ice leading to salt entrainment. The inefficient separation was visible in the images of the ice product. These are shown in **Error! Reference source not found.** to REF _Ref82605208 \h **Error! Reference source not found.**. The small crystals around the larger ice crystals are salt crystals.

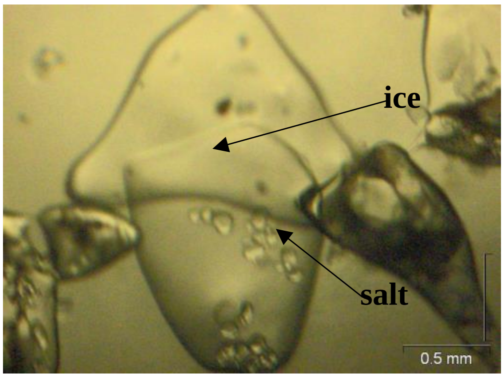

Figure 6.16: Typical image of ice product crystals at ΔT_{LMTD} =2°C

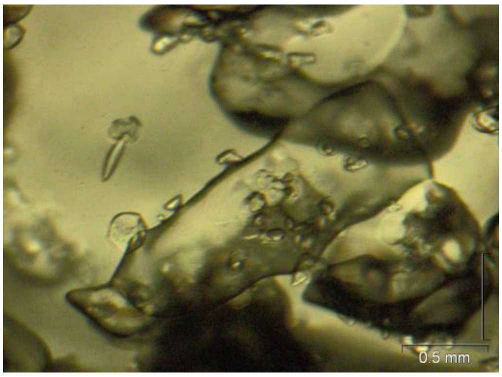

Figure 6.17: Typical image of ice product crystals at ΔT_{LMTD} =4°C

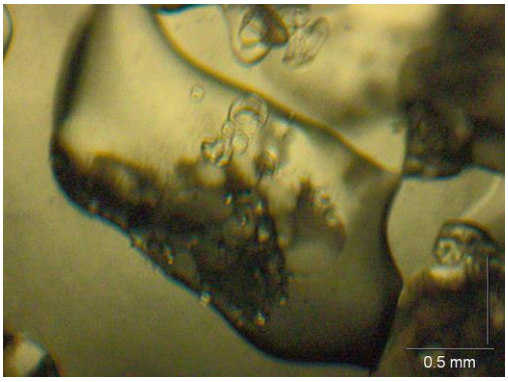

Figure 6.18: Typical image of ice product crystals at ΔT_{LMTD} =6°C

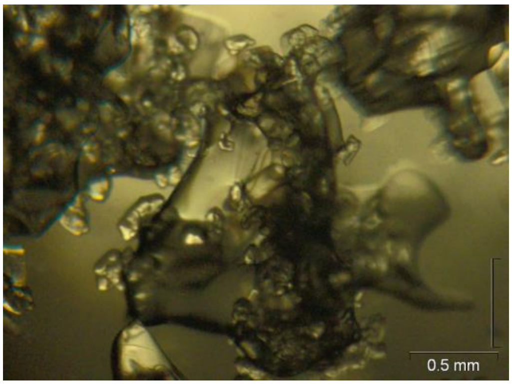

Figure 6.19: Typical image of ice product crystals at ΔT_{LMTD} =8°C

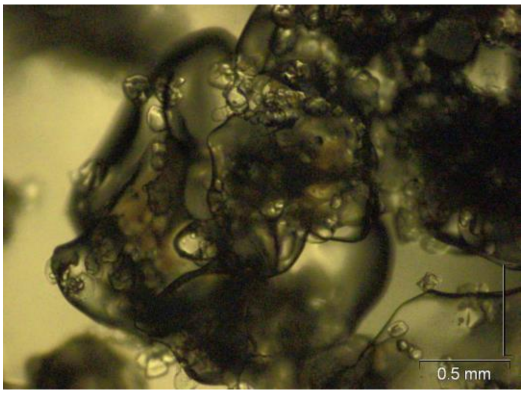

Figure 6.20: Typical image of ice product crystals at ΔT_{LMTD} =10°C

The images show that the severity of salt entrainment increased as the ΔT_{LMTD} increased. The CSDs show that when ΔT_{LMTD} was increased, the salt crystals became bigger. The expectation was that the entrainment would be reduced, however, this was not the case. The changes in salt crystal size with ΔT_{LMTD} were very small. The small changes in the salt crystal size in combination with the ice crystals becoming larger resulted in increased severity of entrainment, which was due to the difference in ice and salt crystal sizes becoming larger as ΔT_{LMTD} increased. The severity of entrainment could also have been exacerbated by increased production of salt in the bulk.

Poor separation could also have been due to high extent of mixing caused by the agitator speed and design. The agitator was designed to allow efficient suspension of the seeds. To achieve this effect, the impeller had a larger diameter than conventional heuristics prescribe (heuristics prescribe an impeller diameter that is $\frac{D_{crystallizer}}{3}$ but the impeller had a diameter of $\frac{D_{crystallizer}}{1.47}$). This design allowed efficient suspension of ice in the active volume, but it also resulted in thorough mixing, reducing chances of settling.

The ice crystals were larger than the ice seeds, which corroborates the findings in the work done by Kaboyashi and Shirai (1996) where they observed that ice crystals grew when a seed loading of 6 wt.% was used. The salt product on the other hand, was much finer than the seeds. This can be attributed to the fact that though 1g was enough to initiate salt crystallization, it was below the critical seed loading for the salt (Ws* was 17.3 g), so nucleation was more dominant than growth (Doki et al., 1999). Nucleation is known to result in fine product sizes. According to Doki et al. (1999), the salt CSD should be bimodal to show nucleation and growth, however, the salt CSD is unimodal. It is difficult to rule out the possibility of growth as growth is what makes crystals become visible, but growth is not reflected in the CSD. Due to this, the salt CSD can also be attributed to melting during handling and imaging as can be seen from the rounded edges of the salt product. Since the focus was on the ice, the critical seed loading for salt was not used as a decider for the salt seed loading.

6.3.2.2 Purity of ice on the wall

Figure 6.21 shows the scale purity obtained at different ΔT_{LMTD}s. The scale purity decreases by very small margins (0.3 %) with increasing ΔT_{LMTD}, from the highest purity of 97.9 %H_2O achieved when the ΔT_{LMTD} was 4 °C to the lowest at 97.5 %H_2O at ΔT_{LMTD} of 10 °C. The purity is shown for ΔT_{LMTD} of 4 °C and above because there was no scale layer when a ΔT_{LMTD} of 2 °C was used.

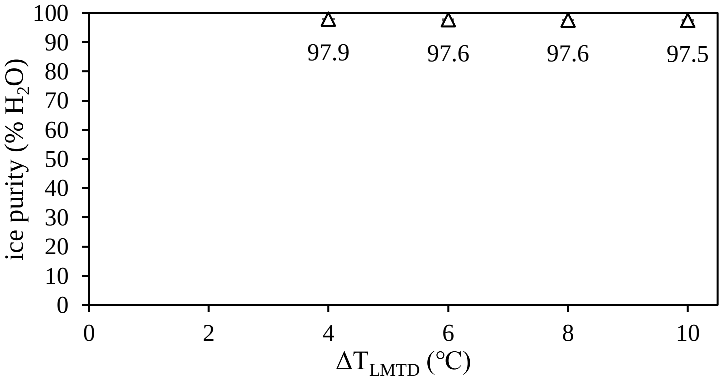

Figure 6.21: Effect of ΔT_{LMTD} on scale layer purity

The impurity could have been due to salt crystals or mother liquor getting trapped in the scale layer as it grew. The scale layer has a purity that is slightly lower than the ice formed in the bulk. This is expected since ice in the bulk can be physically separated from salt whereas any encapsulated/entrapped salt within the scale layer dissolves upon harvesting.

6.4 Effect of ice seed loading

6.4.1 Effect of ice seed loading on ice and salt yield

6.4.1.1 Effect of ice seed loading on ice yield: bulk and wall crystallization

Figure 6.22 shows the effect of ice seed loading on the yield of ice at a constant ΔT_{LMTD} of 4 °C. As in section 6.3.1.3, the total ice yield was split between the wall and bulk. The error bars associated with each data point are shown and are very small, which indicates that the results were reliably reproducible.

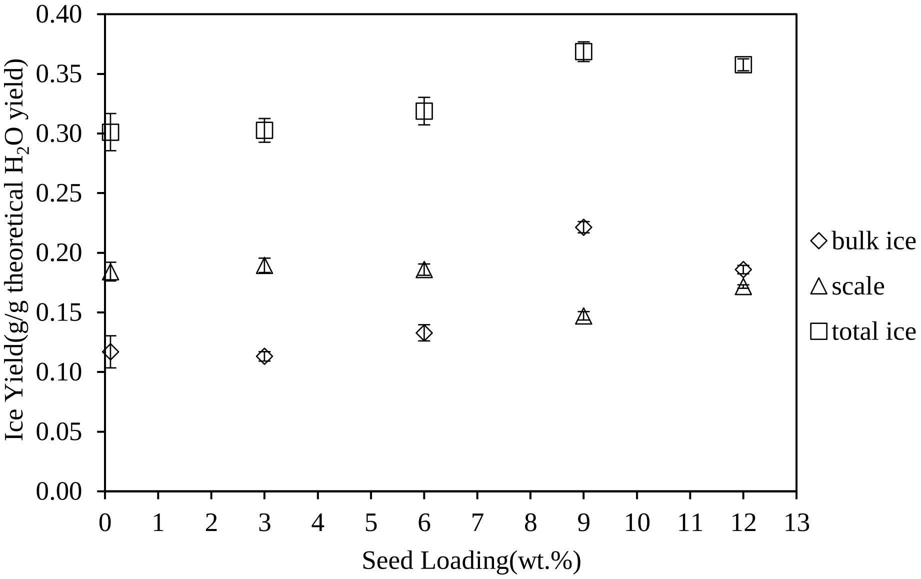

Figure 6.22: Effect of seed loading on ice yield

The total yield of ice increased with increasing seed loading with a maximum yield obtained at a seed loading of 9 wt.%. Figure 6.22 shows that there were insignificant changes in the scale yield when seed loadings were between 0 and 6 wt.%. Insignificant changes were also observed in the yield of ice in the bulk when seed loadings were between 0 and 3 wt.%. When the seed loading increased from 3 to 9 wt.% the yield of ice in the bulk increased with the maximum bulk ice yield being at 9 wt.%. While the ice in the bulk was at a maximum, a minimum in the yield of scale was obtained. Increasing the seed loading from 9 to 12 wt.% increased the yield of scale by 14%, but this yield was 8% less than the yields obtained at seed loadings of 6 wt.% and below. The increase in seed loading from 9 to 12 wt.% also resulted in a 16% reduction in the yield f ice in the bulk, but this yield was 35 % more than the yield of ice in the bulk when seed loadings below 6 wt.% were used.

With seed loadings between 0 and 6 wt.%, changes in the yield of scale were insignificant. During crystallization where cooling happens through a cooled wall, the boundary layer has the highest supersaturation. If this supersaturation is localised at the wall, heterogeneous nucleation will occur at the wall, resulting in a scale layer. Though the wall has higher supersaturation than the bulk, crystallization can be promoted in the bulk by using seeds. Seeds provide a surface with a lower energy barrier for nucleation than the wall (Lewis et al., 2015). As more seeds are added, more of the supersaturation is consumed by crystallization on the seed surface. When there is more crystallization in the bulk, the heat of crystallization that is released is increased. This allows for the boundary layer to be warmer, thereby reducing the supersaturation at the wall. This reduces heterogeneous nucleation of ice on the wall. The lack of change in the scale yield for seed loadings between 0 and 6 wt.% shows that seeds of 6 wt.% and below did not induce enough crystallization to cause the reduction of supersaturation within the boundary layer. When the ice seed loading was increased to 9 wt.%, the secondary nucleation introduced by the seeds resulted in reduction of supersaturation on the wall and, in turn, reduction of ice yield on the wall. The increased heating of the bulk and in turn the boundary layer due to increased crystallization, can be seen in the coolant inlet and outlet temperatures, particularly the difference between the temperature of the coolant inlet and outlet. $T_{c,out} - T_{c,in}$. $T_{c,out} - T_{c,in}$ was larger for seed loading of 9 wt.% than for 6 wt.%, as shown in Figure 6.23. A larger $T_{c,out} - T_{c,in}$ means that the coolant had to do more heat removal showing that more heat was being released by the bulk. The temperature profiles were reliably reproducible with the maximum variation at ±0.01 °C.

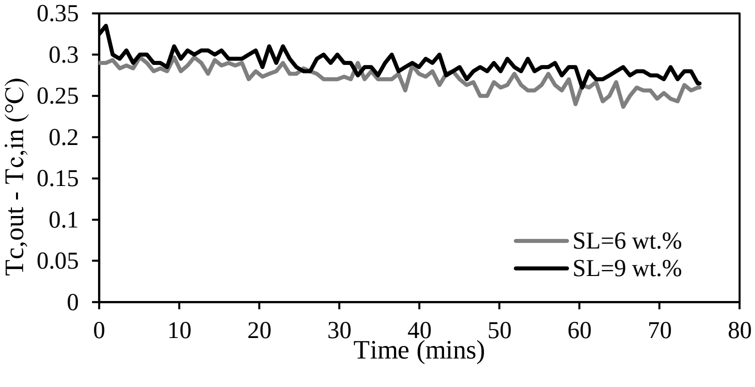

Figure 6.23: Effect of ice seed loading on $T_{c,out} - T_{c,in}$ for SL= 6 and 9 wt.%

When the seed loading was increased from 9 to 12 wt.% there was a decrease in the yield of ice in the bulk and an increase in the yield of scale. Increasing the seed loading increased the initial magma density, $M_{T,0}$. The magma density affected the hydrodynamics of the system by reducing mixing in the radial direction which in turn reduced the distribution of supersaturation from the wall to the bulk (Leyland, Chivavava & Lewis, 2019). The effect of the magma density on the hydrodynamics of the system can be seen in the changes in the Reynolds number, Re. Figure 6.24 shows the calculated Re at each seed loading upon introduction of the seeds. The Re dropped due to the greater solid content, which increased the viscosity of the bulk, hence the reduction in Re (Appendix 10.11).

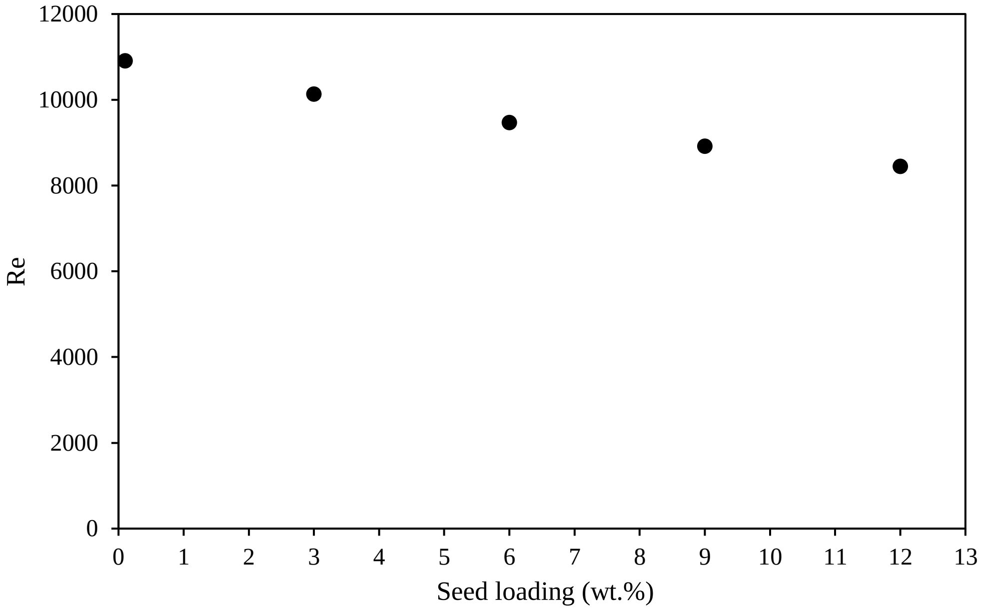

Figure 6.24: Effect of solid content on Reynolds number

A reduction in Re shows that the system had reduced mixing efficiency, which would result in a reduction in the distribution of supersaturation from the wall to the bulk, thereby increasing the resistance to heat transfer within the bulk. Increased resistance to heat transfer within the bulk would be reflected in a reduction in the process fluid heat transfer coefficient, $\alpha_{process}$ as was seen in the work done by Vaessen, Seckler and Witkamp (2004) . Figure 6.25 shows the initial values of $\alpha_{process}$.

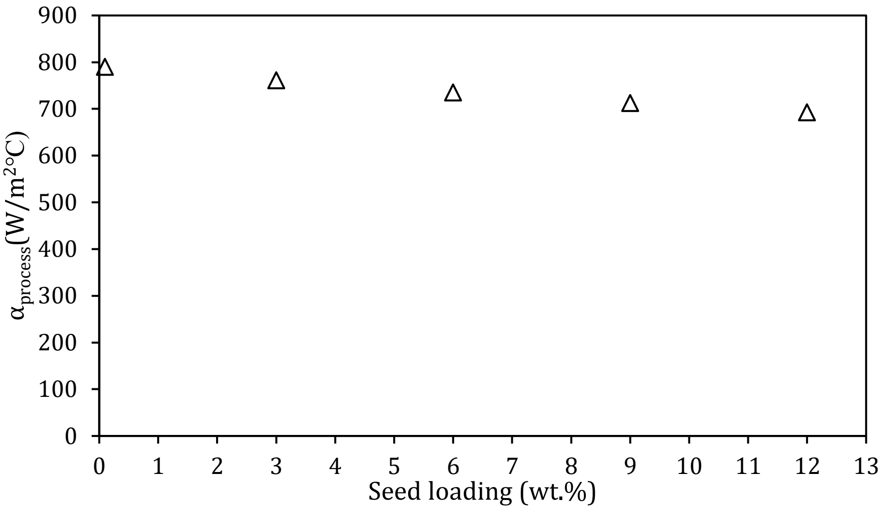

Figure 6.25: Effect of seed loading on process side heat transfer coefficient

From Figure 6.25, it can be seen that $\alpha_{process}$ did decrease with increasing seed loading. This was due to the reduction in Re. The reduction in $\alpha_{process}$ corroborates the explanation for the reduced distribution of supersaturation from the wall to the bulk. In such a case, the wall once again had high localised supersaturation leading to scale layer formation by heterogeneous nucleation. At 9 wt.%, the secondary nucleation produced enough heat to reduce the localised supersaturation at the wall such that the scale yield was minimised even though the mixing and $\alpha_{process}$ were reduced. This ceased to be a factor at 12 wt.% because the magma density effects on hydrodynamics became more important than secondary nucleation (Leyland, Chivavava & Lewis, 2019). At 9 wt.%, the system was operating within region II of the scaling potential illustration by Leyland, Chivavava and Lewis (2019), where the surface area of available ice induced enough crystallization to reduce supersaturation at the wall. Once 12 wt. % was used, however, the system was operating within Region III where the resistance to heat transfer in the bulk resulted in localised supersaturation at the wall and giving rise to a scale layer. This is illustrated in Figure 6.26.

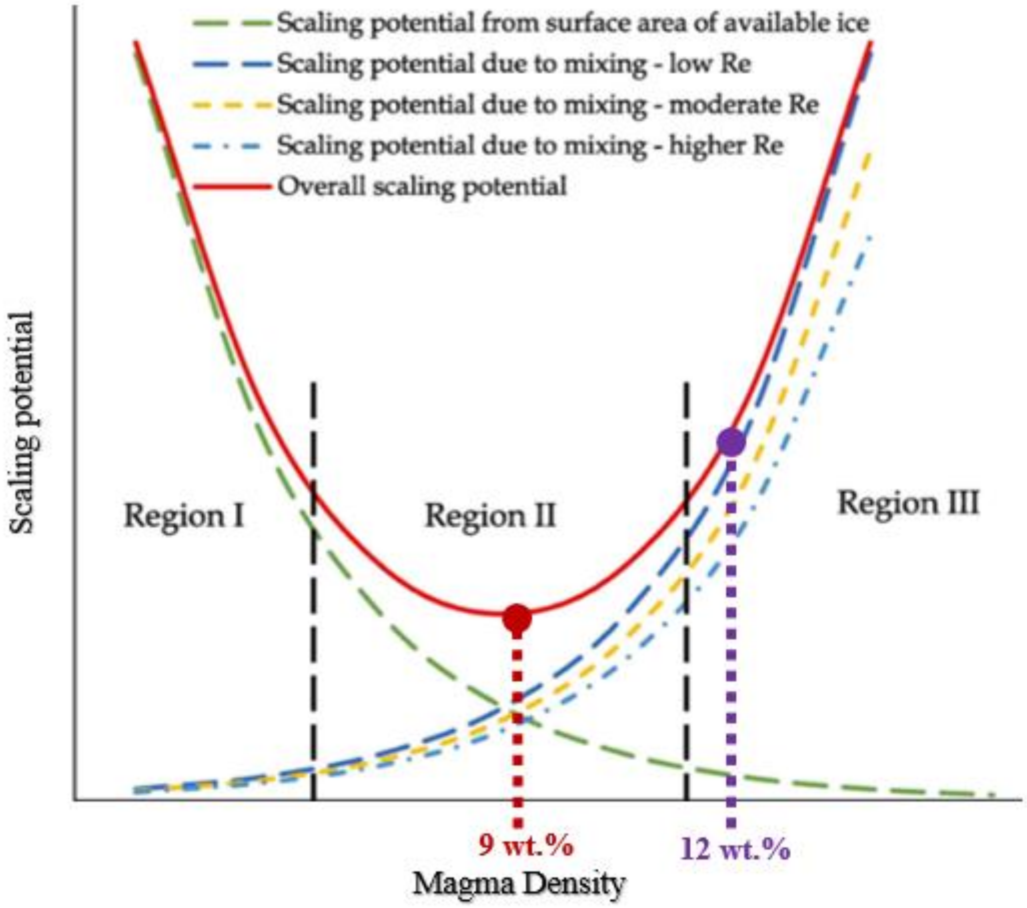

Figure 6.26: Magma density illustration adapted from Leyland, Chivavava and Lewis (2019)

The reduced heat transfer within the bulk resulted in reduced crystallization within the bulk and yielded less ice in the bulk.

6.4.1.2 Hypothesis- Effect of ice seed loading on bulk and wall crystallization

It was earlier hypothesised that the yield of ice in the bulk would increase while the yield of ice on the wall decreased when the seed loading was increased. The ice and scale yield confirmed the hypothesis for seed loading of 6 wt.% and above. The seeds did provide surface area for the reduction of scale formation. The seeds promoted secondary nucleation and growth in the bulk thus producing more ice in the bulk. The nucleation and growth in the bulk resulted in the release of heat of crystallization which allowed for the reduction of supersaturation at the wall, which resulted in the reduction of heterogeneous nucleation on the wall and subsequently the reduction of the yield of ice at the wall. It was also hypothesised that beyond a certain seed loading, the yield of ice on the wall would increase while the yield of ice in the bulk decreased. This was found to be true when a seed loading of 12 wt.% was used. An ice seed loading of 12 wt.% reduced the mixing efficiency of the system, resulting in localised supersaturation at the wall which produced a scale layer. The reduced mixing efficiency increased the resistance to heat transfer within the bulk, causing reduced crystallization within the bulk and less ice in the bulk.

6.4.1.3 *Effect of ice seed loading on salt yield*

Figure 6.27 shows the effect of ice seed loading on salt yield. Lower salt yields were obtained at higher seed loadings.

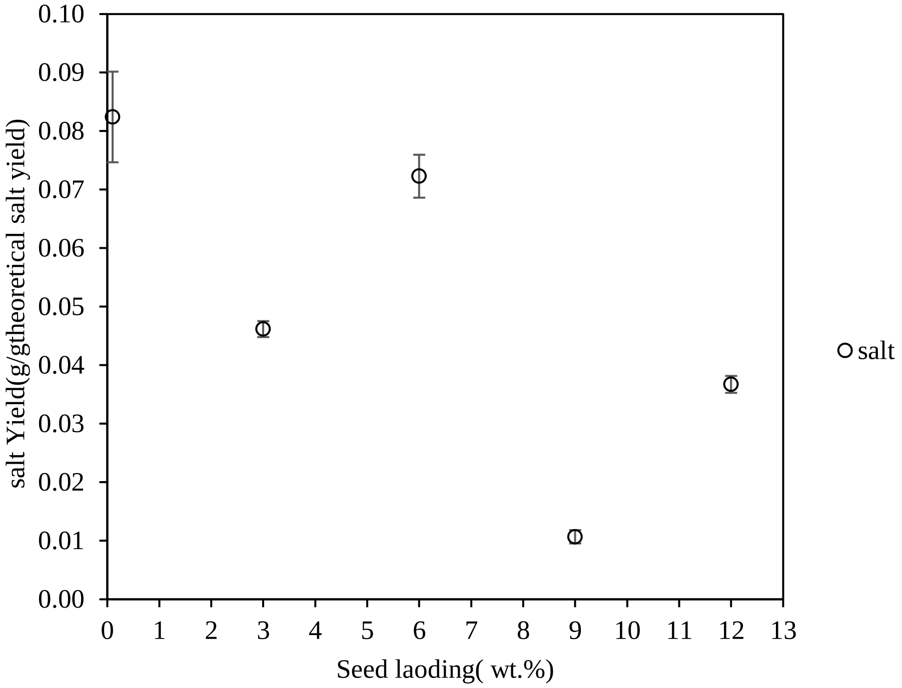

Figure 6.27: Effect of seed loading on salt yield

The reduction in the yield of salt with seed loading indicates poor separation. As the seed loading increased, the ice crystals obtained were very large with d50s ranging from 1636 to 1786 µm and PSDs ranging from 500 to 2800 µm. The salt crystals on the other hand, were small with PSDs ranging from 20 to 300 µm and d50s ranging from 85.4 to 105.9 µm. This is shown in Table 6.4, Figure 6.28 and Figure 6.29.

Table 6.4: Effect of SL on ice and salt d50

SL(wt.%)	Ice d50 (µm)	Salt d50 (µm)
0.1	1786	105.9
3	1636	95.9
6	1560	94.7
9	1744	85.4
12	1663	87.4

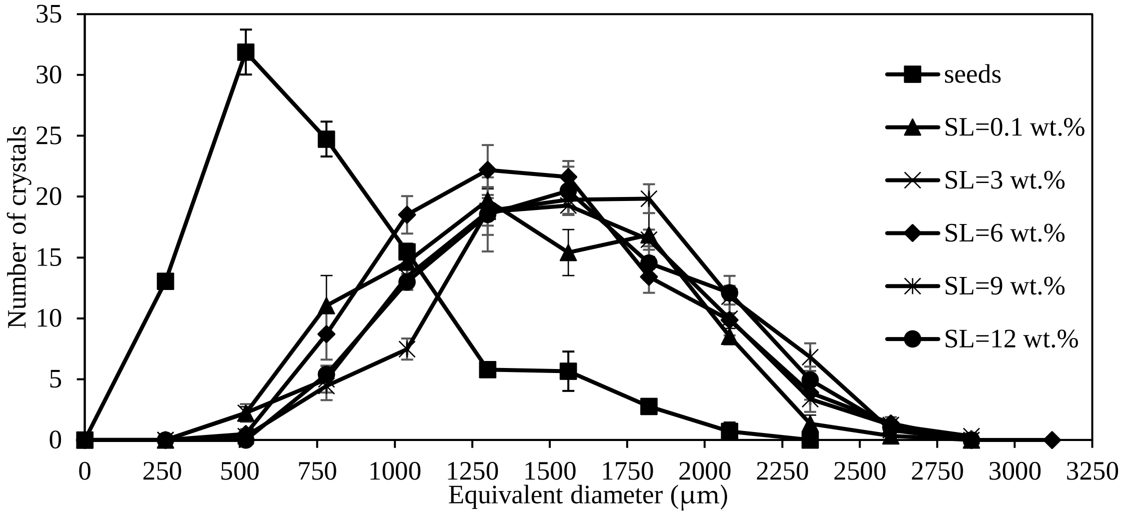

Figure 6.28: Effect of ice seed loading on product ice size

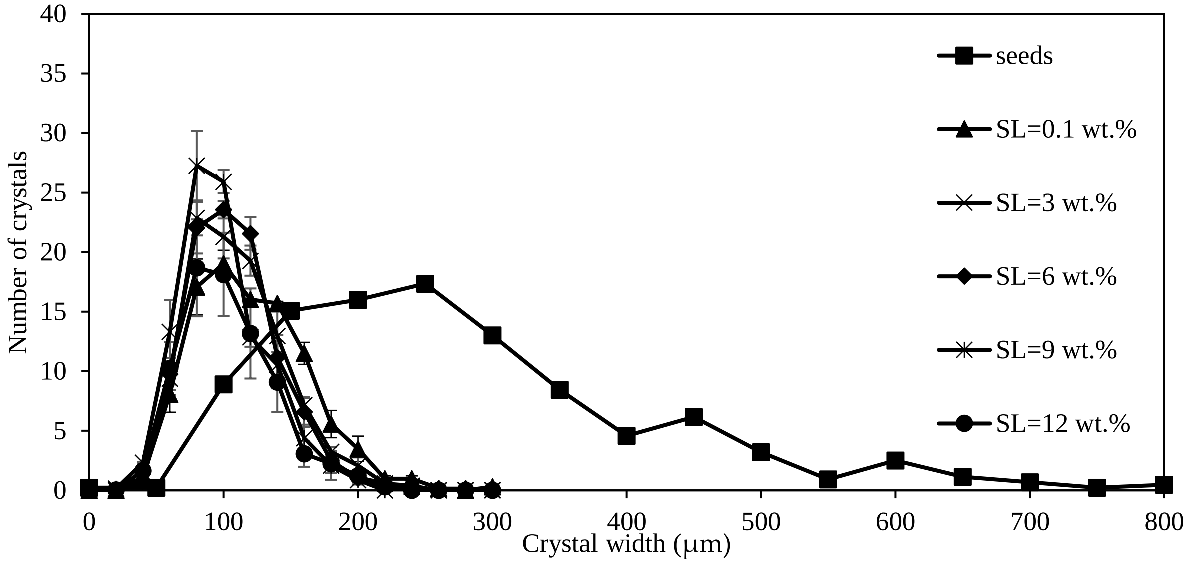

Figure 6.29: Effect of ice seed loading on salt product size

As with the ΔT_{LMTD} experiments, the salt was fine due to melting and due to the salt seed loading being below the critical salt seed loading (16.3 g ≤ Ws* ≤ 18.4 g). The low salt seed loading promoted nucleation rather than growth (Doki et al., 1999) resulting in the fine salt crystals. The large difference in size between ice and salt (ice was over 16 times larger than salt) and high extent of mixing resulted in salt entrainment in the ice product. The salt entrainment became more severe as the ice seed loading increased as a result of the increase in the magma density. The entrainment and increase in severity with seed loading was evident in the increase in salt obtained in the wash water, shown in Figure 6.30 (assuming most of the detected salt is from washed crystals and a negligible amount is from mother liquor entrainment). The entrainment and increase in severity with seed loading was also evident in the ice product images (Figure 6.31 to Figure 6.35) which were taken of the ice before washing.

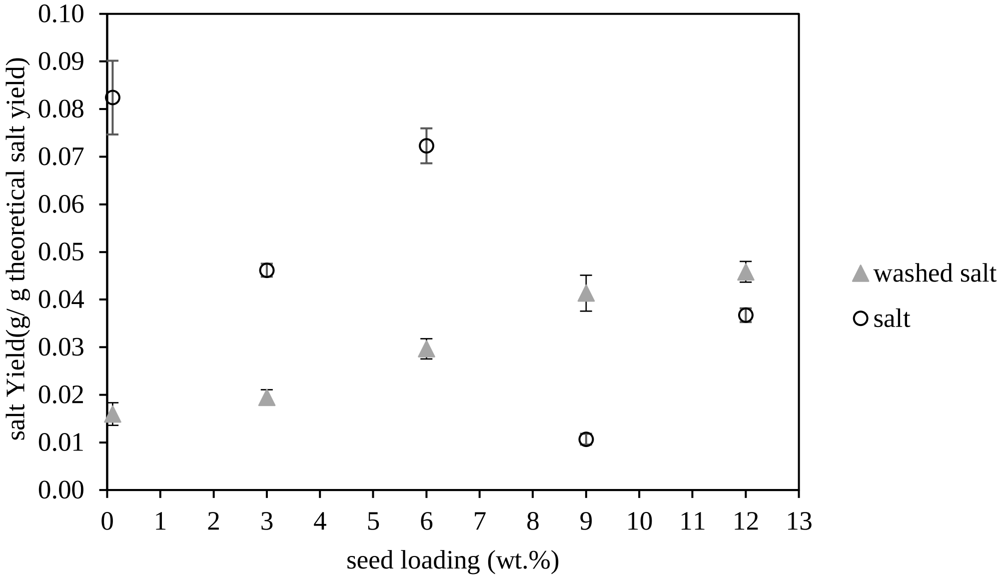

Figure 6.30: Effect of seed loading on washed salt

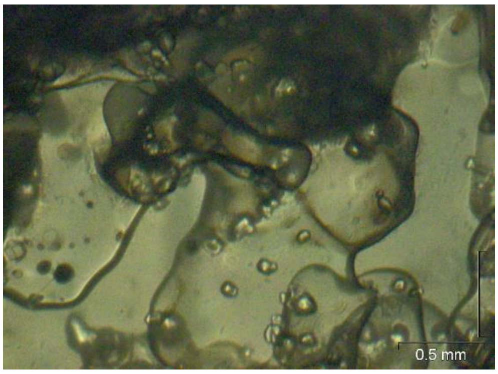

Figure 6.31: Typical ice product at SL=0.1 wt.%

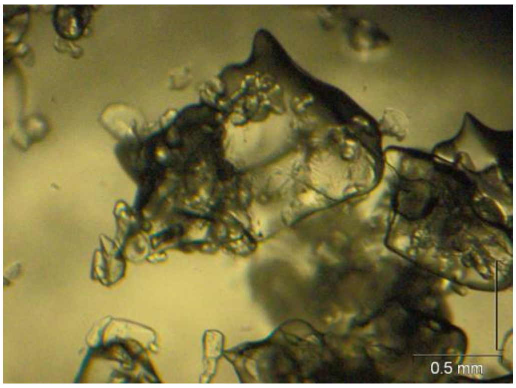

Figure 6.32: Typical ice product at SL=3 wt.%

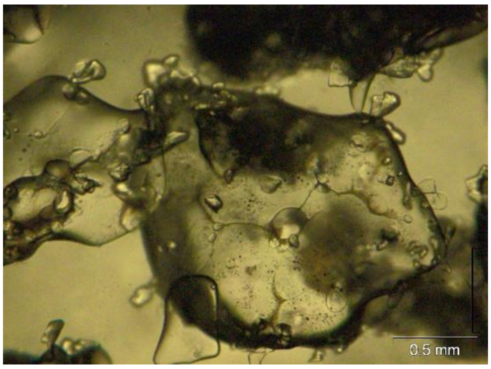

Figure 6.33: Typical ice product at SL=6 wt.%

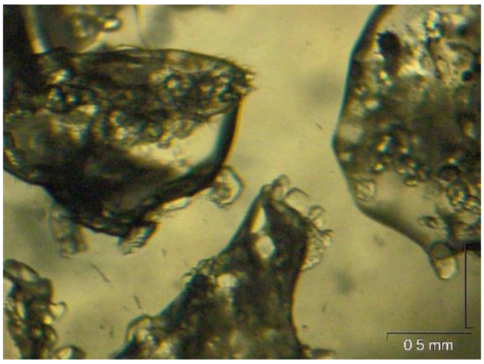

Figure 6.34: Typical ice product at SL=9 wt.%

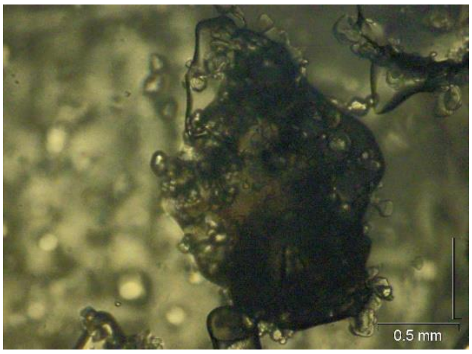

Figure 6.35: Typical ice product at SL=12 wt.%

Figure 6.30 shows that at seed loadings of 9 wt.% and above, there was more washed salt than harvested salt. This further confirms that the poor separation of salt from ice led to salt being entrained in ice and later washed off the ice, rather than being harvested, and leading to low salt yields at higher seed loadings.

Though the seed loadings for ice were all below the critical seed loading, the seeds grew. Even for the seed loading of 0.1 wt.% where mostly nucleation would be expected due to the low seed loading, the crystals that nucleated out of solution had enough time to grow to sizes larger than the seeds. The growth experienced in this study contradicts the findings by Kaboyashi and Shirai (1996). In the work done by Kaboyashi and Shirai (1996), when the seed loading was low, the product crystals were smaller than the seeds, showing there was mostly nucleation. The growth here could have been due to the low concentration of the brine; the brine in the work by Kaboyashi and Shirai (1996) was a 10 wt.% glucose solution while the brine used in this study was a 4wt.% Na_2SO_4 solution. The low concentration means the supersaturation was low which allowed for growth to be more dominant than nucleation.

6.4.2 Effect of seed loading on purity of ice

6.4.2.1 Purity of ice in the bulk

Figure 6.36 shows the purity of the ice obtained when different ice seed loadings were used. The ice purity increased with increasing seed loading. The lowest purity of 97.2 %H_2O was achieved when 0.1 wt.% seed loading was used, while the highest purity of 98.8 %H_2O was achieved with 12 wt.% seed loading. The volume of the seeds was not used in calculating the purity of the product to avoid dilution error.

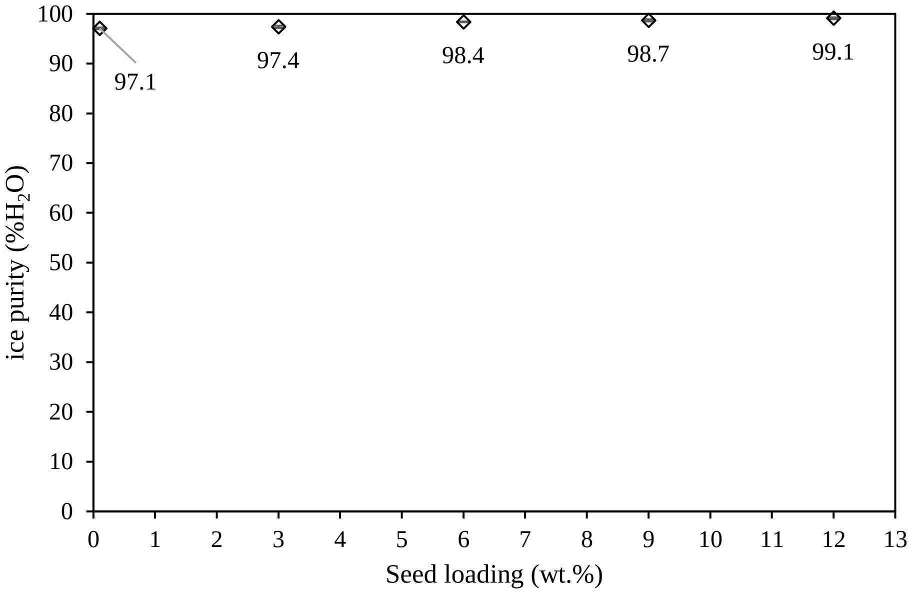

Figure 6.36: Effect of seed loading on ice purity

As the seed loading increased, the salt product became finer, as shown by the d50s in Table 6.4. This led to entrainment in the ice product. Wash water was used during the experiments for all the seed loadings. For higher seed loadings where the yield was higher, more wash water was used on finer salt crystals. This led to more efficient removal of salt from the ice product, as shown by the increase in salt obtained in the wash water as the seed loading increased (Figure 6.30).

6.4.2.2 Purity of ice on the wall

Figure 6.37 shows the purity of the ice scale layer obtained when different ice seed loadings were used. The ice purity decreased with increasing seed loading from the highest purity of 98.6 %H_2O, achieved using 0.1 wt.% seed loading, to the lowest at 97.8 %H_2O when 12 wt.% seed loading was used. As the seed loading increased, the salt product became finer. Having finer salt crystals resulted in easier entrapment while the scale layer grew as the finer crystals took longer to settle.

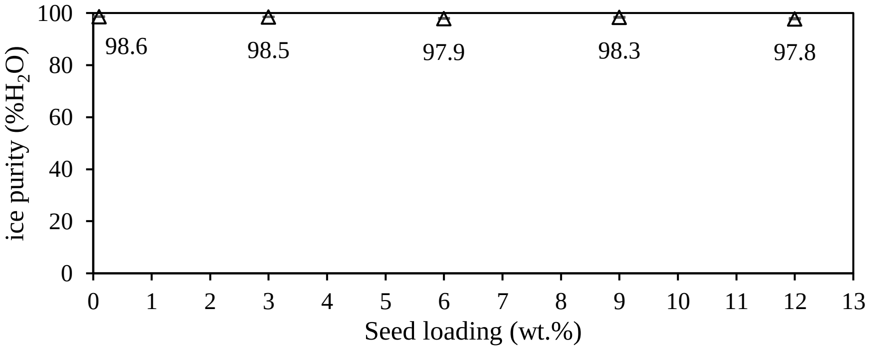

Figure 6.37: Effect of seed loading on scale purity

The presence of impurities in a layer of ice that grew on a surface was observed by Shirai et al. (1999) in the work on freeze crystallization from a polypeptone solution. The impurities were from the mother liquor because only ice was crystallizing out of solution. Mother liquor inclusion is common in freeze crystallization due to the high supersaturations used there, whereas in EFC, the supersaturation is low, so the probability of salt crystal entrapment is more likely.

7 CONCLUSIONS

The aim of this study was to investigate and understand the effect of heat transfer driving force, ΔT_{LMTD}, and ice seed loading, on the production of ice and salt, and on the purity of ice from a dilute brine. The effect of these two operating conditions was tested in a 1.45L crystallizer at varying coolant temperatures for the effect of $\Delta T_{LMTD,}$ and at varying seed masses.

It was found that as the ΔT_{LMTD} increased, the yield of ice and salt increased. The ice and salt yields increased because there was an increase in the heat transfer rate, since ΔT_{LMTD} and heat transfer rate are directly related. The ice yield was the sum of ice harvested from the bulk and the ice formed on the wall. The yield of ice in the bulk was reduced when ΔT_{LMTD} was increased, whilst the yield of ice on the wall (scale) increased. The increase in yield of scale with ΔT_{LMTD} came from the fact that increasing the ΔT_{LMTD} resulted in an increase in the supersaturation at the wall. High supersaturation at the wall led to the formation of a scale layer. As the ΔT_{LMTD} increased, the scale layer became larger because the time lapse before the scale formed became shorter. Having a larger scale layer meant that the resistance to heat transfer from the bulk to the coolant grew, therefore the yield of ice in the bulk decreased with increasing ΔT_{LMTD}.

This study also found that the intense nature of agitation and salt particle entrainment resulted in poor separation. The salt entrainment was due to the large difference between ice and salt crystal sizes. The entrainment became more severe as ΔT_{LMTD} increased because salt production in the bulk increased. Both scale and ice from the bulk were purer than the mother liquor, with the ice in the bulk being purer than the scale.

As for the effect of ice seed loading, it was found that as the ice seed loading increased, the yield of ice in the bulk increased, while the yield of ice on the wall decreased. The increase in ice production in the bulk happened because increasing the seed loading increased secondary nucleation in the bulk, thereby increasing the heat of crystallization released into the bulk. The heat released reduced the supersaturation at the wall by heating up the boundary layer. The reduced supersaturation at the wall diminished the tendency for scale formation. A maximum in the ice in the bulk and minimum in the scale were observed when a seed loading of 9 wt.% was used. Once the seed loading was increased to 12 wt.%, the benefit of the heat of crystallization was superseded by the impediment of mixing because of the greater magma density. The increase in magma density reduced mixing which in turn reduced the distribution of supersaturation from the wall. The reduced mixing led to localised supersaturation at the wall such that a scale layer formed. This resulted in an increase in the yield of the scale. The reduction in the mixing raised heat transfer resistance within the bulk such that crystallization within the bulk was reduced, which meant there was less ice in the bulk.

It was also found that the salt yield was very low at higher seed loadings (0.01-0.04 g/gtheoretical salt yield) caused by poor separation. The low salt seed loading resulted in fine salt product as nucleation was promoted instead of growth. The fine salt product was entrained in the ice product such to the degree that most of the salt was harvested in the wash water rather than as a pure salt product. The entrainment became more severe as the ice seed loading increased because of the increased magma density. Due to the fine nature of the salt, washing the ice became more efficient resulting in purer ice product.

It can be concluded that that ice seeds can be used to control where ice crystallization occurs once the optimum seed loading has been identified. This study shows that these operating conditions of a crystallizer affect the amount of ice and salt that can be produced from a brine, and in turn the achievable product purities. The understanding and knowledge of the relationship between operating conditions and output production variables allows for the identification of optimums as well as the responsible mechanisms. This in turn allows for better application of the EFC process.

8 RECOMMENDATIONS

This study showed the effect of ΔT_{LMTD} and ice seed loading on the production of ice and salt from a dilute brine in batch operational mode. This study is the first of its kind where ice seeds were a focal point in EFC as salt seeding studies are more common in literature. Carrying out the experiments in batch mode allowed for the development of the first stages of understanding the relationship between $\Delta T_{LMTD,}$ seed loading and production of ice and salt. The first recommendation is to carry this work into continuous mode, to allow for further understanding of crystallization of ice and salt from dilute brines.

It is recommended that a narrower range for the effect of ΔT_{LMTD} should be tested to see if a maximum in the yield of ice in the bulk exists or not. Results from these experiments on a Na_2-SO_4-H_2O system suggest that a maximum may exist between ΔT_{LMTD} of 2 and 4 °C. This shows that it is possible that each system may have this maximum, so it is recommended that this study be carried out on other systems as well.

It is also recommended that the effect of ice seed loading on other systems be investigated as a maximum in the yield was observed. This shows that a maximum may exist for every system, so it is recommended that the maximum be identified for each system.

Since the focus of this work was on ice seed loading in an EFC system, it is recommended that the effect of salt seed loading in an EFC system be investigated as well and from there an optimum for both ice and salt seed loading be identified.

The study was carried out in a simple cylindrical crystallizer, so it is recommended that similar studies be done in different geometries to incorporate an optimise in-situ separation. The study also highlights the need for investigations on downstream processes, such as the relationship between washing mechanisms and product size, as this affected the salt yield and purity obtained.

9 REFERENCES

1. Aspeling, B.J. 2019. Selective recovery of salts from a ternary eutectic system in EFC using seeding. Masters. University of Cape Town.
2. Deissler, R.G. 1955. Turbulent heat transfer and friction in the entrance regions of smooth passages. *Trans. ASME.* 77(8):1221-1232.
3. Dhanaraj, G., Byrappa, K., Prasad, V. & Dudley, M. 2010. *Springer handbook of crystal growth.* Springer.
4. Dittus, F.W. & Boelter, L.M.K. 1930. *Heat transfer in automobile radiators of the tubular type.* University of California Press. Available: https://books.google.co.za/books?id=Sh4DJgAACAAJ.
5. Doki, N., Kubota, N., Yokota, M. & Chianese, A. 2002. Determination of critical seed loading ratio for the production of crystals of uni-modal size distribution in batch cooling crystallization of potassium alum. *Journal of Chemical Engineering of Japan.* 35(7):670-676.
6. Doki, N., Kubota, N., Sato, A., Yokota, M., Hamada, O. & Masumi, F. 1999. Scaleup experiments on seeded batch cooling crystallization of potassium alum. *AIChe.* 45(12):2527-2533.
7. DWS, D.o.W.a.S. 2017. *Strategic overview of the water sector In south Africa 2017.* Pretoria, South Africa: Government of South Africa.
8. Eder, R.J.P., Schmitt, E.K., Grill, J., Radl, S., Gruber-Woelfler, H. & Khinast, J.G. 2011. Seed loading effects on the mean crystal size of acetylsalicylic acid in a continuous flow crystallization device. *Crystal Research and Technology.* (3):227-237.
9. Genceli, F.E. 2008. Scaling up eutectic freeze crystallization. PhD. Delft University of Technology.
10. Genceli, F.E., Gärtner, R. & Witkamp, G.J. 2005. Eutectic freeze crystallization in a 2nd generation cooled disk column crystallizer for $MgSO_4 \cdot H_2O$ system. *Journal of Crystal Growth.* 275(1-2):e1369-e1372. DOI:10.1016/j.jcrysgro.2004.11.172.
11. Genceli , F.E., Popescu, D., Gärtner, R., Rodriguez, M. & Witkamp, G.-J. 2005. 3rd generation cooled disk column crystallizer and a skid mounted unit for eutectic freeze crystallization. *16th Annual Symposium on Industrial Crystallization*. 11-14 September 2005. 855-860.
12. Haan, A.B.d. & Bosch, H. 2013. Crystallization and precipitation. In *Industrial separation processes fundamentals.* Germany. 207-239.
13. Hofmann, G. & Melches, C. 2013. Continuous crystallization. In *Crystallization: Basic Concepts and Industrial Applications.* W. Beckmann, Ed. Germany: Wiley-VCH. 203-207.
14. Hojjati, H. & Rohani, S. 2005. Cooling and seeding effect on supersaturation and final crystal size distribution of ammonium sulphate in a batch crystallizer. *Chemical Engineering and Processing.* 44:949-957.
15. Johnson, D.B. & Hallberg, K.B. 2005. Acid mine drainage remediation options: a review. *Science of the Total Environment.* 338(1):3-14.
16. Jooste, D. 2016. Ice ccaling in continuous eutectic freeze crystallization. Masters. University of Cape Town.
17. Kaboyashi, A. & Shirai, Y. 1996. A method for making large agglomerated ice crystals for freeze crystallization. *Journal of Food Engineering.* (27):1-15.
18. Kadi, K.E. & Janajreh, I. 2017. Desalination by freeze crystallization: an overview. *International Journal of Thermal & Environmental Engineering.* 15(2):103-110. DOI:10.5383/ijtee.15.02.004.

19. Kapembwa, M., Rodríguez-Pascual, M. & Lewis, A.E. 2014. Heat and mass transfer effects on ice growth mechanisms in pure water and aqueous solutions. *Crystal Growth and Design.* (14):389-395.
20. Lewis, A., Seckler, M., Kramer, H. & van Rosmalen, G. 2015. *Industrial crystallization fundamentals and applications.* Alison Lewis. United Kingdom: Cambridge University Press.
21. Leyland, D., Chivavava, J. & Lewis, A.E. 2019. Investigations into ice scaling during eutectic freeze crystallization of brine streams at low scraper speeds and high supersaturation. *Separation and Purification Technology.* 220:33-41. DOI:10.1016/j.seppur.2019.03.025.
22. Lung-Somarribaa, B.L.M., Moscosa-Santillanb, M., Portea, C. & Delacroixa, A. 2004. Effect of seeded surface area on crystal size distribution in glycine batch cooling crystallization: a seeding methodology. *Journal of Crystal Growth.* 270(3):624-632.
23. Luo, T., Young, R. & Reig, P. 2015. Aqueduct projected water stressed country rankings. Available: https://www.wri.org/publication/aqueduct-projected-water-stress-country-rankings:1-15.
24. Mardles, E.W.J. 1940. Viscosity of suspensions and the einstein equation. *Nature.* 145:970.
25. Mehlo, B. 2019. The Characterization and Thermodynamic Analysis of Selected Brine Systems for technically focused Treatment Process selection. Masters. University of Cape Town.
26. Motsepe, L. 2020. Investigating the effect of surface properties on ice scaling in eutectic freeze crystallization. Masters. University of Cape Town.
27. Mullin, J.W. 2001a. Crystal Growth. In *Crytallization.* Oxford: Butterworth-Heinemann. 216-260.
28. Mullin, J.W. 2001b. *Crystallization.* 4th. Oxford: Butterworth-Heinemann.
29. Myerson, A.S. 2002. *Handbook of industrial crystallization.* 2. Woburn: Butterworth Heinemann.
30. OLI-Systems-Inc. 2020. *OLI Studio 10.0* Morris Plains, New Jersey, USA: OLI Systems Inc.
31. Petrenko, V.F. 1993. *Electrical properties of ice*. (Report). Hanover, Germany.
32. Qin, F.G.F., Chen, X.D. & Russell, A.B. 2003. Heat transfer at the subcooled-scraped surface with/without phase change. *AIChe.* 49(8):1947-1955.
33. Randall, D.G. 2010. Development of a brine treatment protocol using eutectic freeze crystallization. PhD. University of ape Town.
34. Randall, D.G. 2011. A case study for treating a reverse osmosis brine using Eutectic Freeze Crystallization—Approaching a zero waste process. *Desalination.* (266):256-262.
35. Reddy, S.T., Kramer, H.J.M., Lewis, A.E. & Nathoo, J. 2009. Investigating factors that affect separation in a eutectic freeze crystallisation process. *International Mine water Conference*. Pretoria, South Africa, 2009. 649-655.
36. Rodriguez-Pascual, M., Genceli, F.E., Trambitas, D.O., Evers, J., Spronsen, J.V. & Witkamp, G.J. 2010. A novel scraped cooled wall crystallizer: recovery of sodium carbonate and ice from an industrial aqueous solution by eutectic freeze crystallization *Chemical Engineering Research and Design.* 88(9):1252-1258. DOI:10.1016/j.cherd.2009.07.015.
37. Schaschke, C. 2014. *A Dictionary of Chemical Engineering.* Great Britain: Oxford University Press.

38. Schneider, C.A., Rasband, W.S. & Eliceiri, K.W. 2012. NIH Image to ImageJ: 25 years of image analysis. *Nature Methods.* 10.1038/nmeth.2089(9(7)):671-675. DOI:10.1038/nmeth.2089.
39. Shirai, Y., Wakisaka, M., Miyawaki, O. & Sakashita, S. 1999. Effect Of seed ice on formation of tube ice with high purity for a freeze wastewater treatment system with a bubble-flow circulator. *Water Research.* 33(5):1325-1329.
40. Ulrich, J. & Stelzer, T. 2011. Crystallization. In *Kirk-Othmer Encyclopaedia of Chemical Technology*. 5th ed.: Wiley & Sons. 1-63. DOI:10.1002/0471238961.
41. Vaessen, R.J.C. 2003. Development of scraped eutectic crystallizers. PhD. Technical University of Delft.
42. Vaessen, R.J.C., Seckler, M.M. & Witkamp, G.J. 2004. Heat transfer in scraped eutectic crystallizers. *International Journal of Heat and Mass Transfer.* 47(4):717-728. DOI:10.1016/j.ijheatmasstransfer.2003.07.028.
43. Vaessen, R.J.C., Janse, B.J.H., Seckler, M.M. & Witkamp, G.J. 2003. Evaluation of the performance of a newly developed eutectic freeze crystallizer. *Chemical Engineering Research and Design.* 81(10):1363-1372. DOI:10.1205/026387603771339573.
44. Van der Ham, F., Seckler, M.M. & Witkamp, G.J. 2004. Eutectic freeze crystallization in a new apparatus: the cooled disk column crystallizer. *Chemical Engineering and Processing.* 43:161-167.
45. Van der Ham, F., Witkamp, G.J., de Graauw, J. & Van Rosmalen, G.M. 1998. Eutectic freeze crystallization: Application to process streams and wastewater purification. *Chemical Engineering and Processing: Process Intensification.* 37(2):207-213.
46. Water Resources Group. 2009. *Charting our water future*. (Report). South Africa.
47. Welty, J.R., Wicks, C.E., Wilson, R. & Rorrer, G.L. 2000. Fundamentals of heat transfer. In *Fundamentals of Momentum, Heat, and Mass Transfer.* 5th ed. Corvallis, Oregon: John Wiley & Sons, Inc. 201-213.

10 APPENDICES

10.1 Calculation of ΔT_{LMTD}

The equation for the calculation of ΔT_{LMTD} is shown in equation *10.1*.

$$\Delta T_{LMTD} = \frac{T_{coolant,in} - T_{coolant,out}}{\ln\left(\frac{T_{coolant,in} - T_{bulk}}{T_{coolant,out} - T_{bulk}}\right)} \tag{10.1}$$

This was calculated for each set of temperature measurements as shown in Table 10.1. An average ΔT_{LMTD} was then calculated from the point of seeding. The data for a ΔT_{LMTD} = 6 experiment was used as an example. All the ΔT_{LMTD} values for all the ΔT_{LMTD} and seed loading experiments were calculated in this way.

Table 10.1: ΔT_{LMTD} calculation for ΔT_{LMTD} = 6 as an example

Time	**$T_{C,in}$**	**$T_{C,out}$**	**T_{bulk}**	**tco-tcin**	**tcoo-tb**	**tci-tb**	**$\ln\left(\frac{T_{coolant,in} - T_{bulk}}{T_{coolant,out} - T_{bulk}}\right)$**	**ΔT_{LMTD}**
min	**°C**							
0	19.77	19.28	20.6	-0.49	-1.32	-0.83	0.464	-1.06
0.70	15.02	15	20.6	-0.02	-5.6	-5.58	0.004	-5.59
1.73	10.64	10.65	20.47	0.01	-9.82	-9.83	-0.001	-9.82
2.52	6.87	6.92	19.92	0.05	-13	-13.05	-0.004	-13.02
3.22	3.59	3.8	19.16	0.21	-15.36	-15.57	-0.014	-15.46
4.22	0.46	0.85	18.27	0.39	-17.42	-17.81	-0.022	-17.61
5.07	-2.18	-1.7	17.29	0.48	-18.99	-19.47	-0.025	-19.23
5.92	-4.66	-4.22	16.24	0.44	-20.46	-20.9	-0.021	-20.68
6.77	-6.89	-6.43	15.14	0.46	-21.57	-22.03	-0.021	-21.80
7.62	-7.94	-7.06	14.02	0.88	-21.08	-21.96	-0.041	-21.52
8.47	-6.35	-5.66	12.21	0.69	-17.87	-18.56	-0.038	-18.21
9.33	-6.42	-5.78	10.92	0.64	-16.7	-17.34	-0.038	-17.02
10.20	-6.92	-6.22	9.68	0.7	-15.9	-16.6	-0.043	-16.25
11.05	-7.25	-6.54	8.54	0.71	-15.08	-15.79	-0.046	-15.43
11.90	-7.46	-6.81	7.45	0.65	-14.26	-14.91	-0.045	-14.58
12.73	-7.46	-6.82	6.44	0.64	-13.26	-13.9	-0.047	-13.58
13.58	-7.41	-6.94	5.5	0.47	-12.44	-12.91	-0.037	-12.67
14.43	-7.61	-7.06	4.62	0.55	-11.68	-12.23	-0.046	-11.95
15.28	-7.56	-7.04	3.8	0.52	-10.84	-11.36	-0.047	-11.10
16.13	-7.55	-7.05	3.05	0.5	-10.1	-10.6	-0.048	-10.35

16.98	-7.52	-7.04	2.35	0.48	-9.39	-9.87	-0.050	-9.63
17.83	-7.51	-7.06	1.7	0.45	-8.76	-9.21	-0.050	-8.98
18.68	-7.51	-7.08	1.1	0.43	-8.18	-8.61	-0.051	-8.39
19.53	-7.52	-7.08	0.54	0.44	-7.62	-8.06	-0.056	-7.84
20.38	-7.5	-7.09	0.02	0.41	-7.11	-7.52	-0.056	-7.31
21.23	-7.43	-7.05	-0.46	0.38	-6.59	-6.97	-0.056	-6.78
22.08	-7.46	-7.1	-0.91	0.36	-6.19	-6.55	-0.057	-6.37
22.52	-7.43	-7.09	-1.29	0.34	-5.8	-6.14	-0.057	-5.97
22.93	-7.42	-7.09	-1.21	0.33	-5.88	-6.21	-0.055	-6.04
23.80	-7.4	-7.04	-1.22	0.36	-5.82	-6.18	-0.060	-6.00
24.65	-7.4	-7.05	-1.22	0.35	-5.83	-6.18	-0.058	-6.00
25.50	-7.49	-7.13	-1.22	0.36	-5.91	-6.27	-0.059	-6.09
26.35	-7.43	-7.09	-1.22	0.34	-5.87	-6.21	-0.056	-6.04
27.20	-7.4	-7.03	-1.23	0.37	-5.8	-6.17	-0.062	-5.98
28.07	-7.38	-7.04	-1.23	0.34	-5.81	-6.15	-0.057	-5.98
28.92	-7.41	-7.07	-1.23	0.34	-5.84	-6.18	-0.057	-6.01
29.77	-7.41	-7.05	-1.24	0.36	-5.81	-6.17	-0.060	-5.99
30.62	-7.4	-7.04	-1.24	0.36	-5.8	-6.16	-0.060	-5.98
31.47	-7.41	-7.08	-1.24	0.33	-5.84	-6.17	-0.055	-6.00
32.33	-7.4	-7.06	-1.24	0.34	-5.82	-6.16	-0.057	-5.99
33.17	-7.41	-7.05	-1.24	0.36	-5.81	-6.17	-0.060	-5.99
34.03	-7.39	-7.06	-1.24	0.33	-5.82	-6.15	-0.055	-5.98
34.88	-7.42	-7.09	-1.24	0.33	-5.85	-6.18	-0.055	-6.01
35.73	-7.42	-7.08	-1.24	0.34	-5.84	-6.18	-0.057	-6.01
36.58	-7.41	-7.08	-1.24	0.33	-5.84	-6.17	-0.055	-6.00
37.43	-7.4	-7.08	-1.24	0.32	-5.84	-6.16	-0.053	-6.00
38.28	-7.44	-7.1	-1.24	0.34	-5.86	-6.2	-0.056	-6.03
39.15	-7.42	-7.09	-1.24	0.33	-5.85	-6.18	-0.055	-6.01
40.00	-7.34	-7.04	-1.23	0.3	-5.81	-6.11	-0.050	-5.96
40.85	-7.42	-7.08	-1.22	0.34	-5.86	-6.2	-0.056	-6.03
41.70	-7.4	-7.04	-1.22	0.36	-5.82	-6.18	-0.060	-6.00
42.55	-7.38	-7.07	-1.21	0.31	-5.86	-6.17	-0.052	-6.01
43.40	-7.37	-7.05	-1.21	0.32	-5.84	-6.16	-0.053	-6.00
44.27	-7.4	-7.08	-1.21	0.32	-5.87	-6.19	-0.053	-6.03
45.12	-7.38	-7.1	-1.2	0.28	-5.9	-6.18	-0.046	-6.04

45.97	-7.38	-7.07	-1.2	0.31	-5.87	-6.18	-0.051	-6.02
46.82	-7.36	-7.05	-1.2	0.31	-5.85	-6.16	-0.052	-6.00
47.68	-7.39	-7.05	-1.2	0.34	-5.85	-6.19	-0.056	-6.02
48.52	-7.39	-7.07	-1.2	0.32	-5.87	-6.19	-0.053	-6.03
49.38	-7.4	-7.06	-1.2	0.34	-5.86	-6.2	-0.056	-6.03
50.23	-7.37	-7.05	-1.2	0.32	-5.85	-6.17	-0.053	-6.01
51.07	-7.37	-7.07	-1.2	0.3	-5.87	-6.17	-0.050	-6.02
51.93	-7.38	-7.05	-1.2	0.33	-5.85	-6.18	-0.055	-6.01
52.78	-7.4	-7.1	-1.19	0.3	-5.91	-6.21	-0.050	-6.06
53.65	-7.36	-7.06	-1.19	0.3	-5.87	-6.17	-0.050	-6.02
54.50	-7.35	-7.05	-1.19	0.3	-5.86	-6.16	-0.050	-6.01
55.33	-7.37	-7.07	-1.19	0.3	-5.88	-6.18	-0.050	-6.03
56.20	-7.4	-7.07	-1.19	0.33	-5.88	-6.21	-0.055	-6.04
57.05	-7.35	-7.06	-1.19	0.29	-5.87	-6.16	-0.048	-6.01
57.90	-7.33	-7.03	-1.19	0.3	-5.84	-6.14	-0.050	-5.99
58.75	-7.32	-7.01	-1.19	0.31	-5.82	-6.13	-0.052	-5.97
59.60	-7.32	-7.02	-1.19	0.3	-5.83	-6.13	-0.050	-5.98
60.45	-7.32	-7.02	-1.19	0.3	-5.83	-6.13	-0.050	-5.98
61.30	-7.35	-7.01	-1.19	0.34	-5.82	-6.16	-0.057	-5.99
62.15	-7.35	-7.04	-1.19	0.31	-5.85	-6.16	-0.052	-6.00
63.02	-7.31	-7.03	-1.19	0.28	-5.84	-6.12	-0.047	-5.98
63.87	-7.32	-7.05	-1.19	0.27	-5.86	-6.13	-0.045	-5.99
64.72	-7.35	-7.04	-1.19	0.31	-5.85	-6.16	-0.052	-6.00
65.57	-7.39	-7.08	-1.19	0.31	-5.89	-6.2	-0.051	-6.04
66.42	-7.35	-7.04	-1.19	0.31	-5.85	-6.16	-0.052	-6.00
67.27	-7.37	-7.05	-1.19	0.32	-5.86	-6.18	-0.053	-6.02
68.12	-7.34	-7.03	-1.19	0.31	-5.84	-6.15	-0.052	-5.99
68.97	-7.35	-7.05	-1.19	0.3	-5.86	-6.16	-0.050	-6.01
69.82	-7.34	-7.05	-1.19	0.29	-5.86	-6.15	-0.048	-6.00
70.67	-7.31	-7.02	-1.19	0.29	-5.83	-6.12	-0.049	-5.97
71.53	-7.34	-7.05	-1.19	0.29	-5.86	-6.15	-0.048	-6.00
72.38	-7.34	-7.05	-1.19	0.29	-5.86	-6.15	-0.048	-6.00
73.23	-7.3	-7.02	-1.19	0.28	-5.83	-6.11	-0.047	-5.97
74.10	-7.33	-7.04	-1.19	0.29	-5.85	-6.14	-0.048	-5.99
74.93	-7.3	-7.02	-1.19	0.28	-5.83	-6.11	-0.047	-5.97

75.78	-7.3	-7.02	-1.19	0.28	-5.83	-6.11	-0.047	-5.97
76.65	-7.32	-7.03	-1.19	0.29	-5.84	-6.13	-0.048	-5.98
77.50	-7.31	-7.02	-1.19	0.29	-5.83	-6.12	-0.049	-5.97
78.35	-7.28	-7.01	-1.19	0.27	-5.82	-6.09	-0.045	-5.95
79.20	-7.31	-7.02	-1.19	0.29	-5.83	-6.12	-0.049	-5.97
80.05	-7.33	-7.04	-1.19	0.29	-5.85	-6.14	-0.048	-5.99
80.90	-7.34	-7.04	-1.19	0.3	-5.85	-6.15	-0.050	-6.00
81.75	-7.31	-7.03	-1.19	0.28	-5.84	-6.12	-0.047	-5.98
82.60	-7.32	-7.04	-1.19	0.28	-5.85	-6.13	-0.047	-5.99
83.45	-7.34	-7.04	-1.19	0.3	-5.85	-6.15	-0.050	-6.00
84.30	-7.29	-7.03	-1.19	0.26	-5.84	-6.1	-0.044	-5.97
85.15	-7.37	-7.11	-1.19	0.26	-5.92	-6.18	-0.043	-6.05
85.02	-7.26	-7	-1.19	0.26	-5.81	-6.07	-0.044	-5.94
86.87	-7.31	-7.04	-1.19	0.27	-5.85	-6.12	-0.045	-5.98
87.72	-7.32	-7.03	-1.19	0.29	-5.84	-6.13	-0.048	-5.98
88.58	-7.28	-7.03	-1.19	0.25	-5.84	-6.09	-0.042	-5.96
89.42	-7.3	-7.02	-1.19	0.28	-5.83	-6.11	-0.047	-5.97
90.27	-7.34	-7.05	-1.19	0.29	-5.86	-6.15	-0.048	-6.00
91.13	-7.34	-7.05	-1.19	0.29	-5.86	-6.15	-0.048	-6.00
91.98	-7.32	-7.06	-1.19	0.26	-5.87	-6.13	-0.043	-6.00
92.83	-7.32	-7.05	-1.19	0.27	-5.86	-6.13	-0.045	-5.99
93.68	-7.33	-7.05	-1.19	0.28	-5.86	-6.14	-0.047	-6.00
94.53	-7.28	-7.03	-1.19	0.25	-5.84	-6.09	-0.042	-5.96
95.38	-7.32	-7.05	-1.19	0.27	-5.86	-6.13	-0.045	-5.99
96.23	-7.3	-7.04	-1.19	0.26	-5.85	-6.11	-0.043	-5.98
97.08	-7.31	-7.05	-1.19	0.26	-5.86	-6.12	-0.043	-5.99
97.93	-7.32	-7.03	-1.19	0.29	-5.84	-6.13	-0.048	-5.98
average								-6.00

10.2 Yield vs dt

This is shown in the respective average yields (% of the feed converted to ice and salt) in Table 10.2.

Table 10.2: Effect of ΔT_{LMTD} on overall yield

ΔT_{LMTD} (°C)	Yield (%)
2	15±3
4	30±4
6	38±2
8	46±1
10	53±1

10.3 Calculation of ice purity

The purity of ice was calculated from absorbances measured on three samples of ice reacted with $BaCl_2$. The ice was reacted with $BaCl_2$ to form a white suspension of $BaSO_4$ that would obstruct light and thereby affect the absorbance. The average absorbance was multiplied by the dilution factor and equation *10.2* relating absorbance to concentration of SO_4^{2-} ions (obtained experimentally).

$$[SO_4^{2-}] = \frac{Absorbance - 0.0853}{0.0136} \times dilution\ factor \qquad 10.2$$

The concentration of the salt was calculated using equation *10.3*:

$$[Na_2SO_4] = \frac{142.04g\ g/mole}{96.06\ g/mole} \times [SO_4^{2-}] \qquad 10.3$$

Equation *10.4* was used to calculate the mass of salt present in the ice/brine.

$$m_{Na_2SO^4} = [Na_2SO^4] \times volume\ of\ ice\ product \qquad 10.4$$

Equation *10.5* was used to calculate the purity (%H_2O) of the ice/brine:

$$purity = 100 - \left(\left(\frac{m_{Na_2SO^4}}{m_{ice\ product}}\right) \times 100\right) \qquad 10.5$$

10.4 Calculation of Q_{cool}

The heat transfer rate was calculated using the coolant temperature measurements as well as the temperature functions for Kryo-51 as provided by the supplier, Lauda. These are listed in

.

Table 10.3: Coolant data

Description	Symbol	Value
Density of coolant at 23 °C	$\rho_{coolant,23}$	908.00
Coolant flow rate at 23 °C (kg/s)	$\dot{m}_{coolant,23}$	0.210
Density function (kg/m³)	ρ	$\rho = -0.882T + 943.38$
Specific heat capacity function (kJ/kg°C)	C_p	$C_p = 0.0015T + 1.59$

For each coolant inlet and outlet temperature reading, an average coolant temperature was calculated and was used to calculate ρ and C_p. The coolant flow rate and the temperature difference were calculated using equations *10.6* and *10.8*.

$$\dot{m}_{coolant,T} = \left(\frac{\rho_{coolant,T}}{\rho_{coolant,23}}\right)\dot{m}_{coolant,23} \qquad 10.6$$

$$dT_{coolant} = T_{coolant,out} - T_{coolant,in} \qquad 10.7$$

Thereafter the following equation was used to calculate Q:

$$Q_{cool} = \dot{m}_{coolant,T}C_p dT \qquad 10.8$$

Table 10.4 shows the Q values for a $\Delta T_{LMTD} = 6$ experiment as an example. An average Q_{cool} was calculated from the point of seeding. There were very minimal differences in the Q_{cool} over the duration of the experiment, so an average could be used to show the overall value for one experiment. This was done for all the ΔT_{LMTD} and seed loading experiments.

Table 10.4: Calculated values of Q for ΔT_{LMTD} =6 experiment

Time	**$T_{C,in}$**	**$T_{C,in}$**	**Avg Tc**	**ρ**	**m**	**cp**	**dT**	**q(kW)**
Min	℃			kg/m^3	kg/s	kJ/kg ℃	℃	
0.00	19.77	19.28	19.525	926.15	0.214	1.619	-0.49	-0.170
0.70	15.02	15	15.01	930.14	0.215	1.613	-0.02	-0.007
1.73	10.64	10.65	10.645	933.99	0.216	1.606	0.01	0.003
2.52	6.87	6.92	6.895	937.30	0.217	1.600	0.05	0.017
3.22	3.59	3.8	3.695	940.12	0.218	1.596	0.21	0.073
4.22	0.46	0.85	0.655	942.80	0.218	1.591	0.39	0.135
5.07	-2.18	-1.7	-1.94	945.09	0.219	1.587	0.48	0.167
5.92	-4.66	-4.22	-4.44	947.30	0.219	1.583	0.44	0.153
6.77	-6.89	-6.43	-6.66	949.26	0.220	1.580	0.46	0.160
7.62	-7.94	-7.06	-7.5	950.00	0.220	1.579	0.88	0.305
8.47	-6.35	-5.66	-6.005	948.68	0.220	1.581	0.69	0.240
9.33	-6.42	-5.78	-6.1	948.76	0.220	1.581	0.64	0.222
10.20	-6.92	-6.22	-6.57	949.18	0.220	1.580	0.7	0.243
11.05	-7.25	-6.54	-6.895	949.46	0.220	1.580	0.71	0.246
11.90	-7.46	-6.81	-7.135	949.68	0.220	1.579	0.65	0.226
12.73	-7.46	-6.82	-7.14	949.68	0.220	1.579	0.64	0.222
13.58	-7.41	-6.94	-7.175	949.71	0.220	1.579	0.47	0.163
14.43	-7.61	-7.06	-7.335	949.85	0.220	1.579	0.55	0.191
15.28	-7.56	-7.04	-7.3	949.82	0.220	1.579	0.52	0.180
16.13	-7.55	-7.05	-7.3	949.82	0.220	1.579	0.5	0.174
16.98	-7.52	-7.04	-7.28	949.80	0.220	1.579	0.48	0.167
17.83	-7.51	-7.06	-7.285	949.81	0.220	1.579	0.45	0.156
18.68	-7.51	-7.08	-7.295	949.82	0.220	1.579	0.43	0.149
19.53	-7.52	-7.08	-7.3	949.82	0.220	1.579	0.44	0.153
20.38	-7.5	-7.09	-7.295	949.82	0.220	1.579	0.41	0.142
21.23	-7.43	-7.05	-7.24	949.77	0.220	1.579	0.38	0.132
22.08	-7.46	-7.1	-7.28	949.80	0.220	1.579	0.36	0.125
22.52	-7.42	-7.1	-7.26	949.79	0.220	1.579	0.32	0.111

22.93	-7.43	-7.09	-7.26	949.79	0.220	1.579	0.34	0.118
23.80	-7.42	-7.09	-7.255	949.78	0.220	1.579	0.33	0.115
24.65	-7.4	-7.04	-7.22	949.75	0.220	1.579	0.36	0.125
25.50	-7.4	-7.05	-7.225	949.76	0.220	1.579	0.35	0.121
26.35	-7.49	-7.13	-7.31	949.83	0.220	1.579	0.36	0.125
27.20	-7.43	-7.09	-7.26	949.79	0.220	1.579	0.34	0.118
28.07	-7.4	-7.03	-7.215	949.75	0.220	1.579	0.37	0.128
28.92	-7.38	-7.04	-7.21	949.74	0.220	1.579	0.34	0.118
29.77	-7.41	-7.07	-7.24	949.77	0.220	1.579	0.34	0.118
30.62	-7.41	-7.05	-7.23	949.76	0.220	1.579	0.36	0.125
31.47	-7.4	-7.04	-7.22	949.75	0.220	1.579	0.36	0.125
32.33	-7.41	-7.08	-7.245	949.77	0.220	1.579	0.33	0.115
33.17	-7.4	-7.06	-7.23	949.76	0.220	1.579	0.34	0.118
34.03	-7.41	-7.05	-7.23	949.76	0.220	1.579	0.36	0.125
34.88	-7.39	-7.06	-7.225	949.76	0.220	1.579	0.33	0.115
35.73	-7.42	-7.09	-7.255	949.78	0.220	1.579	0.33	0.115
36.58	-7.42	-7.08	-7.25	949.78	0.220	1.579	0.34	0.118
37.43	-7.41	-7.08	-7.245	949.77	0.220	1.579	0.33	0.115
38.28	-7.4	-7.08	-7.24	949.77	0.220	1.579	0.32	0.111
39.15	-7.44	-7.1	-7.27	949.80	0.220	1.579	0.34	0.118
40.00	-7.42	-7.09	-7.255	949.78	0.220	1.579	0.33	0.115
40.85	-7.34	-7.04	-7.19	949.72	0.220	1.579	0.3	0.104
41.70	-7.42	-7.08	-7.25	949.78	0.220	1.579	0.34	0.118
42.55	-7.4	-7.04	-7.22	949.75	0.220	1.579	0.36	0.125
43.40	-7.38	-7.07	-7.225	949.76	0.220	1.579	0.31	0.108
44.27	-7.37	-7.05	-7.21	949.74	0.220	1.579	0.32	0.111
45.12	-7.4	-7.08	-7.24	949.77	0.220	1.579	0.32	0.111
45.97	-7.38	-7.1	-7.24	949.77	0.220	1.579	0.28	0.097
46.82	-7.38	-7.07	-7.225	949.76	0.220	1.579	0.31	0.108
47.68	-7.36	-7.05	-7.205	949.74	0.220	1.579	0.31	0.108
48.52	-7.39	-7.05	-7.22	949.75	0.220	1.579	0.34	0.118
49.38	-7.39	-7.07	-7.23	949.76	0.220	1.579	0.32	0.111

50.23	-7.4	-7.06	-7.23	949.76	0.220	1.579	0.34	0.118
51.07	-7.37	-7.05	-7.21	949.74	0.220	1.579	0.32	0.111
51.93	-7.37	-7.07	-7.22	949.75	0.220	1.579	0.3	0.104
52.78	-7.38	-7.05	-7.215	949.75	0.220	1.579	0.33	0.115
53.65	-7.4	-7.1	-7.25	949.78	0.220	1.579	0.3	0.104
54.50	-7.36	-7.06	-7.21	949.74	0.220	1.579	0.3	0.104
55.33	-7.35	-7.05	-7.2	949.73	0.220	1.579	0.3	0.104
56.20	-7.37	-7.07	-7.22	949.75	0.220	1.579	0.3	0.104
57.05	-7.4	-7.07	-7.235	949.76	0.220	1.579	0.33	0.115
57.90	-7.35	-7.06	-7.205	949.74	0.220	1.579	0.29	0.101
58.75	-7.33	-7.03	-7.18	949.72	0.220	1.579	0.3	0.104
59.60	-7.32	-7.01	-7.165	949.70	0.220	1.579	0.31	0.108
60.45	-7.32	-7.02	-7.17	949.71	0.220	1.579	0.3	0.104
61.30	-7.32	-7.02	-7.17	949.71	0.220	1.579	0.3	0.104
62.15	-7.35	-7.01	-7.18	949.72	0.220	1.579	0.34	0.118
63.02	-7.35	-7.04	-7.195	949.73	0.220	1.579	0.31	0.108
63.87	-7.31	-7.03	-7.17	949.71	0.220	1.579	0.28	0.097
64.72	-7.32	-7.05	-7.185	949.72	0.220	1.579	0.27	0.094
65.57	-7.35	-7.04	-7.195	949.73	0.220	1.579	0.31	0.108
66.42	-7.39	-7.08	-7.235	949.76	0.220	1.579	0.31	0.108
67.27	-7.35	-7.04	-7.195	949.73	0.220	1.579	0.31	0.108
68.12	-7.37	-7.05	-7.21	949.74	0.220	1.579	0.32	0.111
68.97	-7.34	-7.03	-7.185	949.72	0.220	1.579	0.31	0.108
69.82	-7.35	-7.05	-7.2	949.73	0.220	1.579	0.3	0.104
70.67	-7.34	-7.05	-7.195	949.73	0.220	1.579	0.29	0.101
71.53	-7.31	-7.02	-7.165	949.70	0.220	1.579	0.29	0.101
72.38	-7.34	-7.05	-7.195	949.73	0.220	1.579	0.29	0.101
73.23	-7.34	-7.05	-7.195	949.73	0.220	1.579	0.29	0.101
74.10	-7.3	-7.02	-7.16	949.70	0.220	1.579	0.28	0.097
74.93	-7.33	-7.04	-7.185	949.72	0.220	1.579	0.29	0.101
75.78	-7.3	-7.02	-7.16	949.70	0.220	1.579	0.28	0.097
76.65	-7.3	-7.02	-7.16	949.70	0.220	1.579	0.28	0.097

77.50	-7.32	-7.03	-7.175	949.71	0.220	1.579	0.29	0.101
78.35	-7.31	-7.02	-7.165	949.70	0.220	1.579	0.29	0.101
79.20	-7.28	-7.01	-7.145	949.68	0.220	1.579	0.27	0.094
80.05	-7.31	-7.02	-7.165	949.70	0.220	1.579	0.29	0.101
80.90	-7.33	-7.04	-7.185	949.72	0.220	1.579	0.29	0.101
81.75	-7.34	-7.04	-7.19	949.72	0.220	1.579	0.3	0.104
82.60	-7.31	-7.03	-7.17	949.71	0.220	1.579	0.28	0.097
83.45	-7.32	-7.04	-7.18	949.72	0.220	1.579	0.28	0.097
84.30	-7.34	-7.04	-7.19	949.72	0.220	1.579	0.3	0.104
85.15	-7.29	-7.03	-7.16	949.70	0.220	1.579	0.26	0.090
85.02	-7.37	-7.11	-7.24	949.77	0.220	1.579	0.26	0.090
86.87	-7.26	-7	-7.13	949.67	0.220	1.579	0.26	0.090
87.72	-7.31	-7.04	-7.175	949.71	0.220	1.579	0.27	0.094
88.58	-7.32	-7.03	-7.175	949.71	0.220	1.579	0.29	0.101
89.42	-7.28	-7.03	-7.155	949.69	0.220	1.579	0.25	0.087
90.27	-7.3	-7.02	-7.16	949.70	0.220	1.579	0.28	0.097
91.13	-7.34	-7.05	-7.195	949.73	0.220	1.579	0.29	0.101
91.98	-7.34	-7.05	-7.195	949.73	0.220	1.579	0.29	0.101
92.83	-7.32	-7.06	-7.19	949.72	0.220	1.579	0.26	0.090
93.68	-7.32	-7.05	-7.185	949.72	0.220	1.579	0.27	0.094
94.53	-7.33	-7.05	-7.19	949.72	0.220	1.579	0.28	0.097
95.38	-7.28	-7.03	-7.155	949.69	0.220	1.579	0.25	0.087
96.23	-7.32	-7.05	-7.185	949.72	0.220	1.579	0.27	0.094
97.08	-7.3	-7.04	-7.17	949.71	0.220	1.579	0.26	0.090
97.93	-7.31	-7.05	-7.18	949.72	0.220	1.579	0.26	0.090
	-7.32	-7.03	-7.175	949.71	0.220	1.579	0.29	0.101
Average								0.106

10.5 Calculation of U

Equation *10.9* was used to calculate U by using ΔT_{LMTD}s calculated in section 10.1, the heat transfer area as calculated by equation *10.10* of the crystallizer and making U the subject of the formula. Thereafter, an average U was calculated. This was done from the point of seeding.

$$Q_{cool} = Q_{tot} = UA\Delta T_{LMTD} \tag{10.9}$$

$$A = 2\pi rh + \pi r^2 \tag{10.10}$$

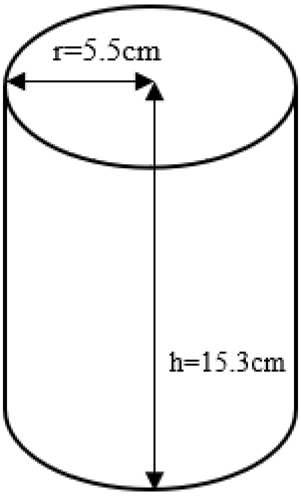

Figure 10.1: Schematic of the inner part of the crystallizer; the top was open so only the area of the bottom surface was calculated

Table 10.5 shows the calculated U values for ΔT_{LMTD} = 6 experiment as an example. There were very minimal differences in the U values over the duration of the experiment, so an average could be used to show the overall value for one experiment This was done for all the ΔT_{LMTD} and seed loading experiments.

Table 10.5: U calculation for ΔT_{LMTD} = 6°C

T	**q**	**Q/A**	**ΔT_{LMTD}**	**u**
min	kW	W/cm^2	°C	W/cm^2 °C
0	-0.170	-0.273	-1.056	0.259
0.70	-0.007	-0.011	-5.590	0.002
1.73	0.003	0.006	-9.825	0.001
2.52	0.017	0.028	-13.025	0.002
3.22	0.073	0.117	-15.465	0.008
4.22	0.135	0.218	-17.614	0.012
5.07	0.167	0.268	-19.229	0.014
5.92	0.153	0.245	-20.679	0.012
6.77	0.160	0.257	-21.799	0.012

7.62	0.305	0.491	-21.517	0.023
8.47	0.240	0.385	-18.213	0.021
9.33	0.222	0.357	-17.018	0.021
10.20	0.243	0.390	-16.247	0.024
11.05	0.246	0.396	-15.432	0.026
11.90	0.226	0.362	-14.583	0.025
12.73	0.222	0.357	-13.577	0.026
13.58	0.163	0.262	-12.674	0.021
14.43	0.191	0.307	-11.953	0.026
15.28	0.180	0.290	-11.098	0.026
16.13	0.174	0.279	-10.348	0.027
16.98	0.167	0.268	-9.628	0.028
17.83	0.156	0.251	-8.983	0.028
18.68	0.149	0.240	-8.393	0.029
19.53	0.153	0.245	-7.838	0.031
20.38	0.142	0.229	-7.313	0.031
21.23	0.132	0.212	-6.778	0.031
22.08	0.125	0.201	-6.368	0.032
22.52	0.111	0.178	-5.968	0.030
22.93	0.118	0.190	-6.043	0.031
23.80	0.115	0.184	-5.998	0.031
24.65	0.125	0.201	-6.003	0.033
25.50	0.121	0.195	-6.088	0.032
26.35	0.125	0.201	-6.038	0.033
27.20	0.118	0.190	-5.983	0.032
28.07	0.128	0.206	-5.978	0.035
28.92	0.118	0.190	-6.008	0.032
29.77	0.118	0.190	-5.988	0.032
30.62	0.125	0.201	-5.978	0.034
31.47	0.125	0.201	-6.003	0.033
32.33	0.115	0.184	-5.988	0.031
33.17	0.118	0.190	-5.988	0.032

34.03	0.125	0.201	-5.983	0.034
34.88	0.115	0.184	-6.013	0.031
35.73	0.115	0.184	-6.008	0.031
36.58	0.118	0.190	-6.003	0.032
37.43	0.115	0.184	-5.999	0.031
38.28	0.111	0.178	-6.028	0.030
39.15	0.118	0.190	-6.013	0.032
40.00	0.115	0.184	-5.959	0.031
40.85	0.104	0.167	-6.028	0.028
41.70	0.118	0.190	-5.998	0.032
42.55	0.125	0.201	-6.014	0.033
43.40	0.108	0.173	-5.999	0.029
44.27	0.111	0.178	-6.029	0.030
45.12	0.111	0.178	-6.039	0.030
45.97	0.097	0.156	-6.024	0.026
46.82	0.108	0.173	-6.004	0.029
47.68	0.108	0.173	-6.018	0.029
48.52	0.118	0.190	-6.029	0.031
49.38	0.111	0.178	-6.028	0.030
50.23	0.118	0.190	-6.009	0.032
51.07	0.111	0.178	-6.019	0.030
51.93	0.104	0.167	-6.013	0.028
52.78	0.115	0.184	-6.059	0.030
53.65	0.104	0.167	-6.019	0.028
54.50	0.104	0.167	-6.009	0.028
55.33	0.104	0.167	-6.029	0.028
56.20	0.104	0.167	-6.043	0.028
57.05	0.115	0.184	-6.014	0.031
57.90	0.101	0.162	-5.989	0.027
58.75	0.104	0.167	-5.974	0.028
59.60	0.108	0.173	-5.979	0.029
60.45	0.104	0.167	-5.979	0.028

61.30	0.104	0.167	-5.988	0.028
62.15	0.118	0.190	-6.004	0.032
63.02	0.108	0.173	-5.979	0.029
63.87	0.097	0.156	-5.994	0.026
64.72	0.094	0.151	-6.004	0.025
65.57	0.108	0.173	-6.044	0.029
66.42	0.108	0.173	-6.004	0.029
67.27	0.108	0.173	-6.019	0.029
68.12	0.111	0.178	-5.994	0.030
68.97	0.108	0.173	-6.009	0.029
69.82	0.104	0.167	-6.004	0.028
70.67	0.101	0.162	-5.974	0.027
71.53	0.101	0.162	-6.004	0.027
72.38	0.101	0.162	-6.004	0.027
73.23	0.101	0.162	-5.969	0.027
74.10	0.097	0.156	-5.994	0.026
74.93	0.101	0.162	-5.969	0.027
75.78	0.097	0.156	-5.969	0.026
76.65	0.097	0.156	-5.984	0.026
77.50	0.101	0.162	-5.974	0.027
78.35	0.101	0.162	-5.954	0.027
79.20	0.094	0.151	-5.974	0.025
80.05	0.101	0.162	-5.994	0.027
80.90	0.101	0.162	-5.999	0.027
81.75	0.104	0.167	-5.979	0.028
82.60	0.097	0.156	-5.989	0.026
83.45	0.097	0.156	-5.999	0.026
84.30	0.104	0.167	-5.969	0.028
85.15	0.090	0.145	-6.049	0.024
85.02	0.090	0.145	-5.939	0.024
86.87	0.090	0.145	-5.984	0.024
87.72	0.094	0.151	-5.984	0.025

88.58	0.101	0.162	-5.964	0.027
89.42	0.087	0.139	-5.969	0.023
90.27	0.097	0.156	-6.004	0.026
91.13	0.101	0.162	-6.004	0.027
91.98	0.101	0.162	-5.999	0.027
92.83	0.090	0.145	-5.994	0.024
93.68	0.094	0.151	-5.999	0.025
94.53	0.097	0.156	-5.964	0.026
95.38	0.087	0.139	-5.994	0.023
96.23	0.094	0.151	-5.979	0.025
97.08	0.090	0.145	-5.989	0.024
97.93	0.090	0.145	-5.984	0.024
98.78	0.101	0.162	-6.000	0.027
average				0.028

10.6 Calculation of seed loading

The following equation was developed for the calculation of seed loading. The main constraint was that the total volume of the brine and the seeds had to be equal to the volume of the crystallizer (1450ml).

$$SL = \frac{m_{seeds}}{m_{brine}} \tag{10.11}$$

$$m_{seeds} = \rho_{seeds} V_{seeds} \tag{10.12}$$

$$m_{brine} = \rho_{brine} V_{brine} \tag{10.13}$$

$$V_{seeds} + V_{brine} = 1450 \tag{10.14}$$

By making V_{brine} the subject of the formula in equation *10.14* and substituting equations *10.12* and *10.13* into equation *10.11*, equation *10.15* was formulated.

$$SL = \frac{\rho_{seeds} V_{seeds}}{\rho_{brine}(1450 - V_{Seeds})} \tag{10.15}$$

This was rearranged to solve for V_{Seeds}as shown below:

$$SL = \frac{\rho_{seeds} V_{seeds}}{(1450\rho_{brine} - \rho_{brine} V_{Seeds})}$$

$$SL(1450\rho_{brine} - \rho_{brine} V_{Seeds}) = \rho_{seeds} V_{seeds}$$

$$1450 SL \rho_{brine} - SL \rho_{brine} V_{Seeds} = \rho_{seeds} V_{seeds}$$

$$1450SL\rho_{brine} = \rho_{seeds}V_{seeds} + SL\rho_{brine}V_{Seeds}$$

$$1450SL\rho_{brine} = (\rho_{seeds} + SL\rho_{brine})V_{Seeds}$$

$$\frac{1450SL\rho_{brine}}{(\rho_{seeds} + SL\rho_{brine})} = V_{seeds} \qquad 10.16$$

the volume of the brine as well as the mass of the seeds and the brine.

Table 10.6: seed masses for each seed loading

SL	ρ_{seeds}	ρ_{brine}	V_{seeds}	V_{brine}	m_{seeds}	m_{brine}
0.10%	0.99	1.03	1.45	1448.55	1.44	1492.01
3.00%			43.94	1406.07	43.50	1448.25
6.00%			85.26	1364.74	84.41	1405.68
9.00%			124.12	1325.88	122.88	1365.66
12.00%			160.95	1289.05	159.34	1327.72

10.7 Seed sizes

Figure 10.2 and Figure 10.3 show the CSD and images of the seeds.

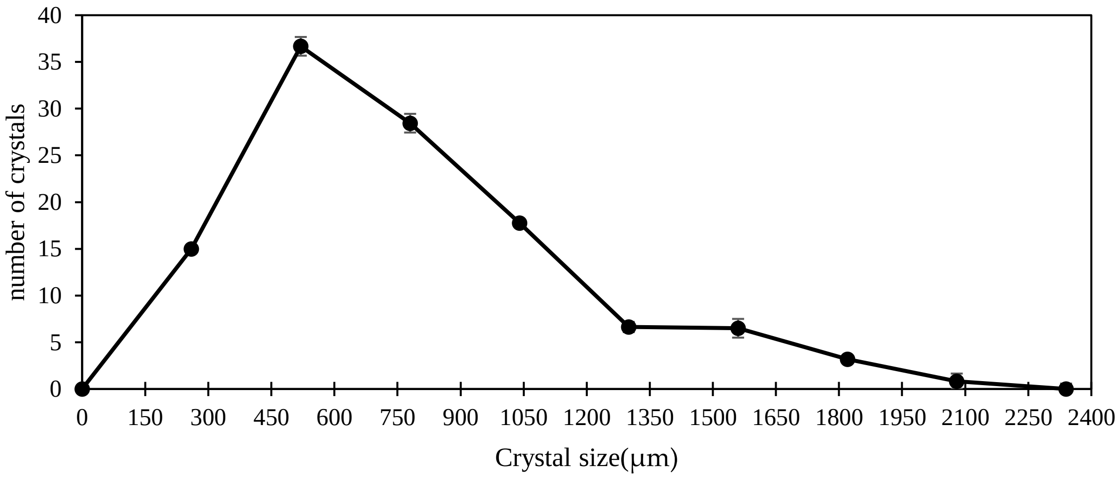

Figure 10.2: Average CSD of the seeds from the ice-shaving machine

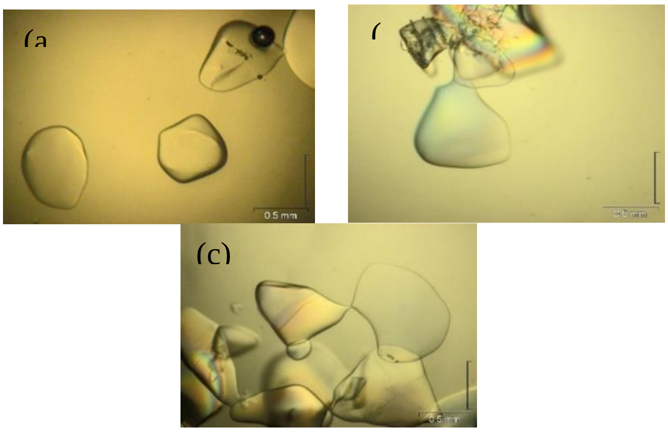

Figure 10.3: Images of seeds from the 3 trials (a, b, c) of seed preparation using the ice-shaving machine.

10.8 Normalisation of yields at different seed loadings

The ice yield at each seed loading was obtained using equation *10.17*

$$ice\ yield = ice\ harvested - ice\ seeds \qquad 10.17$$

Thereafter the normalised yield was calculated using equation *10.18*. The same equation was used for the yield of salt.

$$yield^{*}(g/gH_2O) = \frac{ice\ yield}{Theoretical\ ice\ yield} \qquad 10.18$$

10.9 Calculation of magma density

Equation *10.19* was used to calculate the magma density at each seed loading and ΔT_{LMTD}.

$$M_T = \frac{(m_{ice} + m_{salt} + m_{seeds})}{m_{ice} + m_{salt} + m_{seeds} + m_{brine}} \times 100\% \qquad 10.19$$

10.10 Calculation of α_{scale}

It was assumed the scale layer was a uniform anulus that only covered the crystallizer up to the length of the impeller position as the impeller was never stopped by the scale, and the scale was very thin around the impeller. This is illustrated in Figure 10.4.

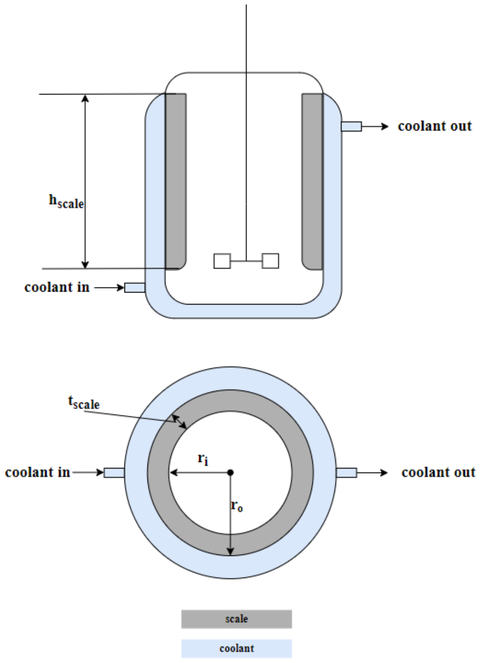

Figure 10.4: illustration of scaling on crystallizer wall

The inner radius, r_i was required for the calculation of the resistance due to the scale layer. The equation for r_i was formulated from the volume of the scale layer. This is shown below.

$$\rho_{scale} = \frac{m_{scale}}{V_{scale}}$$

$$V_{scale} = \frac{m_{scale}}{\rho_{scale}}$$

$$V_{scale} = \pi r_o^2 h_{scale} - \pi r_i^2 h_{scale}$$

$$\therefore \pi r_o^2 h_{scale} - \pi r_i^2 h_{scale} = \frac{m_{scale}}{\rho_{scale}}$$

$$\pi r_o^2 h_{scale} - \frac{m_{scale}}{\rho_{scale}} = \pi r_i^2 h_{scale}$$

$$r_o^2 - \frac{m_{scale}}{\rho_{scale} \pi h_{scale}} = r_i^2$$

$$r_i = \sqrt{r_o^2 - \frac{m_{scale}}{\rho_{scale} \pi h_{scale}}} \qquad 10.20$$

The thickness of the scale was calculated using equation *10.21*. This was done to confirm the thickening of the scale layer as the mass of the scale layer increased.

$$t_{scale} = r_o - r_i \qquad 10.21$$

The conductive resistance due to the scale layer was calculated using equation *10.22* (Welty et al., 2000).

$$R_{scale} = \frac{\ln\left(\frac{r_o}{r_i}\right)}{2\pi k h_{scale}} \qquad 10.22$$

The resistance was multiplied by the scale heat transfer area (surface area of a cylinder with radius r_i and height h_{scale}). From here, α_{scale} was calculated using equation *2.9* which is reiterated below.

$$\alpha = \frac{1}{R_{scale} A_{scale}} \qquad 2.4$$

10.11 Calculation of Re

Equation *10.23* was used to calculate the Re for the suspension after seeding and at the final magma density, where ρ (kg/ m^3) was the density of the suspension, v (m/s) was the velocity of the suspension, D(m) was the diameter of the impeller and μ(Pa.s) was the suspension viscosity.

$$Re = \frac{\rho_{suspension} N D_{impeller}^2}{\mu_{suspension}} \tag{10.23}$$

where N (s^{-1}) was the rotational speed of the impeller, $\rho_{suspension}$ (kg/m^3) was the density of the suspension and $\mu_{suspension}$ (Pa. s) was the dynamic viscosity of the suspension.

Equation *10.24* was used to calculate the viscosity of the suspension (Mardles, 1940).

$$\mu_{suspension} = \mu_{brine}(1 + 2.5\phi) \tag{10.24}$$

ϕ was the solids volume fraction, μ_{brine} was the brine viscosity which was obtained from OLI Stream Analyser ™ V10.0.

The density of the suspension was calculated based on the mass fractions, x, of the solids and the brine. This is shown in equation *10.25*.

$$\rho_{suspension} = x_{solids}\rho_{solids} + x_{brine}\rho_{brine} \tag{10.25}$$

10.12 Calculation of $\alpha_{process}$

The heat transfer coefficient was calculated using the Dittus-Boelter correlation for the Nusselt number. This is shown in equation *10.26* (Dittus & Boelter, 1930).

$$Nu = 0.023Re^{0.8}\,\mathrm{Pr}^{0.3} \tag{10.26}$$

where Re was the Reynolds number (calculated in section 0) and Pr was the Prandtl number given by equation *10.27*

$$Pr = \frac{\mu C_p}{k} \tag{10.27}$$

where μ (Pa.s) was the effective viscosity of the suspension, Cp (J/kg K) was the heat capacity of the suspension and k (W/mK) was the thermal conductivity of the suspension.

After obtaining the Nu, the heat transfer coefficient was calculated using equation *10.28*

$$Nu = \frac{\alpha_{process,\infty}\, D}{k} \tag{10.28}$$

where $\alpha_{process,\infty}$ was the heat transfer coefficient, D was the diameter the suspension was moving through, and k was the thermal conductivity of the suspension. For the final heat transfer coefficients, the diameter that the suspension was moving through was determined by the thickness of the scale layer calculated in section 10.10.

The diameter to be used in equation *10.28* was calculated using equation *10.29*:

$$D = 2 \times r_i \qquad 10.29$$

The heat transfer coefficient, $\alpha_{process,\infty}$, calculated using equation *10.28* is for vessels with an $\frac{L}{D}$ ratio that is larger than 60. To convert it to one that is smaller (the one for this work was 1.4), equation *10.30* was used (Deissler, 1955).

$$\frac{\alpha_{process}}{\alpha_{process,\infty}} = 1 + \left(\frac{D}{L}\right)^{0.7} \qquad 10.30$$

where $\alpha_{process}$ is the process heat transfer coefficient of our system, $\alpha_{process,\infty}$ is the heat transfer coefficient calculated using equation *10.28*, L is the length of the crystallizer and D is the diameter the suspension is moving through, once again the thickness of the scale layer was taken into account for the final heat transfer coefficients.